Expanding the toolbox for thermal control of *E. coli*:
Cold-activated transcription with applications in temperature self-regulation

Thesis by
Lealia Li Xiong

In Partial Fulfillment of the Requirements for the
Degree of
Doctor of Philosophy

CALIFORNIA INSTITUTE OF TECHNOLOGY
Pasadena, California

2023
Defended December 13, 2022

Lealia Li Xiong
ORCID: 0000-0001-7636-5936

ACKNOWLEDGEMENTS

As a student co-advised in the Kornfield and Shapiro labs, I have spent a lot of time walking samples back and forth between Schlinger, where the Kornfield lab is located, and Spalding, where the Shapiro lab is located. Although Caltech's campus is tiny, those couple of minutes per experiment add up, and I have used some of them to try to think of the best way to thank everyone who helped me to complete this thesis.

This work would not have been possible without my advisors, Mikhail Shapiro and Julie Kornfield. Mikhail gave me the gift of a few minutes of his time when I was at the end of my second year at Caltech and looking for a new project. He is the one that suggested that he, Julie, and I work together to develop thermal self-regulation for living materials.

I would like to acknowledge my colleagues in the Shapiro lab, particularly Michael Garrett for being the best summer student. Your contributions have echoed in the years since, and I am glad that we can now see the fruits of our work together. Thank you also to Di Wu, Dan Piraner, and George Lu for helping me get started in the lab, and to Cameron Smith for coming in in the last few months of my PhD and providing wonderful sanity checks, mathematical and otherwise. Marjorie Buss and Erik Schrunk — we never got to celebrate passing our candidacy exams in the same month. Maybe there's still time? Finally, thank you to our wonderful staff and technicians throughout my time working with the lab: Dina Malounda, Gabrielle Ho, Teresa Tran, Audrey Lee-Gosselin, Margaret Swift, Ruby Zhang, and Rosie Zedan.

In addition, I would like to thank my colleagues in the Kornfield lab. Julie, thank you for agreeing to co-advise me on this little project that occupies the exact overlap of the Kornfield lab and Shapiro lab, and thank you especially for supporting me through the COVID-19 pandemic. Thank you to Priya Chittur and Tiziana Di Luccio for welcoming me to the lab and for your solidarity in figuring out engineered living materials. Rob Learsch, Red Lhota, and Andy Ylitalo — we did it! Thanks additionally to Rachel Ford, Andy, and Jin Mo Koo for keeping us safe in the lab, and to Abigail McCann, Christine Jary, and Therese Bagsit for helping us to keep Julie on track. Thank you to the rest of the Kornfield lab — Paresh Samantaray, Dennis Ko, Ben Laccetti, and more — for our interesting conversations throughout

the years. Finally, thanks to GG, Tyler, and Spencer for not only your expertise in heat transfer, but your friendship and support along the way.

Furthermore, thank you to Sasha Fishman and Alix Kang for being amazing new scientists and teaching me different perspectives from your art and design backgrounds. Mentoring you has been a pleasure.

Next, thank you to the Department of Medical Engineering at Caltech, in particular Christine Garske and my committee members, Vivana Gradinaru and Wei Gao. In addition, I would like to thank my fellow MedE graduate student council members, especially Colin Cook and David Garrett.

Outside of Caltech, I would like to acknowledge the staff and volunteers I worked with at John Muir High School, Franchesca Ocasio, Ana Gonzalez, Efren Monterroso Carias, Giovanni Ayala, and Charles Winston, in addition to the students I got to know.

Before I ever got to Caltech, I had the deep privilege to learn from and be supported by some of the smartest and kindest scientists in the world. Thank you to Deepak Mishra for getting my research career started, and for all the mentorship and friendship since 2012. You weren't half bad as a wedding officiant, either. Thanks also to Aranda Duan and Tami Lieberman for teaching me and allowing me to contribute to your research projects. Finally, thank you to Alan Ransil and Wenhao Sun for getting me into scientific entrepreneurship. I still admire your audacity and tenacity.

Thank you to my parents, Shu Li and Jinming Xiong for always making sure I got the best education possible. Thank you for driving me to extra math classes on Saturdays, for sending me to Exeter, and for sending me to China for my first research experience. And thank you to my second family from childhood: Paige, Hannah, Sue, and Mark Cascio. Your support means the world to me.

I have saved the best for last. Rob Learsch, I couldn't have done this without you. Well, I probably could have, but I wouldn't have wanted to. When I applied for iGEM ten years ago, I didn't know how much my life was about to change. You are the best teammate, partner, husband, and colleague. Thank you.

ABSTRACT

Temperature can be used to control engineered *E. coli* — for example, the living component of an engineered living material (ELM) — through the use of thermolabile transcription factors. Sharp induction of gene expression with heat has been established using these bacteria- and phage-derived proteins. Here, we expand the toolbox for thermal control of *E. coli* through both direct cold-induced gene expression and through the construction of genetic circuits to invert heat-induced gene expression.

We accomplish direct induction at low temperatures through the use of temperature-sensitive mutants of λ repressor as transcriptional activators. In addition, we show that a temperature-sensitive mutant of λ repressor can serve as an activator and a repressor of different genes simultaneously in one genetic circuit, leading to opposite thermal responses and serving as a temperature switch.

Next, we demonstrate inversion of a temperature-sensitive repressor using a temperature insensitive repressor. We apply this multicomponent switch to engineer a temperature self-regulation circuit for *E. coli*-based ELMs. Seasonal variation in ambient temperature presents a challenge in deploying ELMs outside of a laboratory environment, because *E. coli* growth rate is impaired both below and above 37°C. Our construct enables *E. coli* to produce a light-absorptive pigment in response to environmental temperature below 36°C with the goal of allowing the cells to absorb sunlight and locally warm to their optimal growth temperature. We demonstrate the efficacy of our pigment temperature switch in a model flat ELM growing at 32°C and 42°C in a home-built illuminated growth chamber. Below 36°C, our engineered E. coli increase in pigmentation, causing an increase in sample temperature and growth rate above non-pigmented bacteria. On the other hand, above 36°C, they decrease in pigmentation, protecting their growth compared to bacteria with temperature-independent high pigmentation. Integrating our temperature homeostasis circuit into an ELM has the potential to improve ELM performance by optimizing growth and protein production in the face of seasonal temperature changes.

PUBLISHED CONTENT AND CONTRIBUTIONS

(1) Xiong, L. L.; Garrett, M. A.; Buss, M. T.; Kornfield, J. A.; Shapiro, M. G. *ACS Synthetic Biology* **2022**, Publisher: American Chemical Society, DOI: 10.1021/acssynbio.2c00093,
L.L.X. participated in conceiving the study, planned and performed experiments, analyzed data, and wrote the manuscript.

TABLE OF CONTENTS

LIST OF ILLUSTRATIONS

LIST OF TABLES

Chapter 1

INTRODUCTION

1.1 Temperature is a versatile input to engineered microbes

Since the birth of the field of synthetic biology at the dawn of this millennium, researchers have made tremendous progress in engineering cells for diverse applications [1–4]. Microbes, especially the bacterium *Escherichia coli* and the yeast *Saccharomyces cerevisiae*, are extensively used in synthetic biology because they are less complex than mammalian cells and tissues, and are well-characterized. Thus, they are well-suited as chassis for engineering genetic circuits. Engineered microbes are of interest as therapeutic and diagnostic agents [5–8], for use in bioremediation [9, 10], for use in sustainable agriculture [11], and as components or factories for engineered living materials [12–15]. Two decades in, the field has matured to the point where commercial products using synthetic biology tools are available, including a plant-based burger incorporating yeast-fermented soy leghemoglobin (Impossible Foods) and a biological nitrogen fertilizer for corn based on an engineered γ-proteobacterium (Pivot Bio)[3]. This thesis focuses on the use of genetic circuits in *E. coli*, especially for application in engineered living materials.

It is no exaggeration to state that without the discovery of *E. coli* in neonatal feces by pediatrician Theodor Escherich, published in 1886, the modern field of biology would not exist in its present form [16]. By the mid-twentieth century, biologists had established *E. coli* as a model organism, because it is easy to grow and is nonpathogenic. The 1961 discoveries of the genetic code (i.e., that three-nucleotide codons of nucleic acids encode amino acids) by Crick *et al.* [17] and of the *lac* operon for regulation of lactose metabolism by Jacob and Monad [18] both took place in *E. coli* and laid the foundation for molecular biology and the study and engineering of regulatory circuits in synthetic biology.

In addition, with *E. coli* come bacteriophage, viruses that inject their genetic material into bacterial cells. These phages could be exploited by biologists — phage T4 was used in the study of the genetic code — or studied in their own right to glean new insights into genetic regulation. Bacteriophage λ has a genome of only 48.5 kb [19] (compared to 3.98 Mb - 5.86 Mb for *E. coli* [20]), but provided a wealth of information on transcriptional regulation through both repression and activation

[21–23]. Interestingly, a single transcriptional factor, λ repressor (CI) serves as a DNA damage-sensitive switch controlling the induction of phage λ from the lysogenic to the lytic phase by acting at a bidirectional promoter as a repressor of the expression of genes for the lytic cycle and as an activator of the expression of itself. A temperature-sensitive mutant of CI (CI857) has been derived from a heat-inducible mutant of λ [24, 25], and used extensively in bioengineering [26, 27].

Notably, the first synthetic biology genetic circuits, a toggle switch [28] and an oscillatory network [29], use CI857 or CI in conjunction with LacI, derived from the *E. coli lac* operon, and are implemented in *E. coli*.

To take full advantage of engineered microbes, we need tools for spatiotemporal control of the production of microbial products. Temperature can serve as a versatile input to engineered biological systems, as it is deeply penetrant and noninvasive, and can be applied with spatial specificity or globally, as desired [30]. Previous work in the Shapiro lab developed two families of tunable thermal bioswitches based on temperature-labile transcriptional repressors [31]. One class consists of mutants of CI857 (hereafter referred to as TcI), and the other of mutants of TlpA, derived from a virulence plasmid of *Salmonella typhimurium*. Gene expression gated by TcI and TlpA has large dynamic range due to tight repression below their threshold temperatures (39.5°C and 43.5°C, respectively) and strong activity of their cognate promoter when the repressors are inactivated by heating above their thresholds. In addition, these repressors are expected to be orthogonal to endogenous cellular machinery, unlike heat shock promoters.

To expand the application space for circuits using these repressors, with a particular focus on *in vivo* therapeutics and diagnostics, Piraner, Abedi *et al.* tuned the bioswitch activation temperatures by directed evolution. They generated mutants of TcI and TlpA using error-prone PCR, which were used to control the expression of mWasabi (GFP) [31]. They transformed *E. coli* with the mutant library and replica-plated to allow screening using a colony fluorescence assay. Colonies that did not fluoresce on a plate incubated below the desired temperature threshold, but did fluoresce on a plate incubated above the threshold, were selected for further characterization to determine the temperature profile of gene expression. From these experiments, two mutants of TcI and two mutants of TlpA were identified, giving a total of six bioswitches with temperature thresholds ranging from 36°C to 43.5°C.

In addition to these temperature-sensitive repressors, other researchers have used

heat shock factors [32] and 5' UTR RNA hairpins [33–36] to turn on gene expression in response to increases in temperature. However, microbial heat shock promoters exhibit low dynamic range and have low specificity — they can be induced by chemical stress. In addition, as components of the native cell machinery, may be difficult to tune in an orthogonal manner. On the other hand, RNA thermometers can be designed to be orthogonal and are easily tuned, but also have low dynamic range and do not transition as sharply as TcI and TlpA.

Some applications may require sensing decreases in temperature, rather than increases in temperature. For example, we may want to program microbial therapeutics to self-destruct in response to leaving the body [37–39]. Additionally, for environmental, agricultural, or living materials applications, we could engineer adaptive measures beyond the native cold shock pathway [40], which suffers from lack of tunability [41]. Few additional natural cold-inducible switches have been reported [42–44].

A recent synthetic cold-inducible switch couples temperature-sensitive proteolytic and transcriptional regulation for tight control of gene expression [45]. Zheng, Meng *et al.* evolved tobacco etch virus (TEV) protease to be heat-inactivated and the CI repressor of bacteriophage 434 (CI434) — with the TEV protease cleavage site inserted — to be cold-inactivated. The CI434 mutant, constitutively expressed, gates the expression of the TEV protease mutant and GFP. At low temperature, the cold-inactivated CI434 mutant decreases in function, allowing for expression of protease and GFP. The effect is amplified by degradation of the CI434 mutant by the protease. At high temperature, the CI434 mutant represses expression of the protease and of GFP, while the heat-inactivated protease also decreases in function. Combining proteolytic and transcriptional regulation improves the dynamic range of the switch over the performance of either the cold-inactivated CI434 mutant or the heat-inactivated TEV protease on their own.

Another recent synthetic cold-inducible switch uses a split-T7 RNA polymerase fused with the temperature-sensitive domains of TlpA, using the coiled-coils to directly control whether transcription can occur [46]. With constitutive expression of the N-terminal based and C-terminal based fusion proteins in *E. coli*, their system exhibited sharp thermal switching centered at 37.5°C. They tuned their system by changing the stoichiometry of N-terminal based and C-terminal based fusion proteins via changing the promoters from which they were expressed. This system is highly reversible, as demonstrated by dynamic control experiments where *E.*

coli containing their constructs underwent thermal cycles of several hours at 37°C followed by several hours at 30°C, repeated.

1.2 Use of *E. coli* in engineered living materials requires consideration of environmental temperature

Engineered living materials (ELMs) is a newer area of research combining synthetic biology, metabolic engineering, and materials science. By either incorporating biological cells into a synthetic material, or by using living cells as biofactories for materials, properties of the living component — including self-assembly, self-healing, and signal sensing and responsiveness — can be imparted to the material. Because *E. coli* is a laboratory workhorse, it is commonly used in ELM research [13, 47–49].

As a commensal organism in the intestines of warm-blooded animals, *E. coli* is usually exposed to a stable temperature of about 37°C, maintained by the host. In the laboratory, the minimum temperature for growth of *E. coli* is about 7.5°C in minimal media [50]. A smaller decrease from 37°C to 25°C reduces the growth rate of *E. coli* cultures in exponential phase by about 38% [51]. The observed reduction in growth rate with temperature correlates with reduced ability to synthesize protein. Outside of the laboratory, when *E. coli* cells leave the intestines, they are exposed to fluctuations not only in temperature, but also nutrients and moisture. Absent sources of fecal contamination, *E. coli* live in freshwater and soil only in tropical ecosystems, which maintain a steady temperature, nutrient level, and humidity amenable to its growth [52]. In addition, not only is low temperature harmful to *E. coli*, exposure to temperature above 37°C also inhibits its growth due to protein instability [53]. To deploy *E. coli*-based ELMs in outdoor applications outside of the tropics, the *E. coli* will require protection from both low and high ambient temperature to preserve the growth rate and protein production levels needed to grow and functionalize the material.

1.3 Outline of this thesis

In this thesis, we develop the TcI and TlpA transcription factors for use in cold-inducible gene circuits, with applications in thermal homeostasis for living materials. In Chapter 2, we discuss the use of TcI mutants for direct gene induction with low temperature and to create a one-component temperature state switch. In Chapter 3, we explore inversion of heat-inducible TcI and TlpA repression by additional regulatory components. In Chapter 4, we apply a cold-inducible TlpA-based circuit

for production of light-absorptive pigment at low temperature by *E. coli* in a model flat ELM. Chapter 5 comprises our conclusions and suggestions for further study.

References

(1) Cameron, D. E.; Bashor, C. J.; Collins, J. J. *Nature Reviews Microbiology* **2014**, *12*, Number: 5 Publisher: Nature Publishing Group, 381–390.

(2) Ford, T. J.; Silver, P. A. *Current Opinion in Chemical Biology* **2015**, *28*, 20–28.

(3) Voigt, C. A. *Nature Communications* **2020**, *11*, Number: 1 Publisher: Nature Publishing Group, 6379.

(4) Meng, F.; Ellis, T. *Nature Communications* **2020**, *11*, Number: 1 Publisher: Nature Publishing Group, 5174.

(5) Archer, E. J.; Robinson, A. B.; Süel, G. M. *ACS Synthetic Biology* **2012**, *1*, Publisher: American Chemical Society, 451–457.

(6) Danino, T.; Prindle, A.; Kwong, G. A.; Skalak, M.; Li, H.; Allen, K.; Hasty, J.; Bhatia, S. N. *Science Translational Medicine* **2015**, *7*, 289ra84.

(7) Ainsworth, C. *Nature* **2020**, *577*, Bandiera_abtest: a Cg_type: Outlook Number: 7792 Publisher: Nature Publishing Group Subject_term: Synthetic biology, Microbiology, Microbiome, Therapeutics, S20–S22.

(8) Abedi, M. H.; Yao, M. S.; Mittelstein, D. R.; Bar-Zion, A.; Swift, M. B.; Lee-Gosselin, A.; Barturen-Larrea, P.; Buss, M. T.; Shapiro, M. G. *Nature Communications* **2022**, *13*, Number: 1 Publisher: Nature Publishing Group, 1585.

(9) Pieper, D. H.; Reineke, W. *Current Opinion in Biotechnology* **2000**, *11*, 262–270.

(10) Janssen, D. B.; Stucki, G. *Environmental Science: Processes & Impacts* **2020**, *22*, Publisher: The Royal Society of Chemistry, 487–499.

(11) Sudheer, S.; Bai, R. G.; Usmani, Z.; Sharma, M. *Current Genomics* **2020**, *21*, 321–333.

(12) Nguyen, P. Q.; Courchesne, N.-M. D.; Duraj-Thatte, A.; Praveschotinunt, P.; Joshi, N. S. *Advanced Materials* **2018**, *30*, 1704847.

(13) Gilbert, C.; Ellis, T. *ACS Synthetic Biology* **2019**, *8*, 1–15.

(14) Liu, S.; Xu *Frontiers in Sensors* **2020**, *1*, DOI: `10.3389/fsens.2020.586300`.

(15) Duncker, K. E.; Holmes, Z. A.; You, L. *Microbial Cell Factories* **2021**, *20*, 211.

(16) Hacker, J.; Blum-Oehler, G. *Nature Reviews Microbiology* **2007**, *5*, Number: 12 Publisher: Nature Publishing Group, 902–902.

(17) Crick, F. H. C.; Barnett, L.; Brenner, S.; Watts-Tobin, R. J. *Nature* **1961**, *192*, Number: 4809 Publisher: Nature Publishing Group, 1227–1232.

(18) Monod, J.; Jacob, F. *Cold Spring Harbor Symposia on Quantitative Biology* **1961**, *26*, 389–401.

(19) *NCBI Nucleotide Database* **2020**, GenBank: J02459.1.

(20) Kurylo, C. M.; Alexander, N.; Dass, R. A.; Parks, M. M.; Altman, R. A.; Vincent, C. T.; Mason, C. E.; Blanchard, S. C. *Genome Biology and Evolution* **2016**, *8*, 742–752.

(21) Ptashne, M.; Backman, K.; Humayun, M. Z.; Jeffrey, A.; Maurer, R.; Meyer, B.; Sauer, R. T. *Science* **1976**, Publisher: American Association for the Advancement of Science, DOI: 10.1126/science.959843.

(22) Ptashne, M.; Jeffrey, A.; Johnson, A. D.; Maurer, R.; Meyer, B. J.; Pabo, C. O.; Roberts, T. M.; Sauer, R. T. *Cell* **1980**, *19*, 1–11.

(23) Ptashne, M., *A Genetic Switch: Phage Lambda Revisited*; CSHL Press: 2004; 172 pp.

(24) Lieb, M. *Journal of Molecular Biology* **1966**, *16*, 149–163.

(25) Lieb, M. *Molecular and General Genetics MGG* **1981**, *184*, 364–371.

(26) Elvin, C. M.; Thompson, P. R.; Argall, M. E.; Hendry, P.; Stamford, N. P. J.; Lilley, P. E.; Dixon, N. E. *Gene* **1990**, *87*, 1230125.

(27) Jechlinger, W.; Glocker, J.; Haidinger, W.; Matis, A.; Szostak, M. P.; Lubitz, W. *Journal of Biotechnology* **2005**, *116*, 11–20.

(28) Gardner, T. S.; Cantor, C. R.; Collins, J. J. *Nature* **2000**, *403*, 339–342.

(29) Elowitz, M. B.; Leibler, S. *Nature* **2000**, *403*, Number: 6767 Publisher: Nature Publishing Group, 335–338.

(30) Piraner, D. I.; Farhadi, A.; Davis, H. C.; Wu, D.; Maresca, D.; Szablowski, J. O.; Shapiro, M. G. *Biochemistry* **2017**, *56*, Publisher: American Chemical Society, 5202–5209.

(31) Piraner, D. I.; Abedi, M. H.; Moser, B. A.; Lee-Gosselin, A.; Shapiro, M. G. *Nature Chemical Biology* **2017**, *13*, 75–80.

(32) Zhao, K.; Liu, M.; Burgess, R. R. *Journal of Biological Chemistry* **2005**, *280*, 17758–17768.

(33) Neupert, J.; Karcher, D.; Bock, R. *Nucleic Acids Research* **2008**, *36*, e124.

(34) Waldminghaus, T.; Kortmann, J.; Gesing, S.; Narberhaus, F. **2008**, *389*, Publisher: De Gruyter Section: Biological Chemistry, 1319–1326.

(35) Kortmann, J.; Sczodrok, S.; Rinnenthal, J.; Schwalbe, H.; Narberhaus, F. *Nucleic Acids Research* **2011**, *39*, 2855–2868.

(36) Sen, S.; Apurva, D.; Satija, R.; Siegal, D.; Murray, R. M. *ACS Synthetic Biology* **2017**, *6*, Publisher: American Chemical Society, 1461–1470.

(37) Chan, C. T. Y.; Lee, J. W.; Cameron, D. E.; Bashor, C. J.; Collins, J. J. *Nature Chemical Biology* **2016**, *12*, Number: 2 Publisher: Nature Publishing Group, 82–86.

(38) Stirling, F.; Bitzan, L.; O'Keefe, S.; Redfield, E.; Oliver, J. W. K.; Way, J.; Silver, P. A. *Molecular Cell* **2017**, *68*, 686–697.e3.

(39) Rottinghaus, A. G.; Ferreiro, A.; Fishbein, S. R. S.; Dantas, G.; Moon, T. S. *Nature Communications* **2022**, *13*, Number: 1 Publisher: Nature Publishing Group, 672.

(40) Gualerzi, C. O.; Maria Giuliodori, A.; Pon, C. L. *Journal of Molecular Biology* **2003**, *331*, 527–539.

(41) Qing, G.; Ma, L.-C.; Khorchid, A.; Swapna, G. V. T.; Mal, T. K.; Takayama, M. M.; Xia, B.; Phadtare, S.; Ke, H.; Acton, T.; Montelione, G. T.; Ikura, M.; Inouye, M. *Nature Biotechnology* **2004**, *22*, Number: 7 Publisher: Nature Publishing Group, 877–882.

(42) Hoynes-O'Connor, A.; Hinman, K.; Kirchner, L.; Moon, T. S. *Nucleic Acids Research* **2015**, *43*, 6166–6179.

(43) Giuliodori, A. M.; Di Pietro, F.; Marzi, S.; Masquida, B.; Wagner, R.; Romby, P.; Gualerzi, C. O.; Pon, C. L. *Molecular Cell* **2010**, *37*, 21–33.

(44) Kamp, H. D.; Higgins, D. E. *Molecular Microbiology* **2009**, *74*, 421–435.

(45) Zheng, Y.; Meng, F.; Zhu, Z.; Wei, W.; Sun, Z.; Chen, J.; Yu, B.; Lou, C.; Chen, G.-Q. *Nucleic Acids Research* **2019**, *47*, e137.

(46) Chee, W. K. D.; Yeoh, J. W.; Dao, V. L.; Poh, C. L. *ACS Synthetic Biology* **2022**, *11*, Publisher: American Chemical Society, 921–937.

(47) Heyde, K. C.; Scott, F. Y.; Paek, S.-H.; Zhang, R.; Ruder, W. C. *JoVE (Journal of Visualized Experiments)* **2017**, e55300.

(48) Duraj-Thatte, A. M.; Courchesne, N.-M. D.; Praveschotinunt, P.; Rutledge, J.; Lee, Y.; Karp, J. M.; Joshi, N. S. *Advanced Materials* **2019**, *31*, _eprint: https://onlinelibrary.wiley.com/doi/pdf/10.1002/adma.201901826, 1901826.

(49) Guo, S. et al. *ACS Synthetic Biology* **2020**, *9*, Publisher: American Chemical Society, 475–485.

(50) Shaw, M. K.; Marr, A. G.; Ingraham, J. L. *Journal of Bacteriology* **1971**, *105*, 683–684.

(51) Broeze, R. J.; Solomon, C. J.; Pope, D. H. *Journal of Bacteriology* **1978**, *134*, 861–874.

(52) Winfield, M. D.; Groisman, E. A. *Applied and Environmental Microbiology* **2003**, *69*, Publisher: American Society for Microbiology, 3687–3694.

(53) Rudolph, B.; Gebendorfer, K. M.; Buchner, J.; Winter, J. *The Journal of Biological Chemistry* **2010**, *285*, 19029–19034.

Chapter 2

DIRECT GENE INDUCTION WITH COOLING AND CONTROL OF TWO GENES WITH OPPOSITE THERMAL RESPONSE PROFILES WITH ONE TRANSCRIPTION FACTOR

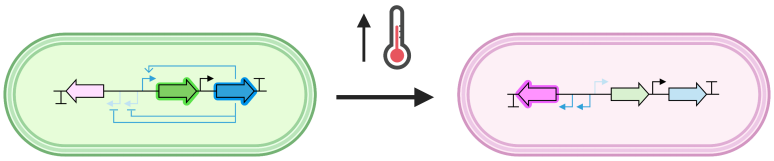

Adapted from:

(1) Xiong, L. L.; Garrett, M. A.; Buss, M. T.; Kornfield, J. A.; Shapiro, M. G. *ACS Synthetic Biology* **2022**, Publisher: American Chemical Society, DOI: 10.1021/acssynbio.2c00093,

2.1 Introduction

Spatiotemporal control of engineered microbes enables patterning and localization of microbial activity in applications ranging from in vivo therapeutics to engineered living materials. Temperature can be applied globally or with spatial specificity as a deeply penetrant, noninvasive input signal [1]. Previous work developed two families of orthogonal tunable thermal bioswitches based on bacteria- and phage-derived transcriptional repressor [2]. These gene circuit components, along with most other currently-used bacterial temperature-dependent regulators, such as heat shock factors and 5' UTR RNA hairpins, turn on gene expression in response to increases in temperature [3–7], whereas few synthetic or natural cold-inducible switches have been reported [8–11]. However, induction of gene expression based on decreases in temperature would, for example, allow for programming microbial therapeutics to self-destruct in response to leaving the body [12–14] or engineering microbe-based living materials to activate adaptive measures beyond the native cold shock pathway [15] in response to decreases in ambient temperature. Most existing sensors for decreases in temperature, such as the native cold shock response,

suffer from lack of tunability, narrowing the range of possible applications [16]. Meanwhile, the inversion of hot-on bioswitches to obtain cold-on responses by adding enzymatic degradation [8], antirepressors [11], or additional repressors [2] increases gene circuit complexity.

One of the most promising classes of thermal bioswitch repressors are mutants of CI857 [17, 18] (here referred to as TcI39). This mutant of bacteriophage Lambda repressor CI has been tuned by directed evolution to transition at different setpoint temperatures while retaining sharp switching behavior [2]. To date, these mutated TcI transcription factors have been applied only as repressors for hot-on gene expression, acting at cognate promoters PR and PL. However, in nature, wildtype CI also activates transcription at promoter PRM, which allows it to serve as a DNA damage-sensitive switch controlling the induction of phage Lambda from the lysogenic to the lytic phase [19, 20]. Previous interest in TcI39's ability to activate PRM involved expression of TcI39 itself from PRM, while the main purpose of TcI39 was to regulate hot-on expression of a protein of interest from the PR promoter [21, 22].

In this chapter, we examine the ability of tunable TcI proteins to serve as cold-on transcriptional activators of specific genes of interest. We demonstrate temperature-responsive activation by two TcI variants with transition setpoints at 35.5°C and 38.5°C in *E. coli*. In addition, we show that a single TcI protein can act simultaneously as a temperature-responsive repressor and activator of two separate genes in a single circuit, enacting complementary thermal regulation.

2.2 Results and discussion

TcI mutants act as tunable, temperature-sensitive transactivators

Different applications of thermal control may require different temperature thresholds for gene activation. Thus, we characterized the ability to activate transcription of two previously-developed mutants, TcI38 and TcI39, with bioswitch activation midpoints of 38°C and 39°C, respectively [2]. We constructed a model gene circuit driving the expression of the mWasabi green fluorescent protein (GFP) from the PRM promoter. In its native bacteriophage Lambda, CI binds three operator sites at the bidirectional PR/PRM promoter: OR1, OR2, and OR3. CI preferentially binds OR1 and then recruits its own binding to OR2, repressing PR and activating PRM [20]. At high concentrations, CI also binds to OR3 and represses PRM; we used a mutated OR3 to prevent this repression [23].

In our cold-on circuit, transcription from the PRM promoter is activated by either

TcI38 or TcI39, which is in turn expressed both from PRM readthrough and a weak constitutive LacI promoter (Figure 2.1.a). For comparison, we also constructed a circuit in which wildtype CI serves as the transactivator (Figure 2.1.b). Wildtype CI is nominally temperature independent; however, its ability to bind to operator DNA decreases gradually with increasing temperature [24], while its ability to activate PRM decreases below 37°C [25]. It was therefore important to compare TcI mutant activation profiles to wildtype CI at each temperature. Finally, we included a construct with no activator to measure the thermal profile of background gene expression at the PRM promoter (2.1.c).

We quantified the gene expression level controlled by TcI38 or TcI39 via GFP fluorescence measured by flow cytometry in comparison with the level driven by wildtype CI or without an activator (Figure 2.2). At 32°C, each TcI mutant drives expression of GFP at levels greater than 75% of that generated by wildtype CI at the same temperature, and expression declines sharply with increasing temperature to a baseline set by the non-fluorescent control (Figure 2.3). TcI38 declines to 50% activation at 35.5°C, while TcI39 reaches 50% activation at 38.5°C. These effective transition temperatures are slightly downshifted from the midpoints observed when these proteins are acting as transcriptional repressors [2], suggesting that the interaction of TcI with its operator helps set its thermal setpoint.

TcI39 simultaneously activates and represses, serving as a temperature- controlled switch

After establishing the basic capabilities of tunable TcI activators, we endeavored to combine them with TcI repression. We assembled a construct wherein expression of GFP from the PRM promoter is activated by TcI39 and expression of mRFP1 (RFP) from the PR-PL tandem promoter is repressed by TcI39 (Figure 2.4). We assayed the thermal response of this genetic circuit in *E. coli* via GFP and RFP fluorescence measured by flow cytometry (Figure 2.5, 2.6). Bivariate fluorescence analysis reveals that at intermediate temperatures, individual cells express both GFP and RFP. Mean hot-on RFP expression shows a sharp increase with temperature above 37°C, consistent with previous work [2]. Meanwhile, the mean cold-on GFP expression response is similar to the standalone TcI39 activation operon (Figure 2.3.a), with slight upshifting of the transition temperature. We illustrated the differential expression of RFP and GFP above and below 39°C using *E. coli* incubated at 37°C and 44°C (Figure 2.7).

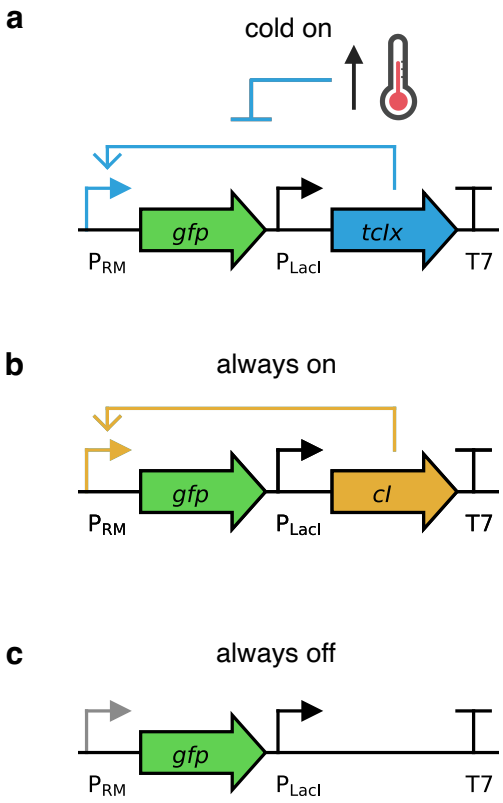

Figure 2.1: Circuit diagrams of gene activation constructs. TcIx (x = 38, 39) (a), wildtype CI (b), or no activator (c) activates expression of mWasabi (GFP) from the PRM promoter.

2.3 Discussion

Our results establish the use of temperature-sensitive CI mutants as heat-inactivated transcriptional activators with tunable setpoints. In addition, due to the dual nature of these transcription factors, they can be used to control the expression of two genes in one circuit complementarily, with one expressed below the thermal setpoint, and the other above. The two TcI variants tested in this study operate at distinct setpoints within a range convenient for bacterial synthetic biology applications. The range of available setpoints could be further widened through directed evolution of TcI [2]. Transcriptional activation by TcI mutants represents a *cool* new tool for global and local thermal control of cells.

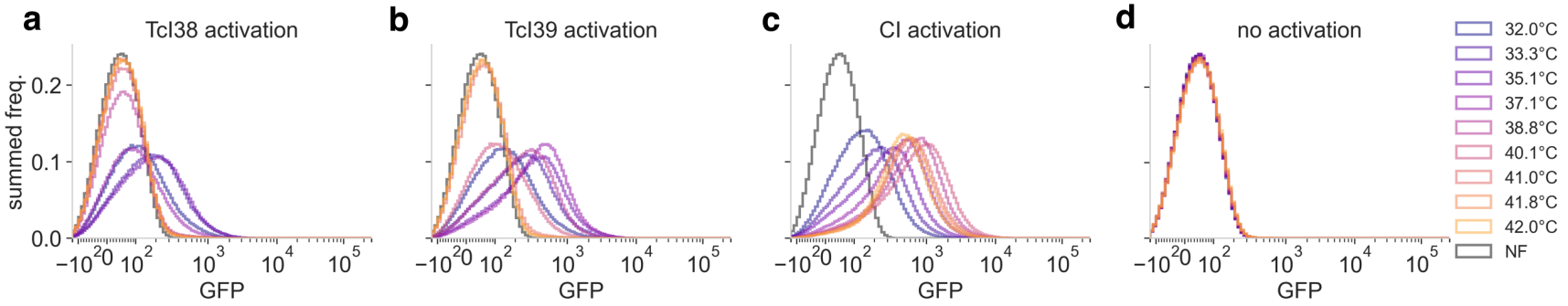

Figure 2.2: Summed frequency histograms for GFP channel for expression of GFP from PRM promoter by TcI39 (a), TcI38 (b), wildtype cI (c), or at baseline (no activator) (d). 8 h incubation, n = 4 biological replicates.

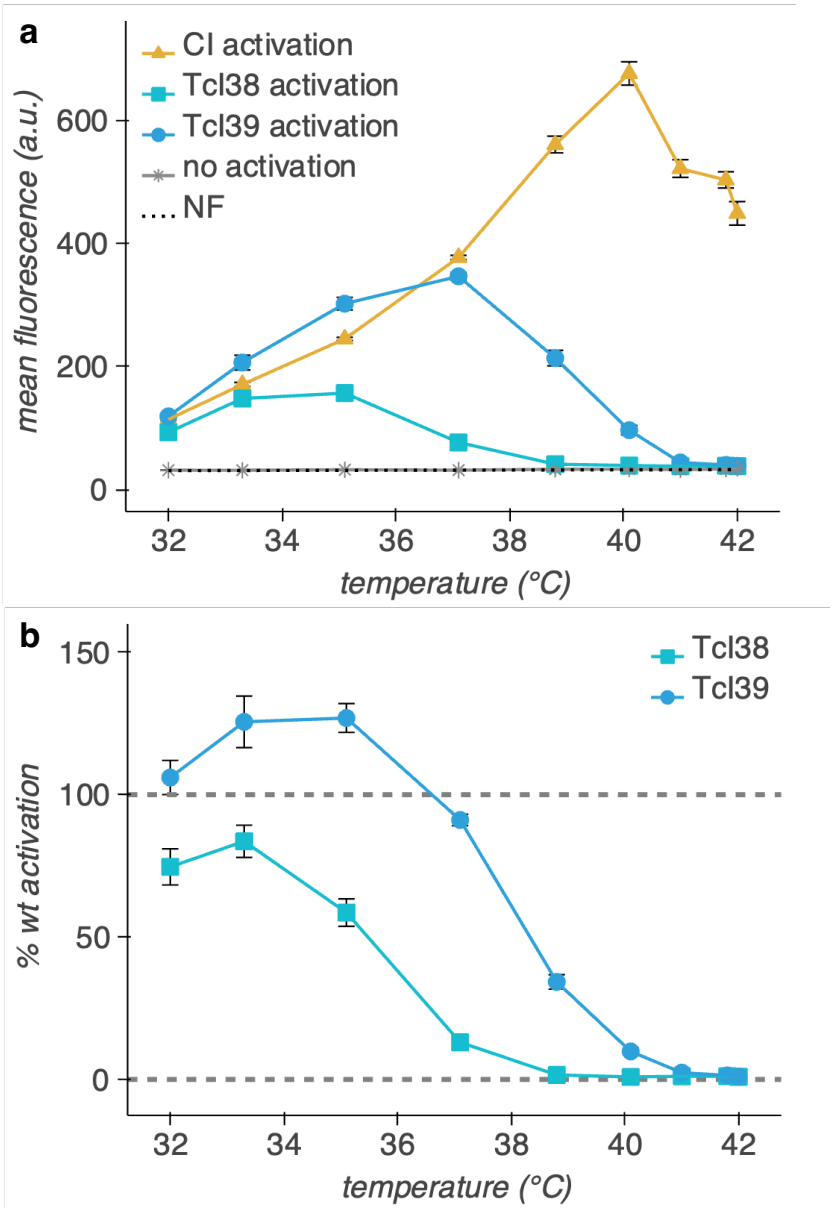

Figure 2.3: Mean population fluorescence and percent of wildtype activation for expression of GFP from PRM promoter by TcI38 and TcI39. (a) Thermal profile of mean population fluorescence of GFP expressed from the PRM promoter with activation by TcI38, TcI39, and wildtype CI, or at baseline (no activator) in *E. coli*. (b) Thermal profile of % wildtype activation of gene expression by TcI38 and TcI39. At each temperature, 100% wildtype activation indicates expression equal to wildtype CI, and 0% activation indicates expression equal to unactivated PRM. 8 h incubation, n = 4 biological replicates. Error bars represent +/- S.E.M.

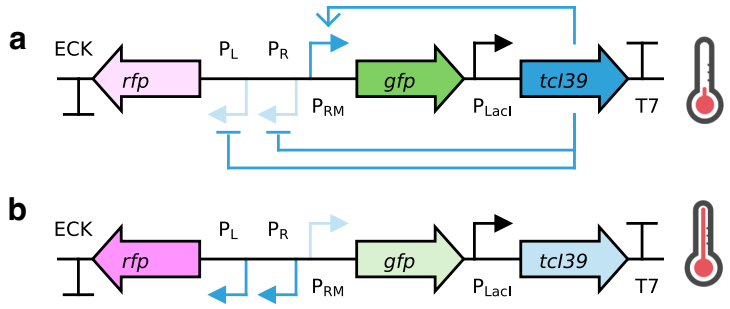

Figure 2.4: Circuit diagram of TcI39 state switch construct with state of regulation arcs indicated at low (a) and high (b) temperature. TcI39 activates expression of mWasabi (GFP) from the PRM promoter and represses expression of mRFP1 (RFP) from the PR-PL tandem promoter.

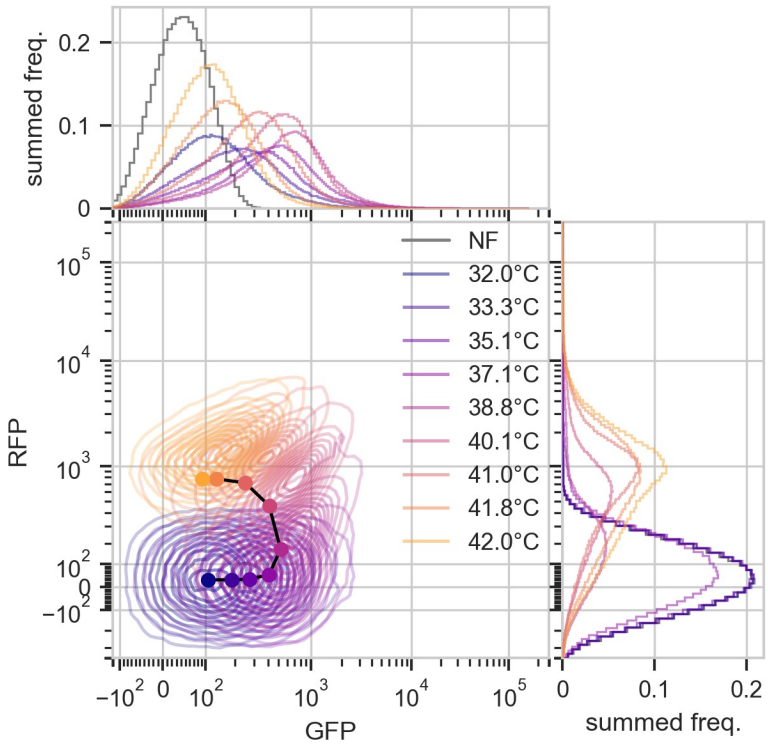

Figure 2.5: Thermal profile of correlation between GFP and RFP expression. Central plot: bivariate kernel density estimation for RFP channel and GFP channel. Points indicate geometric mean. Marginal plots: summed frequency histograms for RFP channel (right) and GFP channel (top). NF indicates nonfluorescent control measured in each channel (not shown in central plot for visual clarity; overlaps with 32.0, 33.3, 35.1°C histograms in RFP channel). 8 h incubation, n = 4 biological replicates.

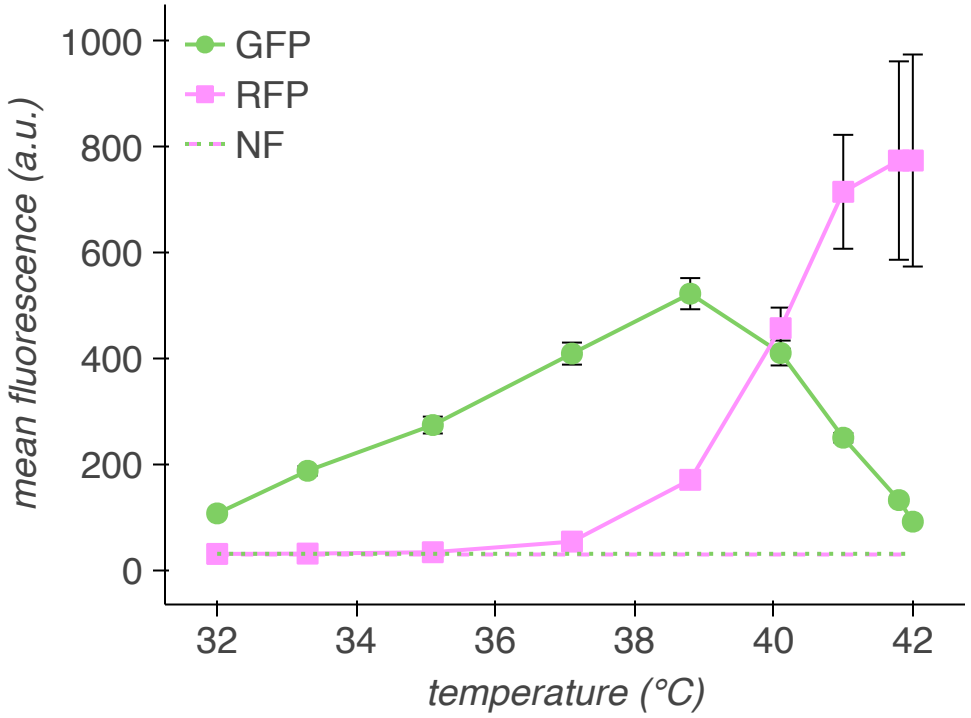

Figure 2.6: Thermal profile of mean population fluorescence of GFP and RFP expressed in *E. coli* containing the TcI39 state switch construct. 8 h incubation, n = 4 biological replicates. Error bars represent +/- S.E.M.

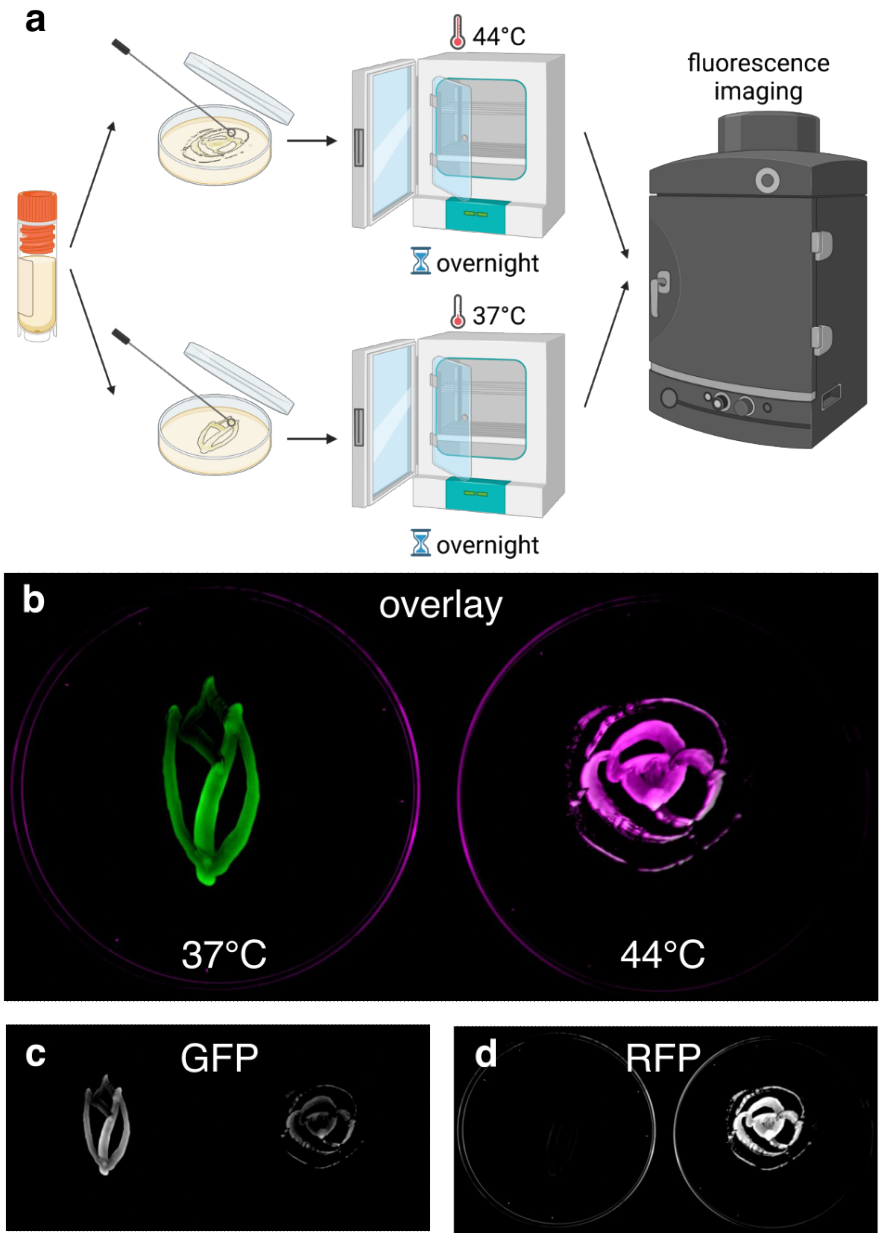

Figure 2.7: Illustration of experiment demonstrating differential gene expression with temperature. (a) We drew images on two agar plates using a glycerol stock of *E. coli* containing the TcI switch construct. We incubated each plate at a different temperature overnight before performing fluorescence imaging. (b) Overlay of GFP (green) and RFP (magenta) fluorescence images of *E. coli* containing the TcI switch construct, cultured on agar plates at 37°C (left) and 44°C (right). (c) GFP fluorescence image of plates in (b). (d) RFP fluorescence image of plates in (b). Color map limits were adjusted for each fluorophore to make the relative fluorescence levels of the two plates apparent. Parts of figure created with BioRender.com.

2.4 Materials and methods

Plasmid construction and molecular biology

All plasmids (Table 2.1) were designed using SnapGene (GSL Biotech) and assembled via reagents from New England Biolabs for KLD mutagenesis (E0554S) or HiFi Assembly (E2621L). After assembly, constructs were transformed into NEB Turbo (C2984I) E. coli for growth and plasmid preparation. Thermal gene expression regulation assays were performed in NEB Stable E. coli (C3040I). Integrated DNA Technologies synthesized all PCR primers. TcI38, TcI39, and mWasabi [26] (GFP) were obtained from our previous work [2]. mWasabi was tagged at the C-terminus with the DAS ssrA tag [27] (amino acid sequence AANDENYADAS). mRFP14 (RFP) was obtained from the pTU1-A-RFP plasmid [28], a gift from Paul Freemont (Addgene plasmid # 72939 ; http://n2t.net/addgene:72939 ; RRID:Addgene_72939). The transcriptional terminator referred to in Figure 2 as ECK is the ECK120029600 terminator [29] and was synthesized as a gBlock by Integrated DNA Technologies. Gene circuit diagrams were created using the DNAplotlib [30] library in Python.

Thermal regulation assays

Determination of temperature-dependent gene expression was performed using slight modifications from a previously-described method [2]. 1 mL cultures of 2x YT medium with 100 μg/mL ampicillin were inoculated with a single colony per culture and grown at 30°C, 250 rpm for 20 h. After dilution to OD600 = 0.1 in 2 mL LB (Sigma) with 100 μg/mL ampicillin, the cells were propagated at 30°C, 250 rpm until reaching OD600 = 0.25 as measured using a Nanodrop 2000c (Thermo Scientific) in cuvette mode. The cultures were dispensed in 50 μL aliquots into 8-well PCR strips (Bio-Rad) and incubated for 8 h in a thermal gradient using a DNA Engine Tetrad 2 Peltier Thermal Cycler (Bio-Rad) with the lid set to 50°C. After

Plasmid	**Transcriptional Regulator**	**Output Gene Product(s)**
pCIwt-PRM-Wasabi	CI	mWasabi
pTcI38-PRM-wasabi	TcI38	mWasabi
pTcI39-PRM-wasabi	TcI39	mWasabi
pBaseline-PRM-wasabi	none	mWasabi
pTcI39-state-switch	TcI39	mWasabi, mRFP1
pTlpA-wasabi-NF	TlpA	Nonfluorescent mWasabi (S71T, G73A)

Table 2.1: Genetic constructs used in this chapter.

thermal stimulus, cultures were immediately diluted 100-fold into PBS with 0.5% BSA and 1 mg/mL chloramphenicol and chilled on ice to stop protein expression.

Cell fluorescence was measured using a MACSQuant VYB flow cytometer (Miltenyi Biotec) with appropriate settings: FSC 400 V, SSC 250 V, Y2 (dsRed/txRed) 550 V, B1 (GFP/FITC) 520 V. At least 40,000 events were collected for each sample. NEB Stable *E. coli* transformed with the pTlpA-wasabi-NF plasmid (obtained from our previous work [2]) served as a non-fluorescent control. For each figure, all biological replicates and samples were measured in the same flow cytometry session.

All data analysis was performed using custom Python scripts with some functions from the Cytoflow [31] package. The geometric mean of fluorescence intensity was calculated using a bi-geometrical approach for negative and positive values [32]. Percent of wildtype activation was determined according to equation (2.1).

$$\% \text{ activation} = \frac{\text{avg } F - \text{avg } F_{\text{no CI}}}{\text{avg } F_{\text{CI}} - \text{avg } F_{\text{no CI}}} \tag{2.1}$$

Here, F is the geometric mean of fluorescence of a given sample at a given temperature, and avg F refers to the mean of 4 biological replicates. 1D and 2D histograms from biological replicates were combined for each circuit and temperature after weighting each count according to the total number of counts in its replicate. 1D histogram bins were chosen as the minimum of the number of bins given by the Freedman-Diaconis rule for each replicate for each circuit and temperature, with a lower limit of 100 bins. 2D histograms used 50 bins in each dimension. Bivariate kernel density estimation was performed using Gaussian kernels with bandwidths selected by Scott's rule, clipping evaluation to values below 1×10^4 for the GFP channel and values below 8×10^3 for the RFP channel. Logicle scale [33, 34] parameters were calculated using Cytoflow [35]. All data were plotted in Python using the Holoviews, Bokeh, and Matplotlib packages.

Plated illustrations of gene expression

Images were drawn on LB agar (Sigma) plates with 100 μg/mL ampicillin using a glycerol stock of E. coli containing the genetic circuit of interest. After incubation overnight at the temperatures of interest, the plates were imaged using a ChemiDoc MP Gel Imaging System (Bio-Rad). Filters used for RFP and GFP were the 530/28 filter and 605/50 filter, respectively. Colormap adjustments and color channel overlays were performed using ImageJ software [36].

2.5 Data and code availability

Plasmids are available through Addgene. Data analysis code is available on Github (https://github.com/shapiro-lab). All other materials and data are available from Mikhail G. Shapiro upon reasonable request.

2.6 Contributions and acknowledgements

L.L.X. and Mikhail G. Shapiro conceived the study. L.L.X., Michael A. Garrett, and Marjorie T. Buss planned and performed experiments. L.L.X. analyzed data. L.L.X. and M.G.S. wrote the manuscript based on this work that was published in *ACS Synthetic Biology* with input from all other authors. M.G.S. and Julia A. Kornfield supervised the research.

Thank you to Mohamad Abedi, Cameron Smith, Di Wu, and Deepak Mishra for helpful discussions. Flow cytometry was performed at the Caltech Flow Cytometry Facility. This research was supported by the Defense Advanced Research Project Agency (HR0011-17-2-0037 to M.G.S. and J.A.K.) and the Institute for Collaborative Biotechnologies (W911NF-19-D-0001 to M.G.S.). L.L.X. and M.T.B. were supported by the NSF Graduate Research Fellowship Program. M.A.G. was supported by the NIH MBRS Research Initiative for Scientific Enhancement Program. M.G.S. is an Investigator of the Howard Hughes Medical Institute. Related research in the Shapiro lab is supported by the David & Lucile Packard Foundation and the Dreyfus Foundation.

2.7 Supplementary information

This section includes (i) flow cytometry gating on forward and side scatter; (ii) flow cytometry fluorescence data by biological replicate; (iii) comparison between flow cytometry and bulk fluorescence data.

Flow cytometry gating on forward and side scatter

The input to our engineered system, temperature, has effects on baseline metabolism and viability of *E. coli*. Here, we display the forward scatter area (FSC-A) vs. side scatter area (SSC-A) for our samples at each temperature to which they were exposed. For each circuit, we observe a slight shift rightwards and upwards in the population distribution with increasing temperature.

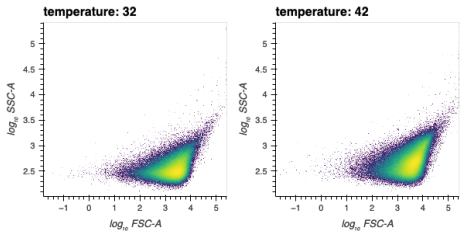

Figure 2.8: Forward scatter area (FSC-A) vs. side scatter area (SSC-A) for non-fluorescent control used to compare to gene expression from the PRM promoter at baseline (no activator) and with activation by TcI38, TcI39, wildtype CI (pooled data from 4 biological replicates).

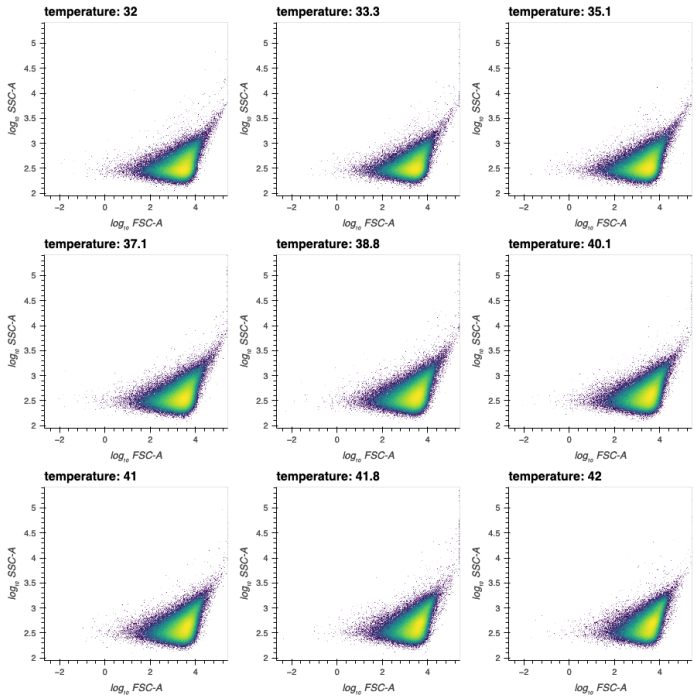

Figure 2.9: Forward scatter area (FSC-A) vs. side scatter area (SSC-A) for TcI38 activation samples (pooled data from 4 biological replicates).

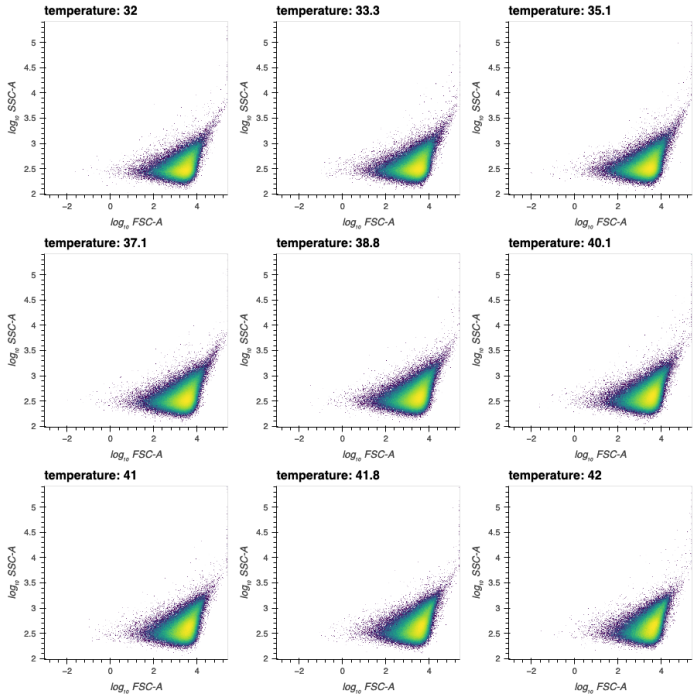

Figure 2.10: Forward scatter area (FSC-A) vs. side scatter area (SSC-A) for TcI39 activation samples (pooled data from 4 biological replicates).

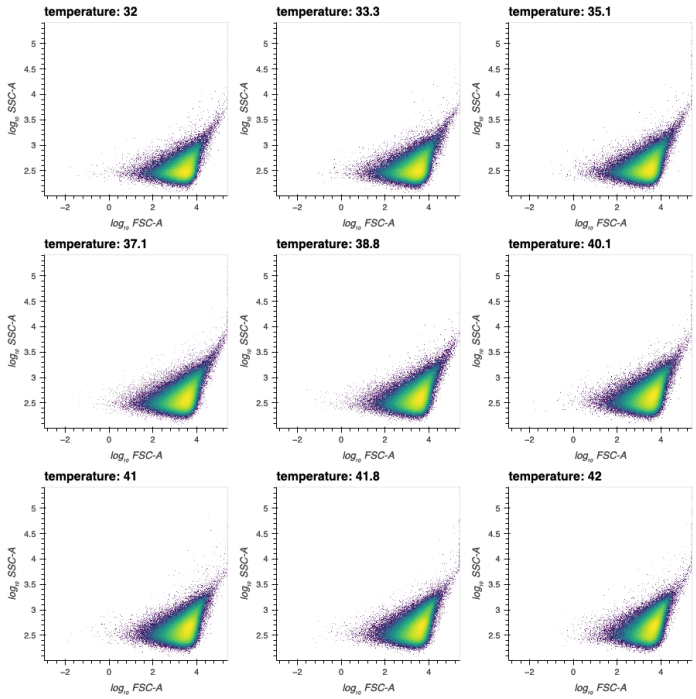

Figure 2.11: Forward scatter area (FSC-A) vs. side scatter area (SSC-A) for no activation samples (pooled data from 4 biological replicates).

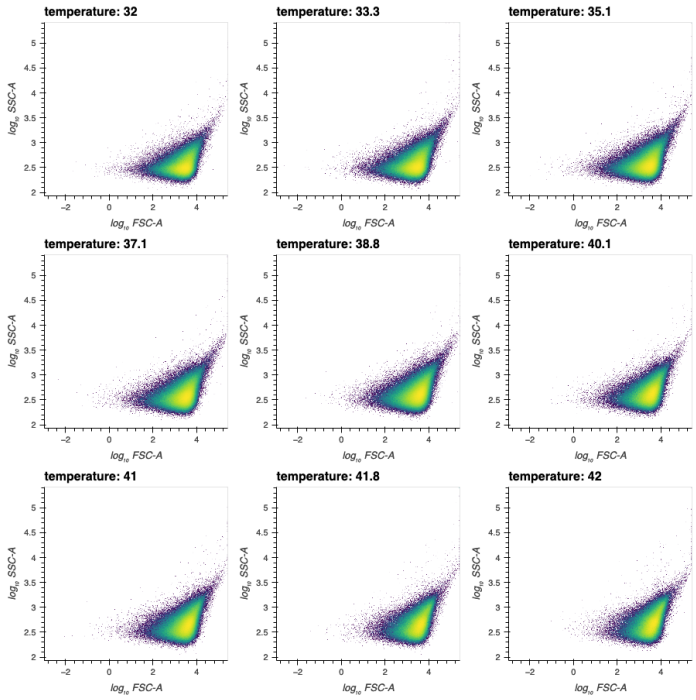

Figure 2.12: Forward scatter area (FSC-A) vs. side scatter area (SSC-A) for CI activation samples (pooled data from 4 biological replicates).

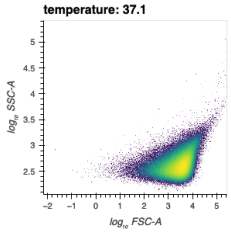

Figure 2.13: Forward scatter area (FSC-A) vs. side scatter area (SSC-A) for nonfluorescent control used to compare to gene expression by the TcI39 state switch construct (pooled data from 4 biological replicates).

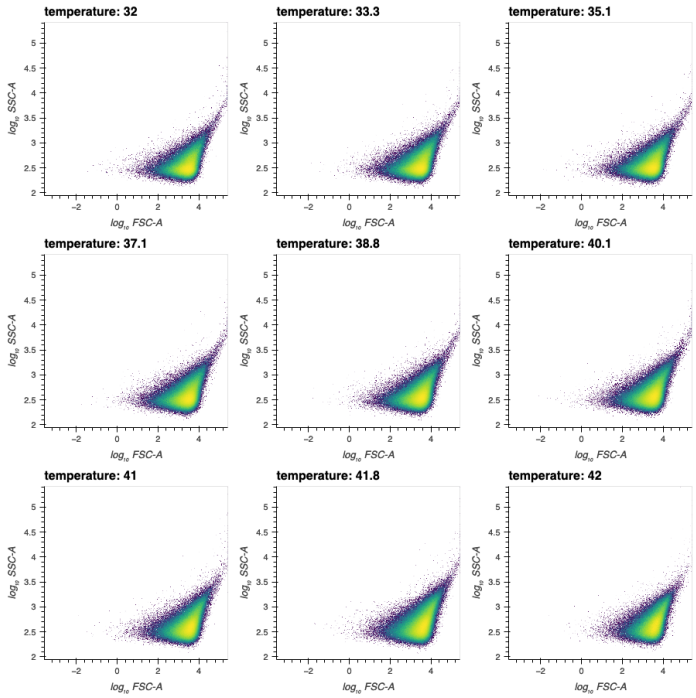

Figure 2.14: Forward scatter area (FSC-A) vs. side scatter area (SSC-A) for TcI39 state switch samples (pooled data from 4 biological replicates).

Flow cytometry fluorescence data by biological replicate

Here, we present flow cytometry fluorescence histograms and geometric means, separated by biological replicate. Each biological replicate is the set of samples grown at different temperatures derived from a single overnight culture grown from a single colony.

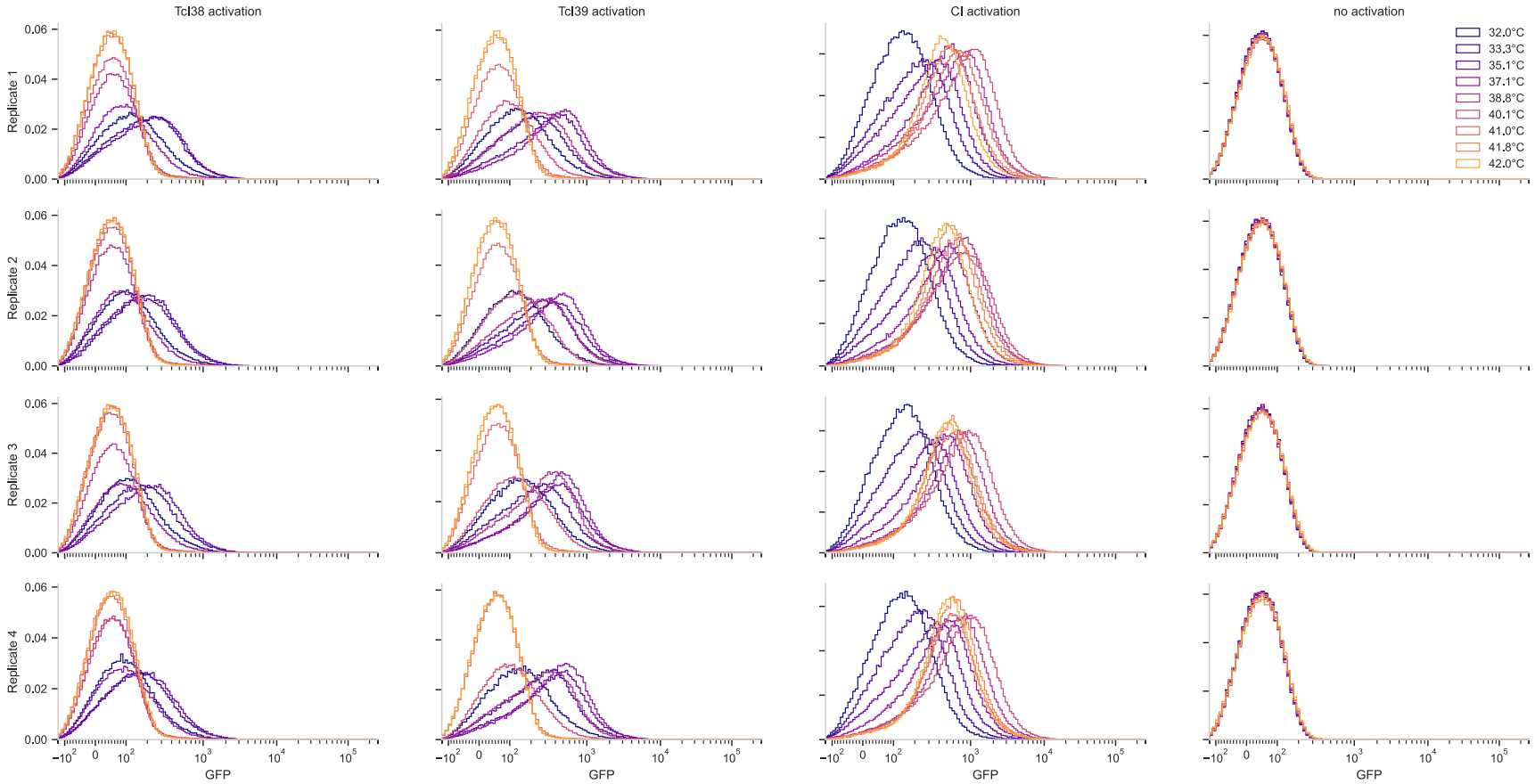

Figure 2.15: Frequency histograms for GFP channel for expression of mWasabi from PRM promoter by TcI38 (column 1), TcI39 (column 2), wildtype cI (column 3), or at baseline (no activator) (column 4), for each biological replicate (rows). Number of bins for each histogram determined by Freedman-Diaconis rule, with a minimum of 100 bins.

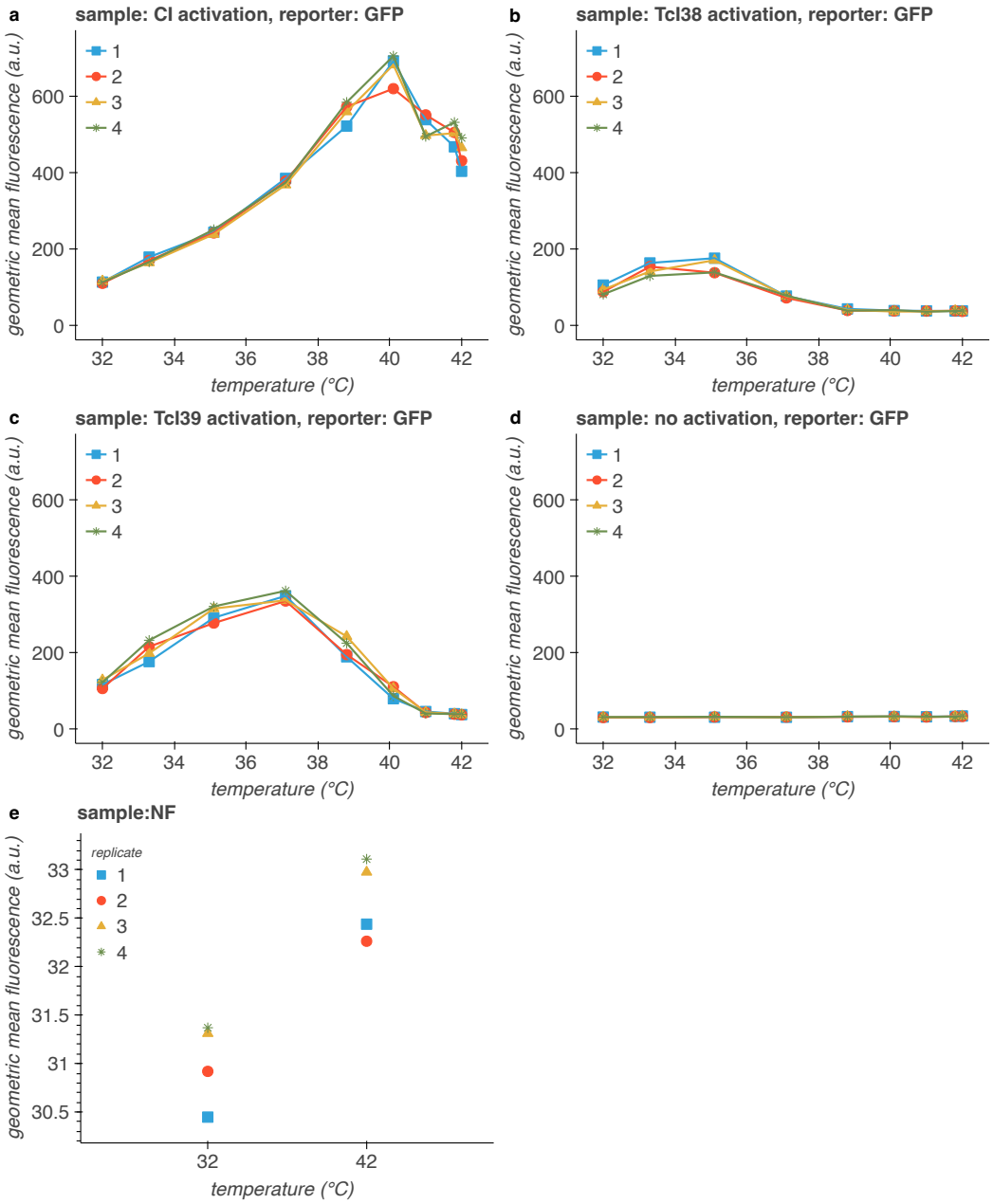

Figure 2.16: Geometric mean of fluorescence in GFP channel for expression of mWasabi from PRM promoter by cI (a), TcI38 (b), TcI39 (c), or at baseline (no activator) (d), for each biological replicate. (e) Geometric mean of fluorescence in GFP channel for each biological replicate of nonfluorescent control.

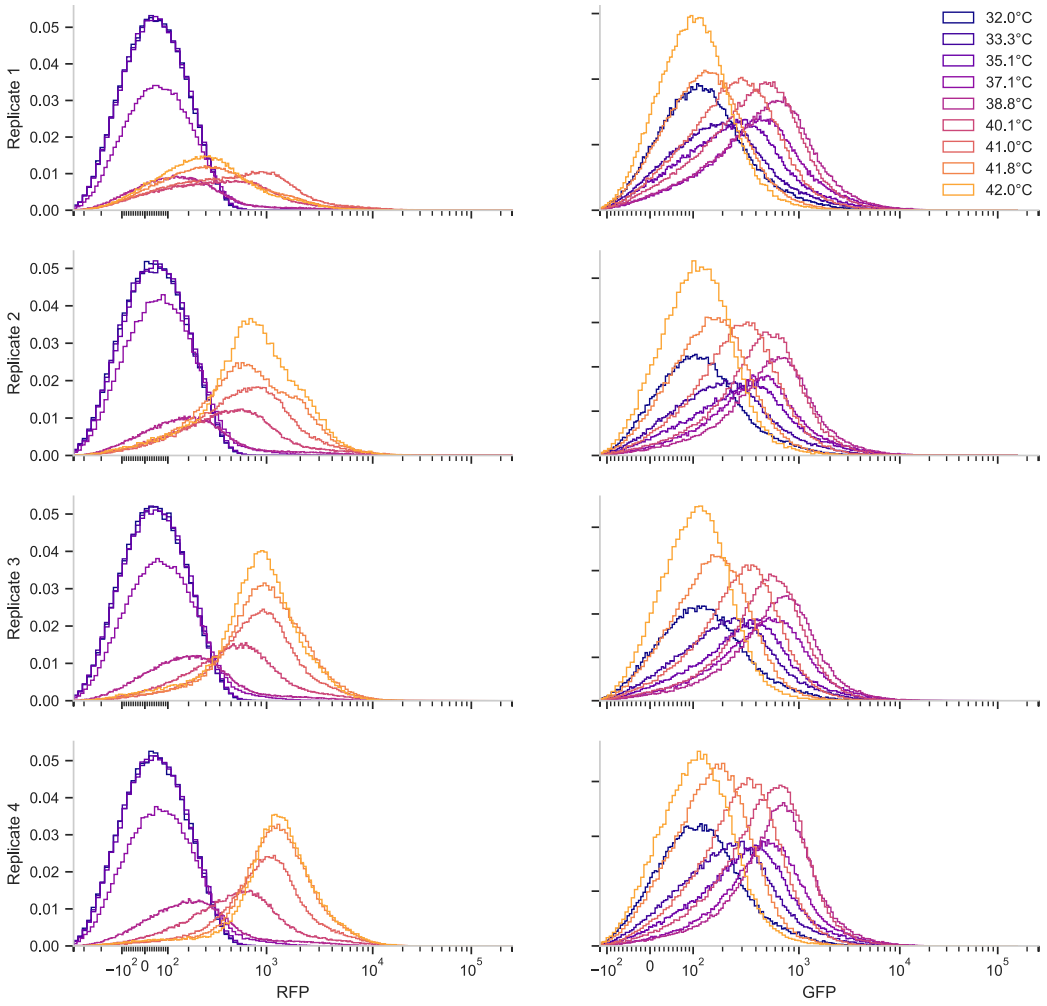

Figure 2.17: Frequency histograms for RFP channel (left) and GFP channel (right) for expression by TcI39 state switch construct, for each biological replicate (rows). Number of bins for each histogram determined by Freedman-Diaconis rule, with a minimum of 100 bins.

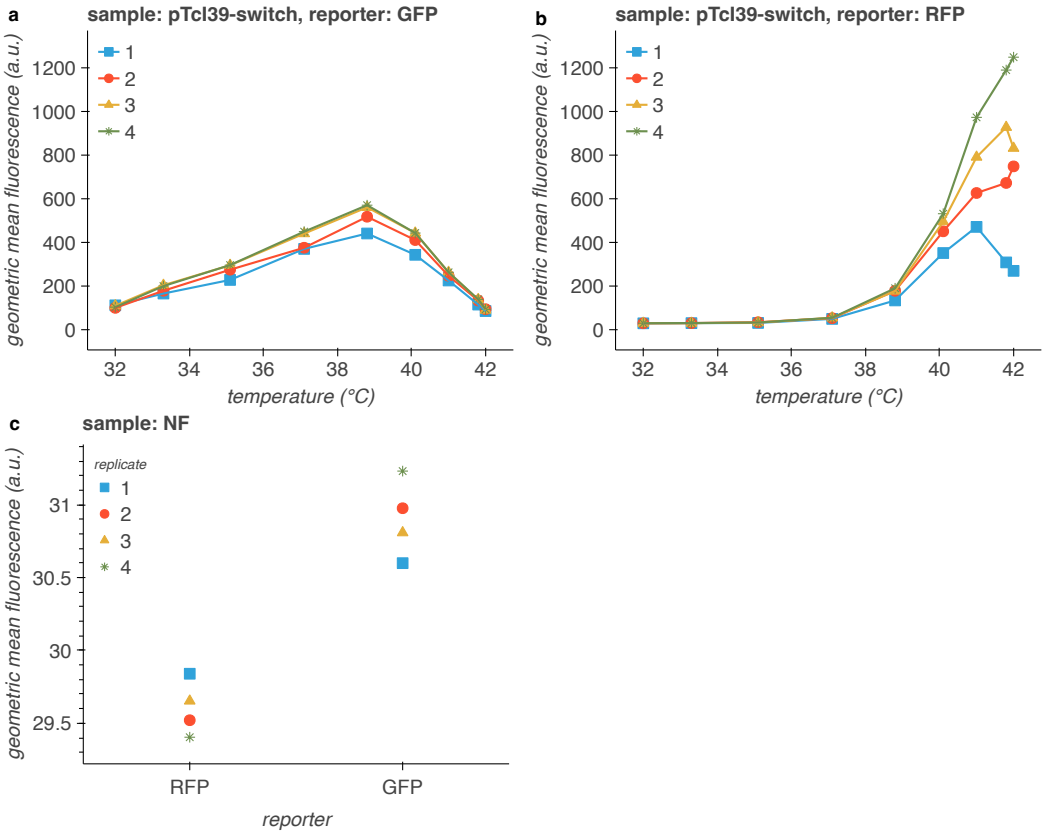

Figure 2.18: Geometric mean of fluorescence in GFP channel (a) and RFP channel (b) for expression by TcI39 state switch construct, for each biological replicate. (c) Geometric mean of fluorescence in GFP channel and RFP channel for nonfluorescent controls grown at 37.1°C.

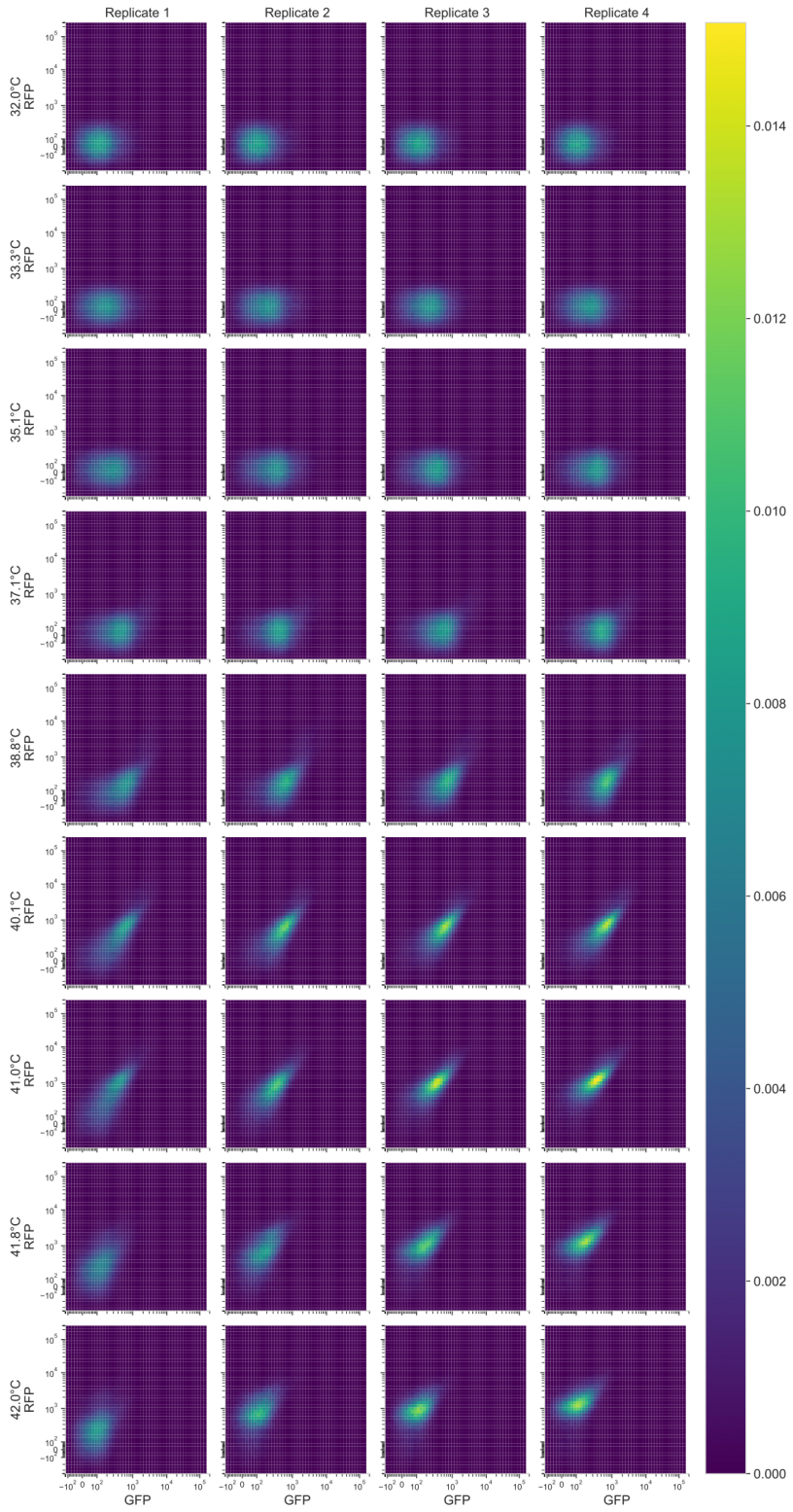

Figure 2.19: 2D frequency histograms for RFP channel and GFP channel for expression by TcI39 construct, for each biological replicate (columns). 50 bins in each dimension.

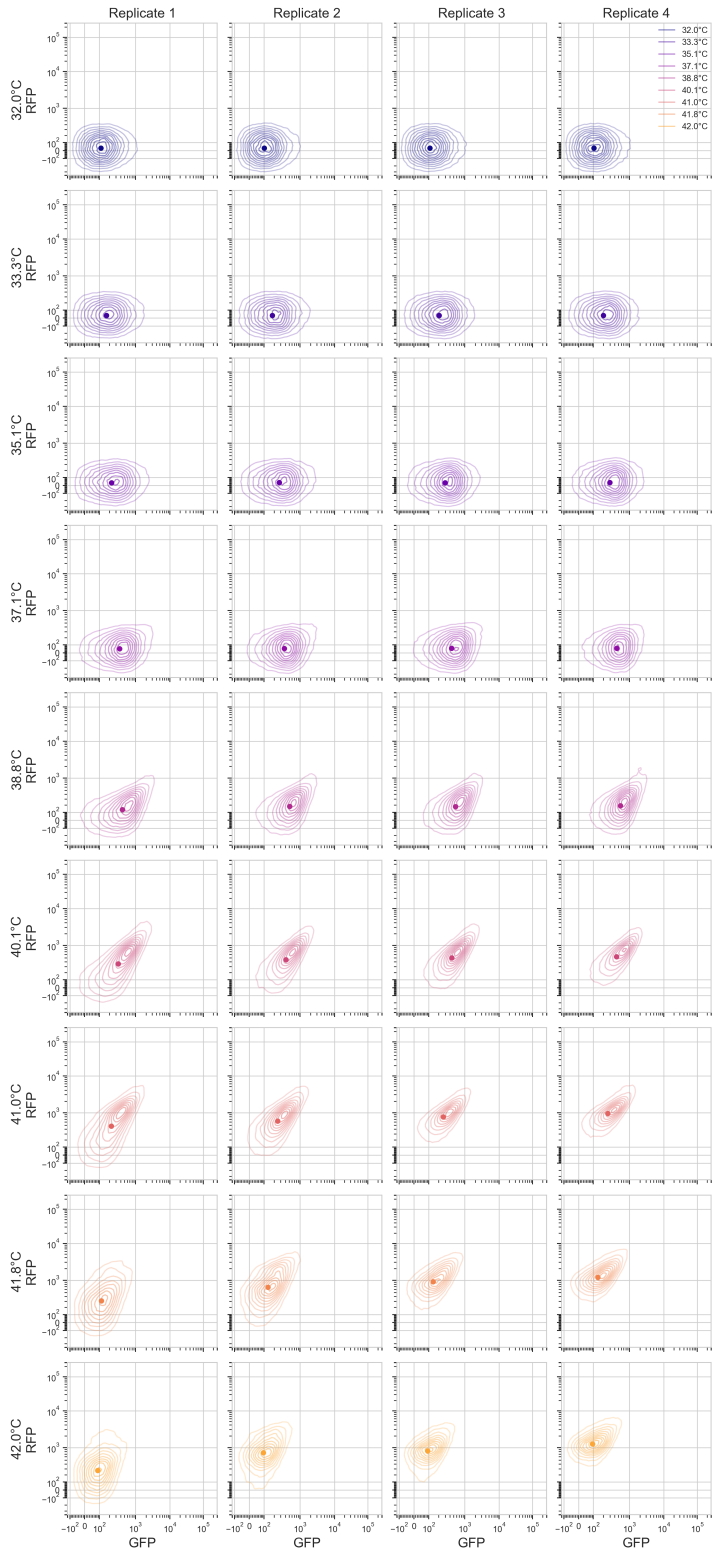

Figure 2.20: Bivariate kernel density estimation for RFP channel and GFP channel for expression by TcI39 construct, for each biological replicate (columns). 50 bins in each dimension.

Comparison with bulk fluorescence data

The fluorescence vs. temperature results presented in the main body of this chapter were measured by flow cytometry. Flow cytometry is a single-cell measurement technique; thus, in the case of the temperature state switch, it allows us to determine whether each cell in a population produces both green and red fluorescent protein, or whether the population splits into a green subpopulation and a red subpopulation (Figure 2.5). However, population-level averaging allows us to compare the measurements for each temperature and more easily detect trends. These results can be replicated by bulk measurement of population fluorescence using a plate reader or qPCR instrument, with normalization by OD600 measured by plate reader. Bulk measurements are faster and more accessible, and are especially suitable for quickly evaluating and comparing changes in circuit design or in experimental conditions.

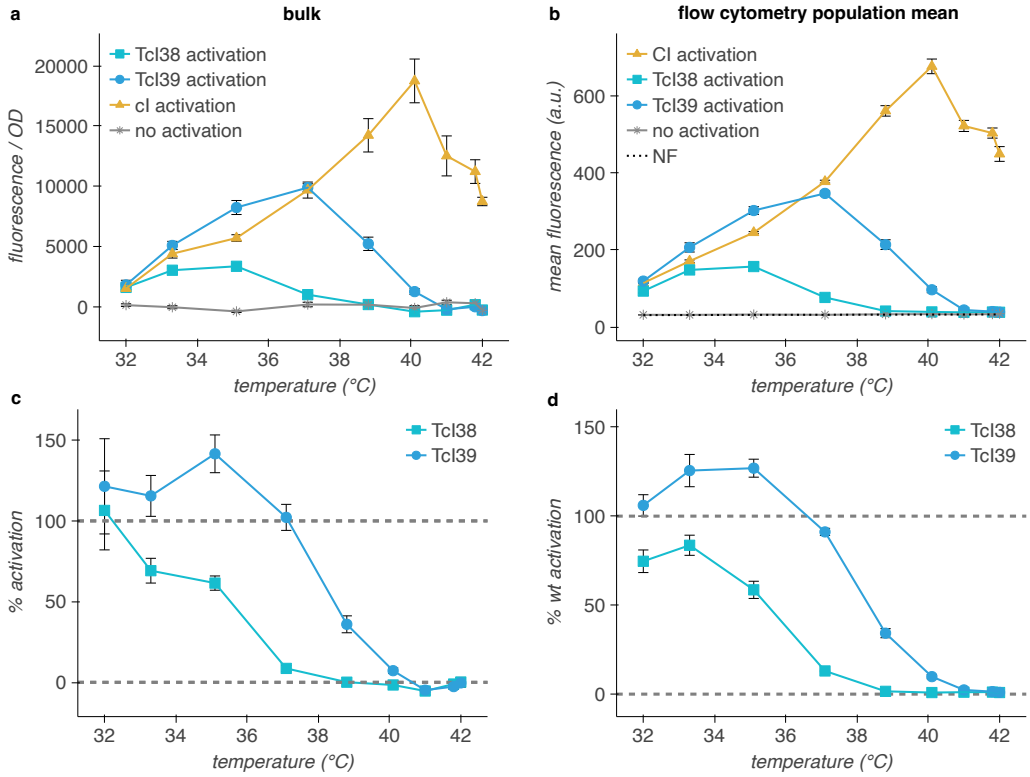

Figure 2.21: Bulk (a, c) and flow cytometry (b, d; repeated from figure 2.3) measurements of population-level fluorescence for TcI38, TcI39, wildtype CI, and no activation of GFP at temperatures ranging from 32 - 42°C. (a) Bulk fluorescence normalized by OD600. (b) Percent activation calculated from bulk OD-normalized fluorescence. (c) Geometric mean population fluorescence. (d) Percent activation calculated from geometric mean fluorescence. n = 4 biological replicates. Error bars represent +/- S.E.M. Bulk measurements at 12 h incubation; flow cytometry at 8 h incubation.

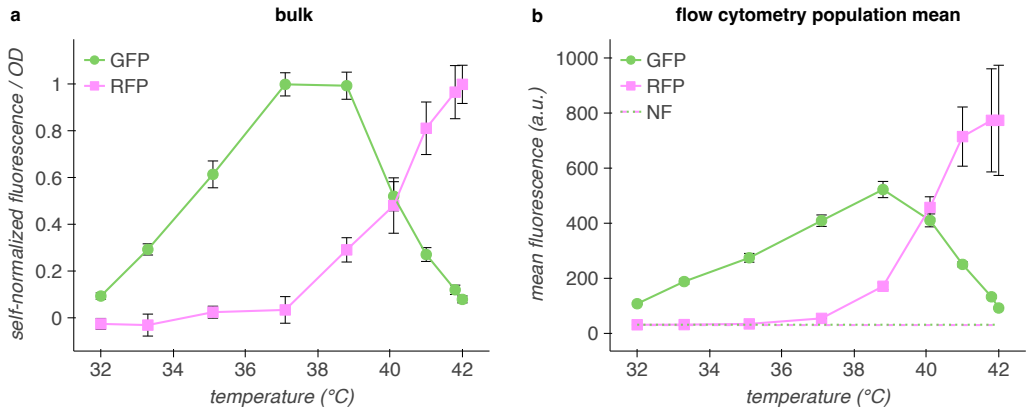

Figure 2.22: Bulk (a) and flow cytometry (b; repeated from figure 2.6) measurements of population-level fluorescence for TcI39 state switch at temperatures ranging from 32 - 42°C. (a) Bulk fluorescence normalized by OD600. Each channel normalized to its highest value. (b) Geometric mean population fluorescence. n = 4 biological replicates. Error bars represent +/- S.E.M. Bulk measurements at 12 h incubation; flow cytometry at 8 h incubation.

Determination of temperature-dependent gene expression was performed using slight modifications from a previously-described method [2]. 2 mL cultures of 2x YT medium with 100 μg/mL ampicillin were inoculated with a single colony per culture and grown at 30°C, 250 rpm for 20 h. After dilution to OD600 = 0.1 in LB (Sigma) with 100 μg/mL ampicillin, the cells were propagated at 30°C until reaching OD600 = 0.25 as measured using a Nanodrop 2000c (Thermo Scientific) in cuvette mode. The cultures were dispensed in 50 μL aliquots into 8-well PCR strips with optically transparent caps (Bio-Rad) and incubated for 12 hours in a thermal gradient using a DNA Engine Tetrad 2 Peltier Thermal Cycler (Bio- Rad) with the lid set to 50°C. After thermal stimulus, fluorescence was measured using a Stratagene MX3005p qPCR (Agilent). Filter sets used for RFP and GFP were ROX and FAM, respectively. Cultures were immediately diluted with 50 μL LB/amp and mixed, after which 90 μL was transferred into 96-well plates (Costar black/clear bottom) and OD600 was measured using a SpectraMax M5 plate reader (Molecular Devices). The background-corrected gene expression was determined according to equation 2.2, as described previously [2]. NEB Stable *E. coli* transformed with the pTlpA-wasabi-NF plasmid (obtained from our previous work [2]) served as the background.

$$E = \frac{F_{\text{raw}} - F_{\text{blank}}}{OD_{\text{raw}} - OD_{\text{blank}}} - \text{avg}(\frac{F_{\text{raw, BG}} - F_{\text{blank}}}{OD_{\text{raw, BG}} - OD_{\text{blank}}} \tag{2.2}$$

Here, F is the raw fluorescence and OD is the raw optical density at 600 nm of a given sample at a given temperature. Percent activation was determined according to equation 2.1, substituting background-corrected gene expression of a given sample at a given temperature, as calculated using equation 2.2, for geometric mean of fluorescence. All data analysis was performed using custom Python scripts.

References

(1) Piraner, D. I.; Farhadi, A.; Davis, H. C.; Wu, D.; Maresca, D.; Szablowski, J. O.; Shapiro, M. G. *Biochemistry* **2017**, *56*, Publisher: American Chemical Society, 5202–5209.

(2) Piraner, D. I.; Abedi, M. H.; Moser, B. A.; Lee-Gosselin, A.; Shapiro, M. G. *Nature Chemical Biology* **2017**, *13*, 75–80.

(3) Zhao, K.; Liu, M.; Burgess, R. R. *Journal of Biological Chemistry* **2005**, *280*, 17758–17768.

(4) Neupert, J.; Karcher, D.; Bock, R. *Nucleic Acids Research* **2008**, *36*, e124.

(5) Waldminghaus, T.; Kortmann, J.; Gesing, S.; Narberhaus, F. **2008**, *389*, Publisher: De Gruyter Section: Biological Chemistry, 1319–1326.

(6) Kortmann, J.; Sczodrok, S.; Rinnenthal, J.; Schwalbe, H.; Narberhaus, F. *Nucleic Acids Research* **2011**, *39*, 2855–2868.

(7) Sen, S.; Apurva, D.; Satija, R.; Siegal, D.; Murray, R. M. *ACS Synthetic Biology* **2017**, *6*, Publisher: American Chemical Society, 1461–1470.

(8) Hoynes-O'Connor, A.; Hinman, K.; Kirchner, L.; Moon, T. S. *Nucleic Acids Research* **2015**, *43*, 6166–6179.

(9) Zheng, Y.; Meng, F.; Zhu, Z.; Wei, W.; Sun, Z.; Chen, J.; Yu, B.; Lou, C.; Chen, G.-Q. *Nucleic Acids Research* **2019**, *47*, e137.

(10) Giuliodori, A. M.; Di Pietro, F.; Marzi, S.; Masquida, B.; Wagner, R.; Romby, P.; Gualerzi, C. O.; Pon, C. L. *Molecular Cell* **2010**, *37*, 21–33.

(11) Kamp, H. D.; Higgins, D. E. *Molecular Microbiology* **2009**, *74*, 421–435.

(12) Chan, C. T. Y.; Lee, J. W.; Cameron, D. E.; Bashor, C. J.; Collins, J. J. *Nature Chemical Biology* **2016**, *12*, Number: 2 Publisher: Nature Publishing Group, 82–86.

(13) Stirling, F.; Bitzan, L.; O'Keefe, S.; Redfield, E.; Oliver, J. W. K.; Way, J.; Silver, P. A. *Molecular Cell* **2017**, *68*, 686–697.e3.

(14) Rottinghaus, A. G.; Ferreiro, A.; Fishbein, S. R. S.; Dantas, G.; Moon, T. S. *Nature Communications* **2022**, *13*, Number: 1 Publisher: Nature Publishing Group, 672.

(15) Gualerzi, C. O.; Maria Giuliodori, A.; Pon, C. L. *Journal of Molecular Biology* **2003**, *331*, 527–539.

(16) Qing, G.; Ma, L.-C.; Khorchid, A.; Swapna, G. V. T.; Mal, T. K.; Takayama, M. M.; Xia, B.; Phadtare, S.; Ke, H.; Acton, T.; Montelione, G. T.; Ikura, M.; Inouye, M. *Nature Biotechnology* **2004**, *22*, Number: 7 Publisher: Nature Publishing Group, 877–882.

(17) Lieb, M. *Journal of Molecular Biology* **1966**, *16*, 149–163.

(18) Lieb, M. *Molecular and General Genetics MGG* **1981**, *184*, 364–371.

(19) Ptashne, M.; Backman, K.; Humayun, M. Z.; Jeffrey, A.; Maurer, R.; Meyer, B.; Sauer, R. T. *Science* **1976**, Publisher: American Association for the Advancement of Science, DOI: 10.1126/science.959843.

(20) Ptashne, M.; Jeffrey, A.; Johnson, A. D.; Maurer, R.; Meyer, B. J.; Pabo, C. O.; Roberts, T. M.; Sauer, R. T. *Cell* **1980**, *19*, 1–11.

(21) Elvin, C. M.; Thompson, P. R.; Argall, M. E.; Hendry, P.; Stamford, N. P. J.; Lilley, P. E.; Dixon, N. E. *Gene* **1990**, *87*, 1230125.

(22) Jechlinger, W.; Glocker, J.; Haidinger, W.; Matis, A.; Szostak, M. P.; Lubitz, W. *Journal of Biotechnology* **2005**, *116*, 11–20.

(23) Part:BBa_I12007, Registry of Standard Biological Parts http://parts.igem.org/Part:BBa_I12007.

(24) Koblan, K. S.; Ackers, G. K. *Biochemistry* **1992**, *31*, 57–65.

(25) Hershberger, P.; Mita, B.; Tripatara, A.; deHaseth, P. *Journal of Biological Chemistry* **1993**, *268*, 8943–8948.

(26) Ai, H.-w.; Olenych, S. G.; Wong, P.; Davidson, M. W.; Campbell, R. E. *BMC Biology* **2008**, *6*, 13.

(27) McGinness, K. E.; Baker, T. A.; Sauer, R. T. *Molecular Cell* **2006**, *22*, 701–707.

(28) Moore, S. J.; Lai, H.-E.; Kelwick, R. J. R.; Chee, S. M.; Bell, D. J.; Polizzi, K. M.; Freemont, P. S. *ACS Synthetic Biology* **2016**, *5*, 1059–1069.

(29) Chen, Y.-J.; Liu, P.; Nielsen, A. A. K.; Brophy, J. A. N.; Clancy, K.; Peterson, T.; Voigt, C. A. *Nature Methods* **2013**, *10*, Number: 7 Publisher: Nature Publishing Group, 659–664.

(30) Der, B. S.; Glassey, E.; Bartley, B. A.; Enghuus, C.; Goodman, D. B.; Gordon, D. B.; Voigt, C. A.; Gorochowski, T. E. *ACS Synthetic Biology* **2017**, *6*, Publisher: American Chemical Society, 1115–1119.

(31) Teague, B. Cytoflow https://github.com/cytoflow/cytoflow/ (accessed 04/25/2022).

(32) Habib, E. A. E. *International Journal of Research and Reviews in Applied Sciences* **2012**, *11*, 14.

(33) Parks, D. R.; Roederer, M.; Moore, W. A. *Cytometry Part A* **2006**, *69A*, 541–551.

(34) Moore, W. A.; Parks, D. R. *Cytometry Part A* **2012**, *81A*, 273–277.

(35) Teague, B. HOWTO: Use the logicle scale in other matplotlib plots Revision 70c0df59., https://cytoflow.readthedocs.io/en/stable/dev_manual/howto/logicle.html (accessed 04/21/2022).

(36) Schneider, C. A.; Rasband, W. S.; Eliceiri, K. W. *Nature Methods* **2012**, *9*, Number: 7 Publisher: Nature Publishing Group, 671–675.

Chapter 3

MULTIPLE COMPONENT INVERSION OF HEAT-ACTIVATED GENE INDUCTION

3.1 Introduction

Previously, two families of orthogonal tunable thermal bioswitches, based on λ repressor (termed TcI mutants) and TlpA, a repressor found on a virulence plasmid of *Salmonella typhimurium*, were engineered [1]. These repressors are heat-labile; i.e. they function as repressors below a certain temperature threshold, which, when exceeded, inactivates them. Thus, above the threshold, transcription commences. However, to extend the application space for temperature-responsiveness, we seek to develop mechanisms to drive gene expression below a temperature threshold. In the previous chapter, we discussed a mechanism for directly inducing gene expression at low temperature using TcI mutants, temperature-sensitive transcriptional activators based on λ repressor. Here, we will discuss methods to invert the action of temperature-sensitive transcriptional repressors to enable low-temperature gene expression.

3.2 Heat-induced repression of protein of interest

Inversion of the action of one repressor by another has been previously demonstrated [2, 3], including inversion of TcI [4]. We sought to apply this principle to temperature-sensitive repressors to specifically achieve low-temperature induction.

We modified a previously-published band-pass circuit [1] to create a state switch circuit for expression of mCherry (RFP) below 36°C and expression of mWasabi (GFP) above 36°C. TlpA36, a mutant of TlpA evolved in the Shapiro lab [1], gates the expression of GFP and of CI, which in turn gates the expression of RFP (Figure 3.1).

We tested the behavior of the circuit using a liquid culture temperature gradient assay (Figure 3.2). Preincubating the cultures to OD_{600} = 0.3 at 30°C revealed that expression levels of RFP and GFP did switch at 36°C, though RFP remained high at T > 36°C (Figure 3.3a). However, pre-incubating at 38°C showed that no new RFP is expressed at T > 36°C, and that the high level of red fluorescence at high temperature after preincubating at 30°C was due to protein produced during the pre-incubation

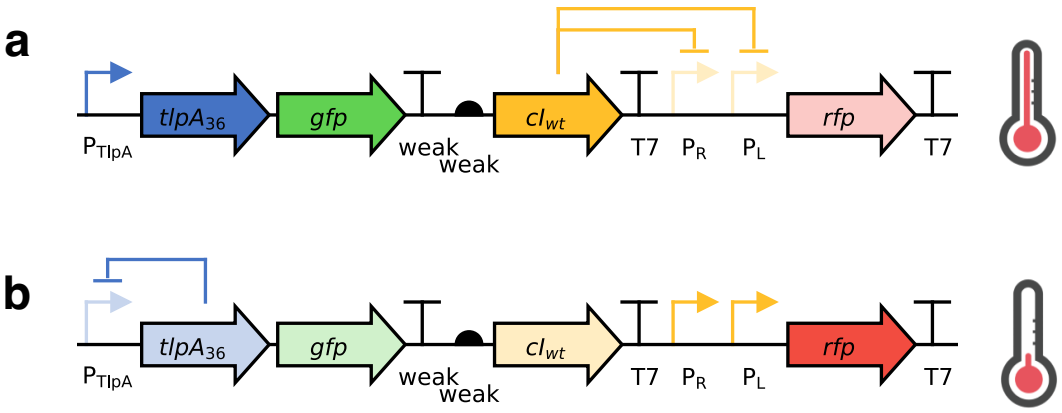

Figure 3.1: Circuit diagram of temperature switch construct for low-temperature RFP and high-temperature GFP, with state of regulation arcs indicated at high (a) and low temperature (b).

phase (Figure 3.3b). The red fluorescence level below 36°C was reduced and the green fluorescence increased after preincubating at 38°C because CI and GFP were produced during preincubation. The CI that was expressed continued to repress expression of RFP even after the sample was transferred to low temperature. The kinetics of switching between low and high temperature states could be improved by the addition of degradation tags to RFP, GFP, and CI.

While the TlpA36-based state switch circuit is in principle modular, we found that replacing CI with other repressors was not trivial (Figure 3.4). We created two additional constructs. In the first, TetR substituted for CI and promoter $P_{LtetO-1}$, which contains a Tet operator, substituted for P_R-P_L. In the second, we used LacI and promoter $P_{LlacO-1}$, which contains a Lac operator. For both of these constructs, RFP no longer exhibited high expression below 36°C, nor did it switch off above 36°C. For the LacI/$P_{LlacO-1}$ construct, we observed low RFP expression at low temperature, and a slight increase with temperature above 36°C, while for the TetR/$P_{LtetO-1}$ construct, no RFP was expressed. However, for both constructs, GFP expression did switch on at high temperature.

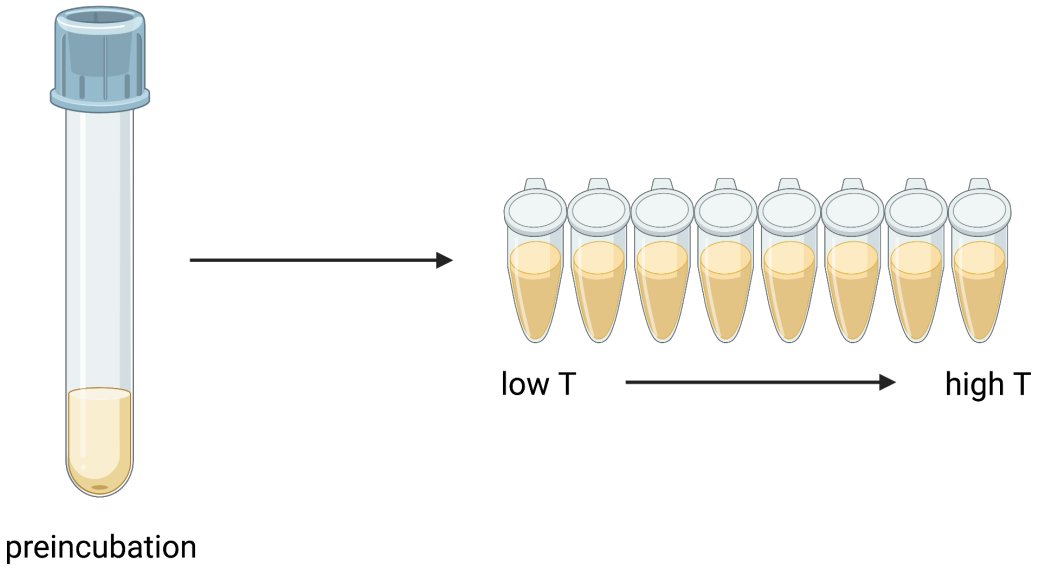

Figure 3.2: Liquid culture temperature response assay. Colonies are inoculated into liquid medium and grown to saturation overnight. Then, the saturated cultures are diluted into fresh medium and preincubated to grow to OD600 = 0.3, log phase. Finally, the cultures are split into PCR tubes and incubated in a temperature gradient for 12 hours, after which fluorescence and OD600 measurements are taken. Figure created with BioRender.com.

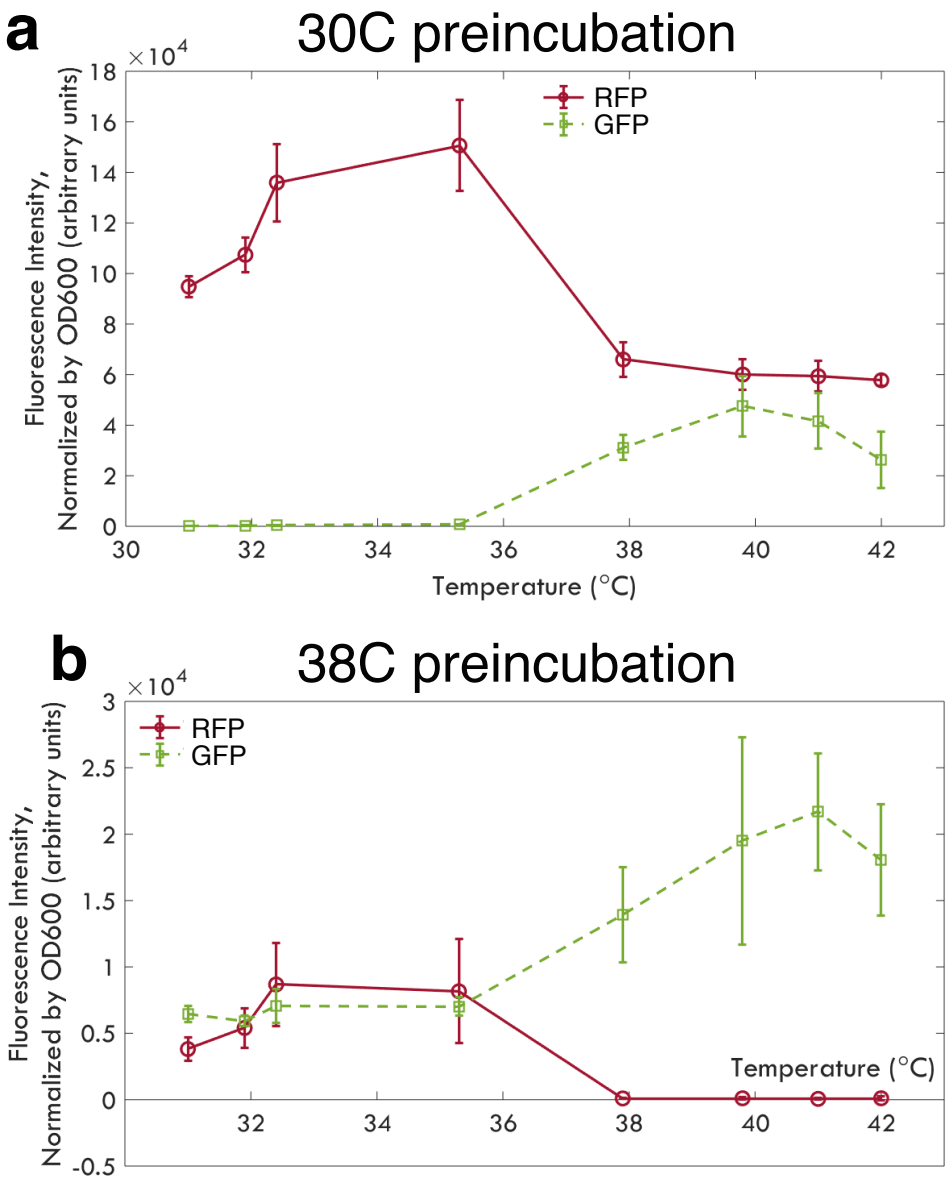

Figure 3.3: TlpA36-based state circuit switches between RFP and GFP expression below and above 36°C, albeit with memory of preincubation temperature. (a) RFP and GFP expression levels with preincubation at 30°C. (b) RFP and GFP expression levels with preincubation at 38°C. n = 4 biological replicates; error bars represent S. E. M.

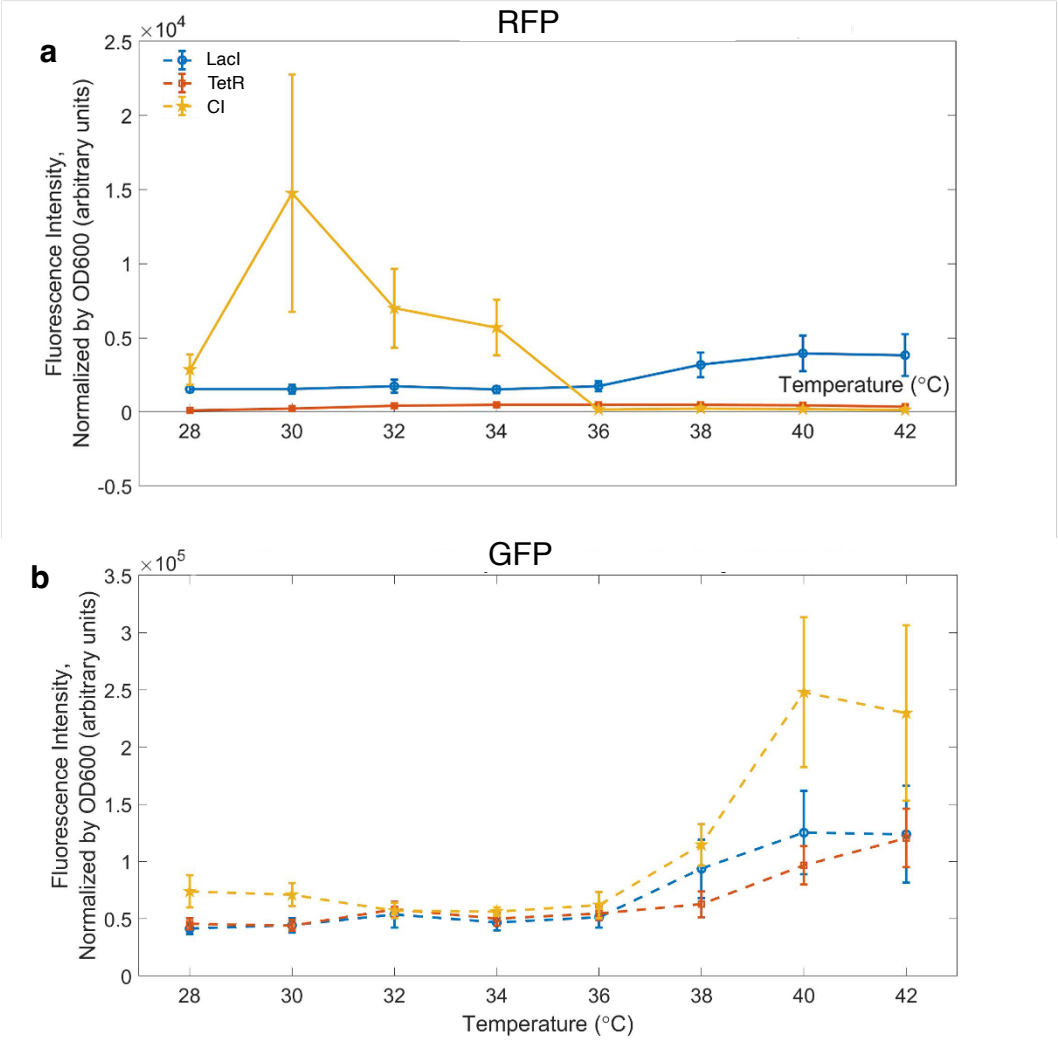

Figure 3.4: RFP (a) and GFP (b) expression levels for TlpA36-based state switch circuit with CI/P_R-P_L; TetR/$P_{LtetO-1}$; and LacI/$P_{LlacO-1}$. n = 4 biological replicates; error bars represent S. E. M. Data acquired with Michael Garrett.

3.3 Heat-induced degradation of protein of interest

As an alternative to turning on expression of a transcriptional repressor at high temperature, we explored the possibility of reducing the concentration of a protein of interest by turning on expression of an orthogonal protease and therefore selectively degrading the protein of interest at high temperature. A heterologous protease from *Mesoplasma florum*, mfLon, has been expressed in *E. coli* and shown to be sufficiently orthogonal to native *E. coli* protein degradation systems to serve as a useful tool in synthetic biology [5, 6]. The mfLon protease targets only proteins with a specific degradation tag, mfssrA; the native Lon and ClpXP do not recognize this tag.

We designed a circuit to constitutively express mfssrA-tagged GFP and to turn on expression of mfLon above the switching temperature of TcI, 39°C (TcI-mfLon/GFP-mfssrA) (Figure 3.5). The protease would then degrade the tagged GFP. We transformed a plasmid encoding this circuit into three strains of *E. coli*: NEB Stable, NEB Turbo, and DH10B. We measured the level of GFP, normalized to $OD_{6}00$, as a function of temperature after preincubating at 30°C (Figure 3.6). For comparison, we also assayed *E. coli* of each strain containing a control construct encoding TcI-gated GFP [1]. While almost no GFP is present in NEB Stable cells containing the TcI-mfLon/GFP-mfssrA construct, both NEB Turbo and DH10B display switch-like behavior, although at T > 39°C, a low level of GFP remains detectable.

We attempted to combine heat-induced repression with heat-induced degradation using a circuit to express mfssrA-tagged GFP from the $P_{LtetO-1}$ promoter. Above the switching temperature of TcI, mfLon and TetR are expressed. TetR represses the expression of mfssrA-tagged GFP, and mfLon degrades any that is present (Figure

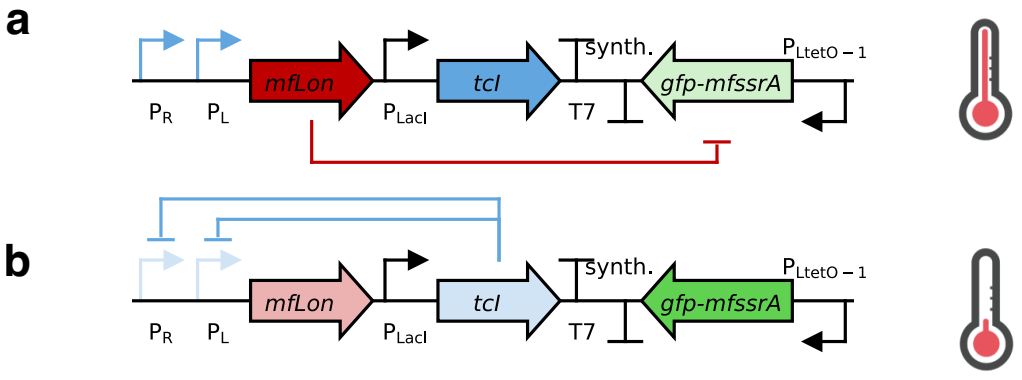

Figure 3.5: Circuit diagram of TcI/mfLon-based switch, with state of regulation arcs indicated at high (a) and low temperature (b).

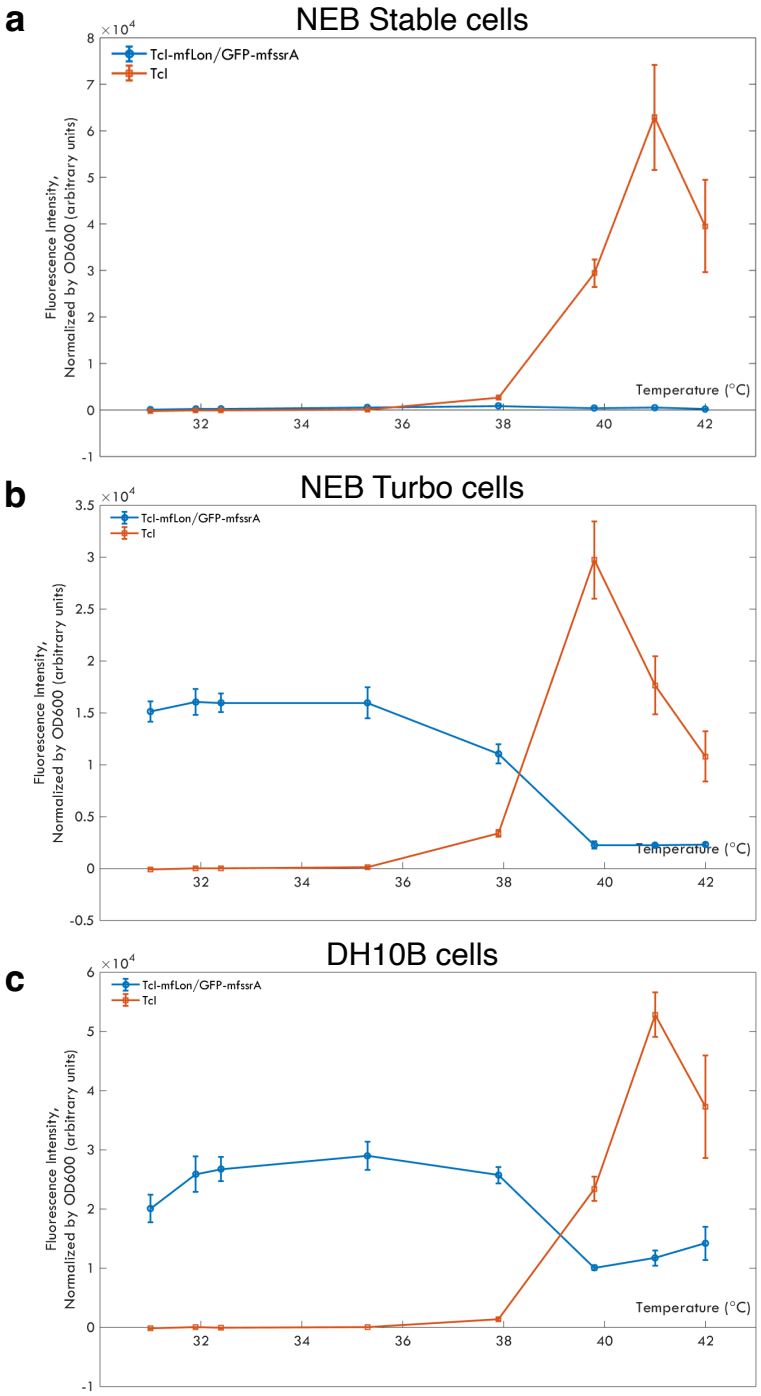

Figure 3.6: GFP levels in NEB Stable (a), NEB Turbo (b), and DH10B (c) *E. coli* containing the TcI/mfLon-based switch at tempertures from 30-42°C. n = 4 biological replicates; error bars represent S. E. M.

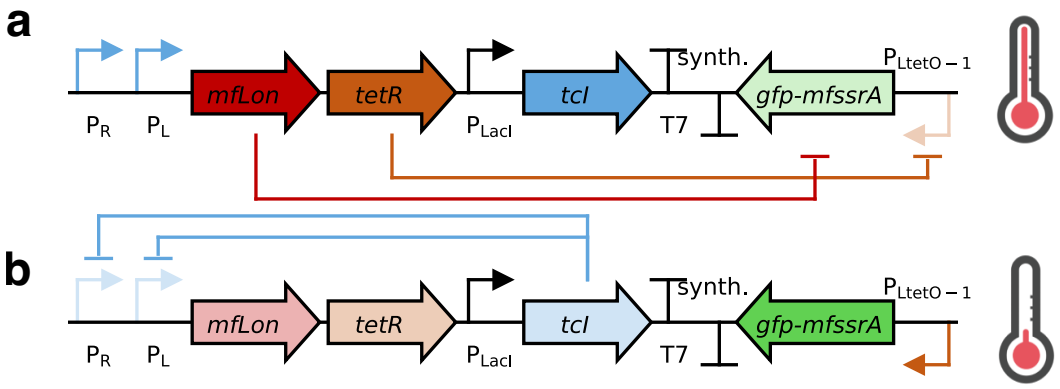

Figure 3.7: Circuit diagram of TcI/mfLon/TetR-based switch, with state of regulation arcs indicated at high (a) and low temperature (b).

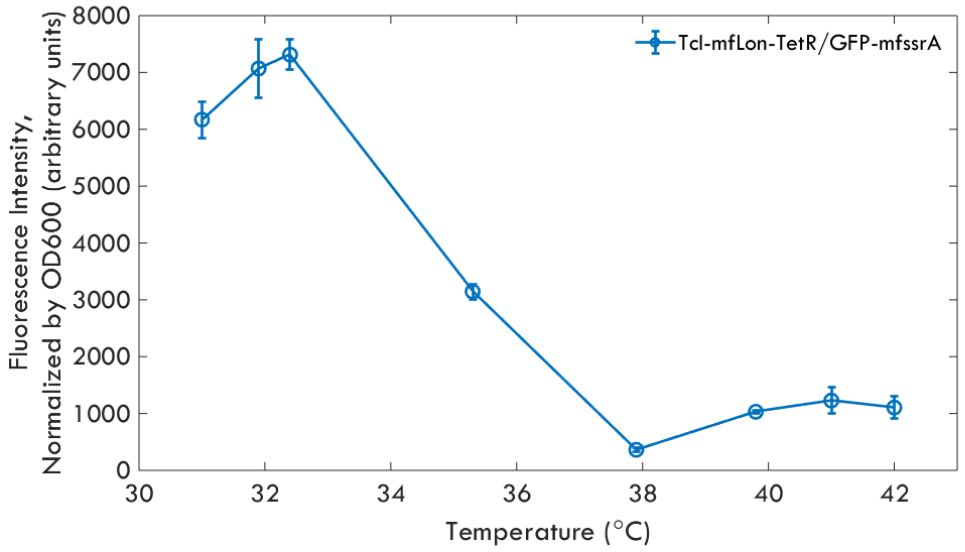

Figure 3.8: GFP levels in NEB Turbo *E. coli* containing the TcI/mfLon/TetR-based switch at tempertures from 30-42°C. $n = 4$ biological replicates; error bars represent S. E. M.

3.7). Based on the behavior of the TcI/mfLon-based switch, we transformed this new TcI/mfLon/TetR-based switch into NEB Turbo *E. coli* and assayed the behavior with temperature (Figure 3.8). Addition of TetR reduces both the "on" and "off" state compared with mfLon alone, even downshifting the switching point slightly and reducing the sharpness of the switch.

3.4 Discussion

We designed and demonstrated several approaches for multi-component low-temperature gene expression. First, we used CI to invert TlpA36, allowing for differential expression of two fluorescent reporters above and below 36°C. In addition, we used TcI to drive the expression of mfLon protease above its switch temperature, 39°C to reduce the concentration of mfssrA-tagged GFP. Finally, we used TcI to drive the expression of both mfLon and TetR aove 39°C to both repress the expression of mfssrA-tagged GFP and to degrade it. The first approach enables the tightest control of protein levels. With preincubation at 38°C, we can express RFP below 36°C and turn off its expression above 36°C. Indeed, the circuit used for a thermal self-regulation application in the next chapter uses the TlpA36/CI-based switch.

3.5 Methods

Plasmid construction and molecular biology

All plasmids were designed using SnapGene (GSL Biotech) and assembled via reagents from New England Biolabs for KLD mutagenesis (E0554S) or HiFi Assembly (E2621L). After assembly, constructs were transformed into NEB Turbo (C2984I) E. coli for growth and plasmid preparation. Thermal gene expression regulation assays were performed in NEB Stable E. coli (C3040I). Integrated DNA Technologies synthesized all PCR primers. Gene circuit diagrams were created using the DNAplotlib [7] library in Python.

Thermal regulation assays

Determination of temperature-dependent gene expression was performed using slight modifications from a previously-described method [1]. 1 mL cultures of 2x YT medium with 100 μg/mL ampicillin were inoculated with a single colony per culture and grown at the specified preincubation temperature with shaking at 250 rpm for 20 h. After dilution to OD600 = 0.1 in LB (Sigma) with 100 μg/mL ampicillin, the cells were propagated at the specified preincubation temperature until reaching OD600 = 0.3 as measured using a Nanodrop 2000c (Thermo Scientific) in cuvette mode. The cultures were dispensed in 25 μL aliquots into 8-well PCR strips with optically transparent caps (Bio-Rad) and incubated for 12 hours in a thermal gradient using a Bio-Rad C1000 Touch thermocycler with the lid set to 50°C. After thermal stimulus, fluorescence was measured using a Stratagene MX3005p qPCR (Agilent). Filter sets used for RFP and GFP were ROX and FAM, respectively. Cultures were immediately diluted with 75 μL LB/amp and mixed, after

which 90 μL was transferred into 96-well plates (Costar black/clear bottom) and OD600 was measured using a SpectraMax M5 plate reader (Molecular Devices). The background-corrected gene expression was determined according to equation 2.2, as described previously [1]. *E. coli* transformed with the pTlpA-wasabi-NF plasmid (obtained from our previous work [1]) served as the background.

3.6 Contributions and acknowledgements

L.L.X. and Mikhail G. Shapiro conceived the study. L.L.X., and Michael A. Garrett planned and performed experiments. L.L.X. analyzed data. M.G.S. and Julia A. Kornfield supervised the research. Thank you to Dan Piraner, Mohamad Abedi, Justin Lee, and Michael Yao for helpful discussions.

References

(1) Piraner, D. I.; Abedi, M. H.; Moser, B. A.; Lee-Gosselin, A.; Shapiro, M. G. *Nature Chemical Biology* **2017**, *13*, 75–80.

(2) Ptashne, M., *A Genetic Switch: Phage Lambda Revisited*; CSHL Press: 2004; 172 pp.

(3) Weiss, R. Cellular Computation and Communications using Engineered Genetic Regulatory Networks, Ph.D. Thesis, Massachusetts Institute of Technology, 2005.

(4) Gardner, T. S.; Cantor, C. R.; Collins, J. J. *Nature* **2000**, *403*, 339–342.

(5) Huang, D.; Holtz, W. J.; Maharbiz, M. M. *Journal of Biological Engineering* **2012**, *6*, 9.

(6) Cameron, D. E.; Collins, J. J. *Nature Biotechnology* **2014**, *32*, Number: 12 Publisher: Nature Publishing Group, 1276–1281.

(7) Der, B. S.; Glassey, E.; Bartley, B. A.; Enghuus, C.; Goodman, D. B.; Gordon, D. B.; Voigt, C. A.; Gorochowski, T. E. *ACS Synthetic Biology* **2017**, *6*, Publisher: American Chemical Society, 1115–1119.

Chapter 4

ENGINEERING THERMALLY SELF-REGULATING BACTERIA WITH TEMPERATURE-DEPENDENT LIGHT ABSORPTION

Adapted from:

(1) Xiong, L. L.; Garrett, M. A.; Kornfield, J. A.; Shapiro, M. G. In 262nd ACS National Meeting & Exposition, Atlanta, GA, 2021.

4.1 Introduction

The field of engineered living materials (ELMs) aims to confer desirable properties of living cells and naturally-occurring biomaterials to designed materials either by incorporating biological cells into a synthetic material, or through formation of a material by living cells and their synthesized biopolymers [1–3]. These properties include self-assembly, self-healing, and sensing & responding to signals. Microbial cells including yeast [4], cyanobacteria [5] and *Bacillus subtilis* [6, 7] have been used in ELMs, but *Escherichia coli* has been an especially common focus of ELM researchers [2, 8–10] because of its extensive characterization and tractability for genetic engineering [11].

While *E. coli* is a laboratory workhorse, it normally lives in the intestines of warm-blooded animals, where the host maintains a stable temperature of about 37°C [12, 13]. However, outside of the laboratory or intestinal environment, cells are exposed to fluctuations in temperature, nutrients, and moisture, all of which affect their viability and growth rate. Indeed, *E. coli* is known to live in freshwater and soil (absent contamination from fecal sources) only in tropical ecosystems, which maintain an appropriate temperature, nutrient level, and humidity [12]. In the laboratory, the minimum temperature for growth of *E. coli* is about 7.5°C in minimal media [14], but even a decrease in temperature from 37°C to 25°C reduces the rate of growth of *E. coli* cultures in exponential phase by about 38% [15]. The reduction in growth rate with temperature correlates with reduced ability to synthesize protein. On the other hand, exposure to temperature above 37°C is also harmful to *E. coli*, with growth inhibited above about 44°C, due to protein instability at high temperatures [16]. Thus, exposure to nonideal temperature limits

the potential for environmental or building materials applications for an ELM in which *E. coli* is a living component.

In this chapter, we develop a genetic circuit that senses temperature and turns on the formation of a light-absorptive pigment below 36°C. We demonstrate that this circuit enables *E. coli* growing in dense patches under simulated sunlight to improve its growth rate over unpigmented *E. coli* at a suboptimal environmental temperature of 32°C by capturing light and warming up. At the same time, when growing at 42°C, an above-optimal temperature, our engineered *E. coli* remains unpigmented and grows faster than bacteria with temperature-independent pigmentation.

4.2 Results

Design of a gene circuit for pigment expression in ELM-like conditions below 36°C

E. coli within ELMs in outdoor applications, such as building exteriors, will be exposed to changes in ambient temperature, which will challenge their ability to grow and produce proteins of interest. For *E. coli*, the optimal growth temperature is 37°C. We propose that when the ambient temperature drops below the optimum, the cells should express a light-absorptive pigment, allowing them to warm up when exposed to sunlight, whereas at or above the optimum, they should remain unpigmented, to avoid overheating (Figure 4.1).

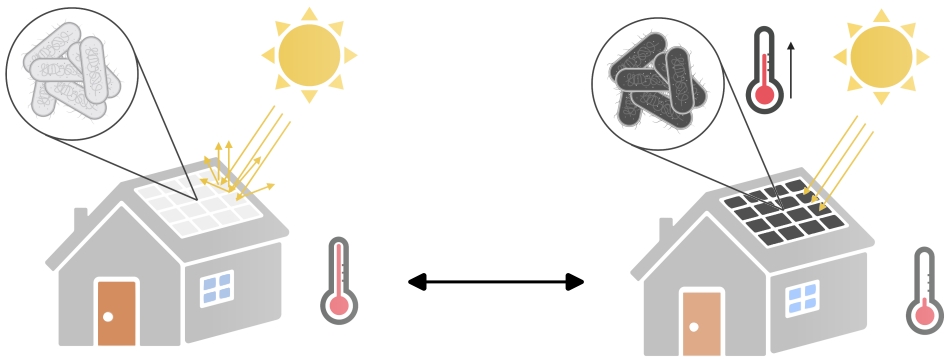

Figure 4.1: Illustration of ELM used as building material. At ambient temperature greater than or equal to optimum for growth, E. coli remain colorless. However, at ambient temperature less than optimal, E. coli express light-absorptive pigment, warming under illumination by the sun to recover growth rate. Illustration created with BioRender.com.

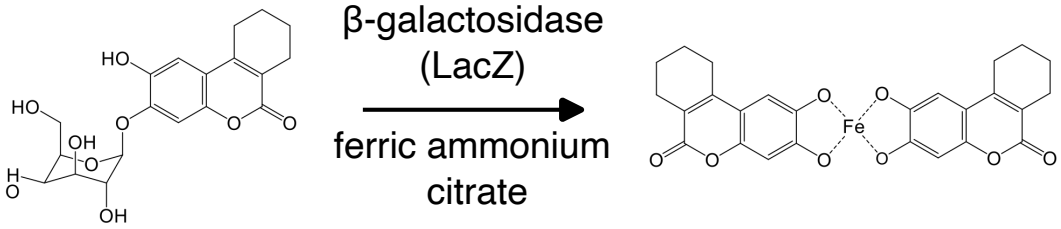

Figure 4.2: Genetically-encodable light-absorptive pigment system. β-galactosidase cleaves S-gal at the glycosidic bond, exposing the esculetin group, which coordinates with ferric iron to form a black pigment.

We repurposed a chemical compound designed to enable the use of β-galactosidase as a gene reporter, 3,4-cyclohexenoesculetin-β-D-galactopyranoside (S-gal), as our genetically-encodable pigment (Figure 4.2). S-gal, which is yellow in solution, consists of galactose linked to 3,4-cyclohexenoesculetin by a glycosidic bond. β-galactosidase hydrolyzes this bond, which frees the esculetin group to complex with ferric iron (provided in the growth medium as ferric ammonium citrate, which is brown in solution) to form a black light-absorptive pigment [17].

We used the TlpA36 transcriptional repressor as a genetically-encodable sensor with a temperature threshold of 36°C [18] and constructed a gene circuit to invert its action, enabling *E. coli* to turn on enzymatic pigment production below 36°C (Figure 4.3). At these temperatures, TlpA36 represses expression of CI repressor from the P_{TlpA} promoter. The LacZα peptide of β-galactosidase, which presents a much lower metabolic burden to the cell than the complete enzyme, is expressed from the P_R-P_L tandem promoter. Above 36°C, TlpA36 loses function, so CI repressor is expressed from the P_{TlpA} promoter and represses expression of LacZα. The complementary LacZω peptide is induced from the genome of *E. coli* DH10B by addition of isopropyl β-D-1-thiogalactopyranoside (IPTG) to the growth medium. mWasabi (GFP) serves as a marker of high temperature.

We measured the visible light absorbance of *E. coli* DH10B containing our temperature switch construct after growth in pigment induction media (containing S-gal, ferric ammonium citrate, and IPTG) at temperatures ranging from 43.7°C to 32.3°C (Figure 4.4). Cultures of *E. coli* containing the temperature switch construct increase in absorbance across the visible light spectrum from 400 – 700 nm below 35.9°C, compared to at and above 35.9°C.

After constructing the temperature switch for expression of pigment below 36°C and demonstrating its function in liquid culture, we grew *E. coli* containing the construct

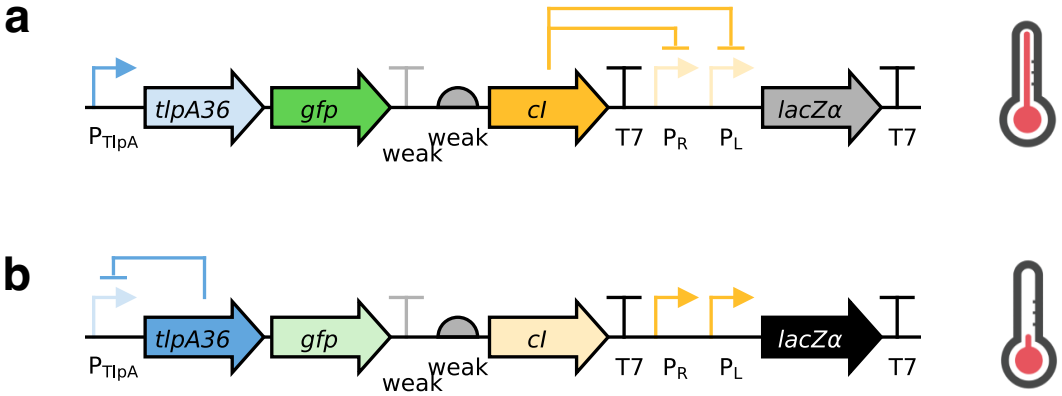

Figure 4.3: Circuit diagram of temperature switch construct for low-temperature pigmentation, with state of regulation arcs indicated at high (a) and low temperature (b).

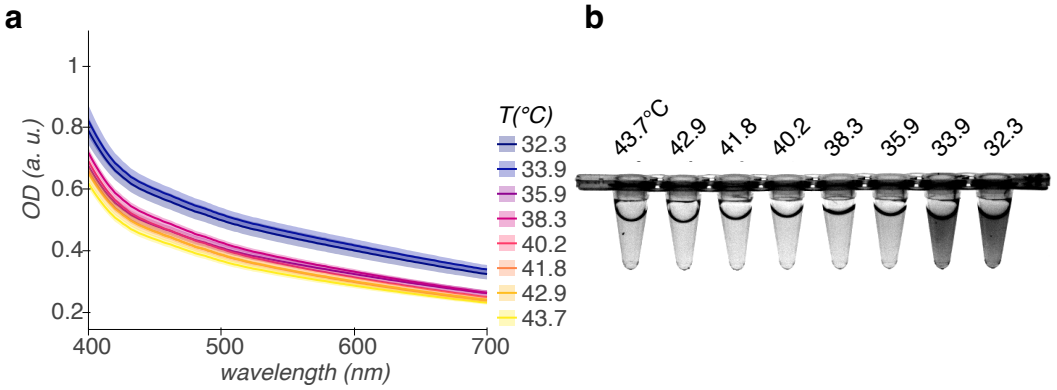

Figure 4.4: Visible light absorption spectra (a) and representative white light transillumination image (b) of cultures of *E. coli* containing the temperature switch construct after 24 h growth in pigment-induction media at temperatures ranging from 43.7°C to 32.3°C. n = 4 biological replicates; shading represents ± standard error of the mean.

in a dense, centimeter-scale patch format to simulate the environment of an ELM. We suction-coated a suspension of cells grown to saturation overnight at 38°C onto a polycarbonate membrane backing and placed on a media-saturated melamine foam growth substrate (Figure 4.5a). We placed the samples in a home-built illuminated growth chamber and monitored the relative temperature of the samples compared to the melamine foam using a lightweight 32x24 thermal IR sensor array (Figure 4.5b). We placed the sensor array on a motorized arm that retracts when not imaging to avoid casting a shadow. After 48 h growth in illuminated conditions at 42°C, patches of *E. coli* containing the temperature switch construct produce little pigment, whereas at 32°C, they become nearly opaque when imaged with white light transillumination (Figure 4.5c, Supplementary Figure 4.14).

Below 36°C, cold-induced pigment increases the growth of *E. coli* under illumination compared with no pigmentation

We tested the ability of turning on pigmentation using the temperature switch construct to confer protection against slowed growth at 32°C with and without illumination by comparing the growth rate of *E. coli* containing our temperature switch construct against the growth rate of *E. coli* containing a control construct encoding mWasabi under the control of TlpA36 [18] (unpigmented control). While patches containing the temperature switch construct express pigment at this temperature, the control patches have no mechanism for pigment production and remain translucent (Figure 4.6a). Due to the low spatial resolution of the sensor array, the precise temperature of the samples cannot be determined; however, the pigmented patches clearly warm above the background temperature (Figure 4.6b).

We monitored the growth of the patches via their thickness, quantified from optical coherence tomography cross-sectional images, and their area, quantified from white light transillumination images. With illumination, the patches containing the temperature switch construct grow to 2-fold the thickness of patches containing the control construct over the course of 72 h (Figure 4.6c-e), whereas without illumination, the patches grow to the same thickness at each timepoint (Figure 4.6f). At this temperature, the slower rate of evaporation without illumination allows for thicker growth overall than with illumination. In addition, with illumination, the temperature switch allows the patches to grow in area linearly with time, while the rate of increase in area of unpigmented patches slows over time (Figure 4.6g). On the other hand, without illumination, patches containing both constructs grow in area linearly at approximately the same rate (Figure 4.6h). These results suggest

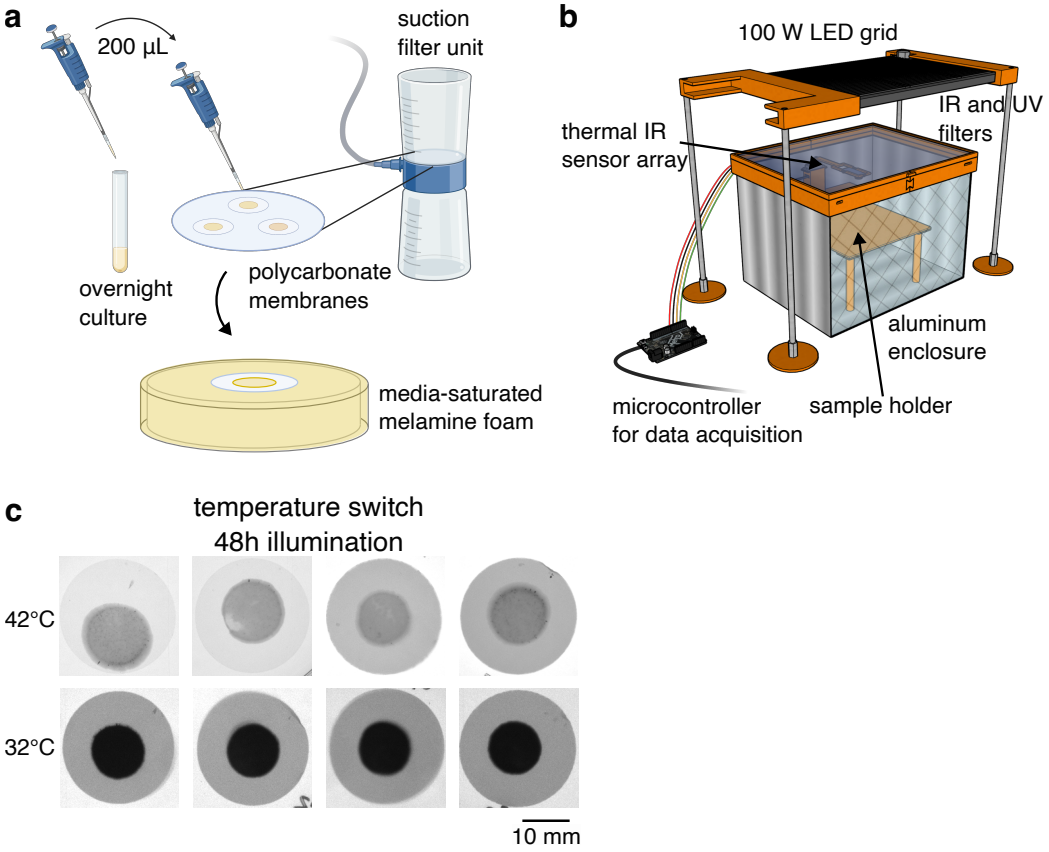

Figure 4.5: Growing *E. coli* in ELM-like conditions. (a) Schematic of formation of dense, centimeter-scale patches of *E. coli* to simulate the ELM environment. We grew *E. coli* overnight to saturation in liquid medium. For each patch, we transferred 200 uL of culture to track-etched polycarbonate membranes (25 mm diam., 0.2 um pores) and applied suction to coat the cells onto the membranes, forming a dense patch. We then transferred the coated membranes to a melamine foam substrate saturated with liquid media for growth. (b) Schematic of illuminated growth chamber. We used a 100W white light LED to expose *E. coli* patches to illumination and monitored the temperature using a 32x24 array of thermal IR sensors. The sensor array is attached to a motorized arm and retracts when not imaging to avoid shadowing the samples. (c) Patches of *E. coli* containing the temperature switch construct on polycarbonate membranes after 48 h growth in the illuminated growth chamber with pigment-induction media at 42°C and 32°C. Parts of figure created with BioRender.com.

that expressing pigment at 32°C using the temperature switch construct gives *E. coli* in a dense patch format a growth advantage under illumination compared with unpigmented patches.

Above 36°C, lack of pigmentation increases the growth of *E. coli* under illumination compared with temperature-independent high pigmentation

While pigmentation is advantageous at suboptimal ambient temperature, we hypothesized that it would be deleterious at above-optimal temperature by exacerbating overheating. To test this hypothesis, we compared the growth at 42°C of patches of *E. coli* containing the temperature switch construct against the growth rate of *E. coli* containing a control construct encoding IPTG-inducible LacZα (pigmented control). After 48 h, the patches containing the temperature switch construct lack pigmentation and appear translucent, while the control patches turn black and opaque and warm above the background temperature (Figure 4.7a,b).

To avoid exposing the samples to laboratory room temperatures ranging from 16 - 25°C during the experiment, we measured the area and thickness of the patches only at the endpoint of 48 h. While the area of the patches containing the temperature switch construct and the patches containing the control construct did not differ significantly (Figure 4.7g,h), the patches containing the control construct were thinner than the patches containing the temperature switch construct in both illuminated and dark conditions (Figure 4.7c-f). However, with illumination, the mean thickness of the temperature switch patches is greater than the mean thickness of the control patches with statistical significance ($p = 0.0006$), whereas without illumination, the significance vanishes ($p = 0.1214$). The smaller difference in thickness without illumination may be due to the burden of protein overexpression from the IPTG-induced control construct. Thus, turning off expression of pigment using the temperature switch construct at 42°C using the temperature switch construct confers an advantage on *E. coli* in a dense patch format grown under illumination compared with chemically-induced pigmentation.

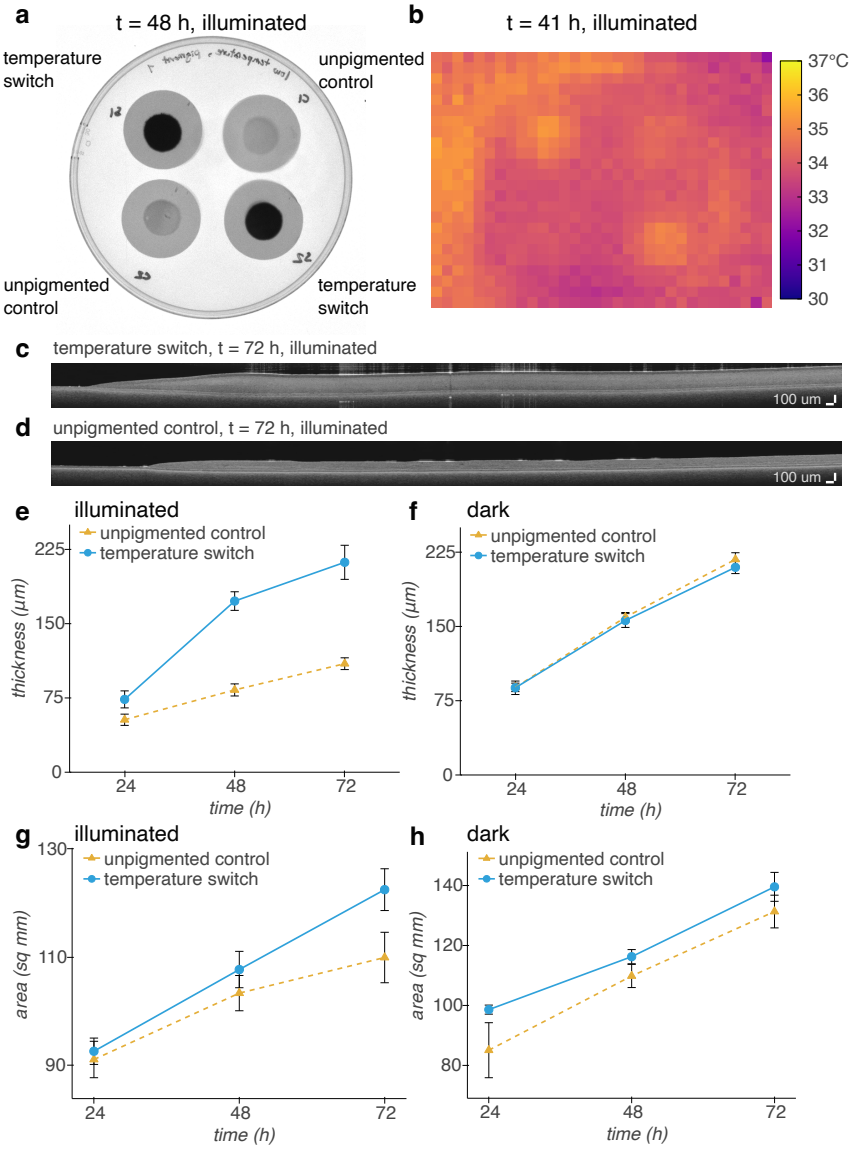

Figure 4.6: Cold-induced pigment improves the growth of dense patches of *E. coli* under illumination at 32°C. (a) White light transillumination image of patches of *E. coli* containing either our temperature switch construct or an unpigmented control construct encoding heat-inducible GFP after transferring to agar for imaging at 48 h. (b) Thermal IR image of patches inside illuminated growth chamber at 41 h. (c, d) Representative OCT images of patches of E. coli containing our temperature switch construct (c) or the unpigmented control construct (d). (e, f) Thickness of patches grown under illumination (e) or in a dark incubator (f) over time. (g, h) Area of patches grown under illumination (g) or in a dark incubator (h) over time. $n = 4$ biological replicates; error bars represent ± standard error of the mean.

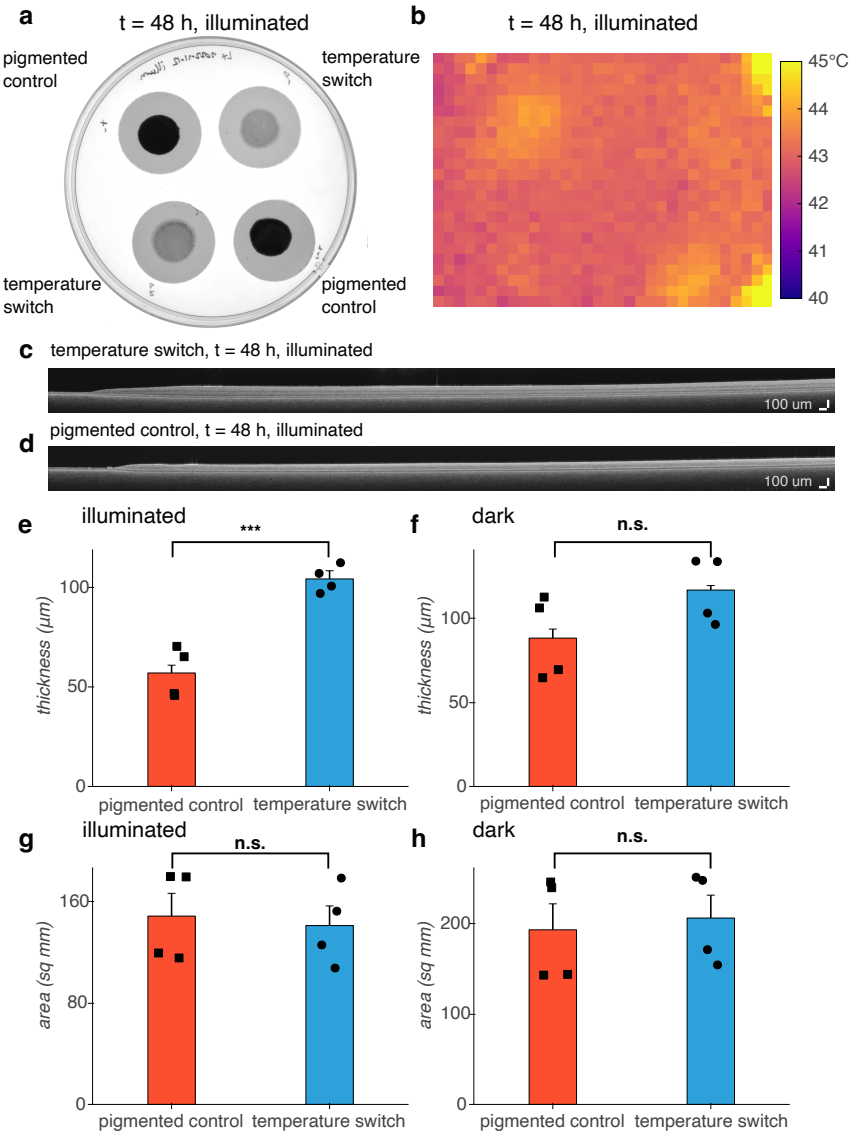

Figure 4.7: Turning off pigmentation above 36°C improves the growth of dense patches of *E. coli* under illumination at 42°C compared to a pigmented control. (a) White light transillumination image of patches of *E. coli* containing either the temperature switch construct or a pigmented control construct encoding IPTG-inducible LacZα after transferring to agar for imaging at 48 h. (b) Thermal IR image of patches inside illuminated growth chamber at 48 h. (c, d) Representative OCT images of patches of E. coli containing our temperature switch construct (c) or the pigmented control construct (d). (e, f) Thickness of patches grown under illumination ($p = 0.0006$) (e) or in a dark incubator ($p = 0.1214$) (f) at 48 h. (g, h) Area of patches grown under illumination ($p = 0.7640$) (g) or in a dark incubator ($p = 0.7456$) (h) at 48 h. $n = 4$ biological replicates; error bars represent ± standard error of the mean. P-values calculated using a two-tailed unpaired t-test.

4.3 Discussion

This work establishes a genetically-encoded mechanism for protection of *E. coli* in an ELM under nonoptimal ambient temperature in outdoor applications. We demonstrated a genetic circuit for expression of a dark, light-absorptive pigment below 36°C. At 32°C, dense patches of *E. coli* containing this circuit become nearly opaque with pigment, allowing them to warm above background and grow in both area and thickness at a greater rate than unpigmented patches. Conversely at 42°C, patches remain translucent, avoiding further overheating and growing to a greater thickness than chemically-induced pigmented patches. Because *E.coli*-based ELMs rely on *E. coli* growth and protein production to form the material, as well as confer engineered properties, such as environmental sensing, to the material, long-term exposure to temperatures below or above 37°C will be detrimental to their function. Our temperature switch genetic construct is in principle compatible with any cloning strain of E. coli with the *lacZ*Δ*M15* genotype, allowing it to be used in existing *E. coli*-based ELMs.

While this study provides a proof of concept for temperature self-regulation, additional work is needed to improve the kinetics of the temperature switch. Because our system does not include a mechanism for degradation of the pigment complex, even brief low-temperature excursions allow pigment to accumulate in the ELM. While protective in the case of long-term exposure to low temperature, this could cause overheating once the ambient temperature reaches 37°C or above. To avoid producing pigment at night in climates or seasons where day-time temperatures exceed 37°C, but night-time temperatures drop below, our circuit could be modified to incorporate a light sensor, such as a phytochrome [19], using an AND gate [20][20], turning on pigment production only with both light and cold temperature. In addition, to hasten the transition from low to high temperature, an enzyme cassette for biodegradation of the esculetin-based pigment could be developed from coumarin degradation pathways found in soil bacteria [21]. This degradation cassette, or a cassette encoding light-scattering proteins such as gas vesicles [22, 23], could be turned on at high temperature in place of the GFP marker currently incorporated in our construct to clear pigment from the ELM or scatter incoming light, increasing protection from heat. With our thermal bioswitch circuits and these future improvements, ELMs will gain the ability to harness sunlight to keep warm or stay cool.

Plasmid	Purpose	Transcriptional Regulator	Output Gene Product(s)
pTSwitch-LacZα	temperature switch	TlpA36, CI	LacZα, mWasabi
pTlpA36-wasabi	unpigmented control	TlpA36	mWasabi
pTrcLacZα	pigmented control	LacIq	LacZα

Table 4.1: Genetic constructs used in this chapter.

4.4 Methods

Plasmid construction and molecular biology

All plasmids were designed using SnapGene (GSL Biotech) and assembled via reagents from New England Biolabs for KLD mutagenesis (E0554S) or HiFi Assembly (E2621L). After assembly, constructs were transformed into NEB Turbo (C2984I) *E. coli* for growth and plasmid preparation. Integrated DNA Technologies synthesized all PCR primers. TlpA36 and mWasabi [24] (GFP) were obtained from our previous work [18]. LacZα was tagged at the C-terminus with the AAV ssrA tag [25] (amino acid sequence AANDENYAAAV). The weak terminator in the temperature switch construct is Part:BBa_B1002 [26]. The weak RBS in the temperature switch construct is RBSF [27]. Plasmids were transformed into DH10B *E. coli* (ThermoFisher) for downstream experiments. Gene circuit diagrams were created using the DNAplotlib [28] library in Python.

Visible light absorbance assays

1 mL cultures of LB medium (Sigma) with 100 μg/mL ampicillin were inoculated with a single colony per culture and grown at 38°C, 250 rpm for 18.5 h. 30 μL were diluted into 2 mL LB with 300 μg/mL 3,4-cyclohexenoesculetin-β-D-galactopyranoside (S-gal) (Sigma), 500 μg/mL ferric ammonium citrate (Sigma), 100 μM IPTG, 100 μg/mL ampicillin and propagated at 38°C, 250 rpm for 90 minutes. The cultures were dispensed in 100 μL aliquots into 8-well PCR strips (Bio-Rad) and incubated for 24 h in a thermal gradient using a DNA Engine Tetrad 2 Peltier Thermal Cycler (Bio-Rad) with the lid set to 50°C. PCR strips were imaged using a ChemiDoc MP Gel Imaging System (Bio-Rad). Contrast was adjusted using ImageJ software [29]. 90 μL were transferred into 96-well plates (Costar black/clear bottom) and absorbance spectra were measured using a Spark multimode microplate reader (Tecan). Data analysis was performed using custom Python scripts.

Preparation of dense patches of *E. coli*

2 mL cultures of LB medium (Sigma) with 100 μg/mL ampicillin (and 25 μM IPTG for pigmented controls) were inoculated with a single colony per culture and grown at 38°C, 250 rpm for 18.5 h. Nalgene Rapid-Flow sterile disposable filter units (cellulose nitrate, 75 mm diameter, 0.2 μm pore size) (ThermoFisher 450-0020) were rinsed with 1x PBS (Corning) and track-etched polycarbonate membranes (25 mm diameter, 0.2 μm pore size) (Sartorius 23007 or Whatman Nuclepore 10417006) were placed on the filter surface. 200 μL bacterial culture was dispensed onto each membrane and vacuum was applied to the filter unit to coat the cells onto the membrane.

Growth of *E. coli* in ELM-like conditions

90 mL (32°C experiments) or 100 mL (42°C experiments) of LB medium (Sigma) with 75 μg/mL S-gal, 125 μg/mL ferric ammonium citrate, 25 μM IPTG, 100 μg/mL ampicillin (and 0.1% D-glucose for 42°C experiments) was added to approximately 0.7 g melamine foam (Amazon) in a petri dish until foam was saturated. For 42°C experiments, saturated foam was prewarmed using a heat lamp. Patches of *E. coli* coated on polycarbonate membranes were placed onto the surface of the saturated foam. Patches were incubated either in a custom illuminated incubator or in a conventional incubator for 72 h (32°C experiments) or 48 h (42°C experiments). At 24 h intervals, petri dishes were weighed to determine the amount of evaporation and the equivalent volume of LB with 75 μg/mL S-gal, 125 μg/mL ferric ammonium citrate, 25 μM IPTG, 100 μg/mL ampicillin (and 0.1% D-glucose for 42°C experiments) at room temperature (for 32°C experiments) or prewarmed to 42°C (for 42°C experiments) was added.

Design and construction of illuminated incubator with *in situ* temperature monitoring

The enclosure of the illuminated incubator is an 8" x 10" x 7.1" aluminum box with a lid consisting of a 1/8" layer of glass (IR-filtering) and a 1.5 mm layer of acrylic (UV-filtering) held in a 3D-printed polylactic acid (PLA) collar. Weatherproofing foam was used to provide a tight fit between the lid and the box. The sample holder is located 120 mm from the 100 W LED grid light source (Mifxion), receiving an average light flux of 120000 lx. The light source is plugged into a power relay (Digital Loggers). The light source heats the interior of the chamber; the temperature is adjusted by adding or removing insulation.

A MLX90640 32 x 24 thermal IR sensor array (Grove or Adafruit) is attached to a SG92R micro servo motor (Tower Pro) via 3D-printed PLA fittings reinforced with wooden craft sticks for monitoring the samples. MCP9808 temperature sensors (Adafruit) were used to monitor the air temperature inside and outside the sample enclosure. All sensors, the servo motor, and the power relay were connected to a Feather M4 Express microcontroller (Adafruit) for data acquisition and control. A custom Bokeh application was used to interface with the microcontroller.

Imaging and analysis of *E. coli* patches

E. coli patches on polycarbonate membranes were transferred from melamine foam growth substrate to 20 mL PBS agar plates for imaging.

White light transillumination imaging was performed using a ChemiDoc MP Gel Imaging System (Bio-Rad). *E. coli* patch area and pixel intensity (normalized to polycarbonate membrane background and opaque black plastic) was measured by using the Canny edge detector algorithm for image segmentation via custom Python scripts.

Optical coherence tomography was performed using a Ganymede 210 Series Spectral Domain OCT Imaging System with an OCTP-900 scanner and 8 μm lateral resolution scan lens (Thorlabs). Cross-sectional images with a 10 mm / 2560 pixel (x) by 1 mm / 491 pixel (z) field of view were acquired at 5.5 kHz A-scan rate with 7 B-scan averages and 5 A-scan averages per acquisition. The despeckle filter in the ThorImageOCT software (Thorlabs) was applied before exporting. *E. coli* patch thickness was measured using a custom Python script. Briefly, after applying a Gaussian filter, the 3 narrowest peaks with height and width fulfilling adjustable thresholds are detected in each column and arranged by distance from the top of the image to correspond with the top of the patch, the top of the polycarbonate membrane, and the bottom of the polycarbonate membrane. The vectors for each interface are Hampel filtered to reduce outliers due to imaging artifacts. The thickness is defined as the distance from the top of the patch to the top of the polycarbonate membrane. The mean thickness and standard deviation of each patch between x = 3.5 mm and x = 9.0 mm (avoiding the edges of the patch) was calculated. Then, the mean for each construct, illumination condition, and temperature was calculated, propagating the standard deviation to calculate the standard error of the mean.

4.5 Contributions and acknowledgements

L.L.X. and Mikhail G. Shapiro conceived the study. L.L.X. and Michael A. Garrett planned and performed experiments. L.L.X. analyzed data. Julia A. Kornfield provided input on research design and data interpretation. L.L.X. and M.G.S. wrote a manuscript for publications with input from all other authors. M.G.S. and J.A.K. supervised the research.

Thank you to Hanwei Liu, David Tirrell, Priya Chittur, and Seunghyun Sim for helpful discussions about engineered living materials, as well as Red Lhota, Robert Learsch, and Justin Bois for assistance with instrument design. This research was supported by the Defense Advanced Research Project Agency (HR0011-17-2-0037 to M.G.S. and J.A.K.), the Institute for Collaborative Biotechnologies (W911NF-19-D-0001 to M.G.S.), the Jacobs Institute for Molecular Engineering (to J.A.K.) and the Elizabeth W. Gilloon Chair (to J.A.K.). L.L.X. was supported by the NSF Graduate Research Fellowship Program. M.A.G. was supported by the NIH MBRS Research Initiative for Scientific Enhancement Program. M.G.S. is an Investigator of the Howard Hughes Medical Institute. Related research in the Shapiro lab is supported by the David and Lucile Packard Foundation and the Dreyfus Foundation.

4.6 Supplementary information

Supplementary figures

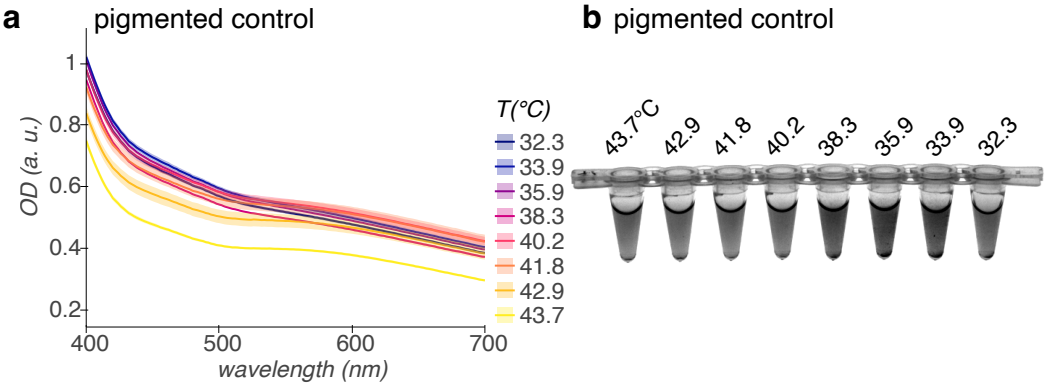

Figure 4.8: Visible light absorption spectra (a) and representative white light transillumination image (b) of cultures of *E. coli* containing a control construct encoding IPTG-inducible LacZα after 24 h growth in pigment-induction media at temperatures ranging from 43.7°C to 32.3°C. $n = 2$ biological replicates; shading represents ± standard error of the mean.

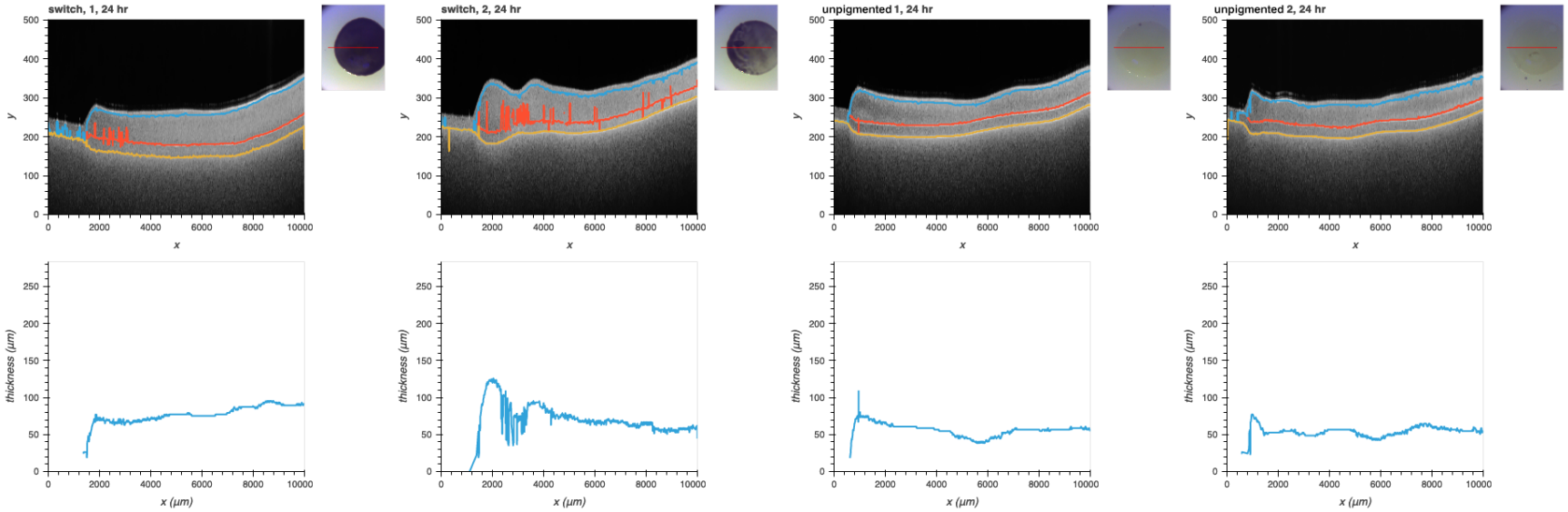

Figure 4.9: Representative OCT images at 24 h for patches of *E. coli* containing either the temperature switch construct or a control construct encoding heat-inducible GFP, grown at 32°C with illumination. Each OCT image is shown with its measured thickness (with Hampel filtering) across the entire field of view. Insets: white light images from the built-in camera of the OCT, showing the imaging path.

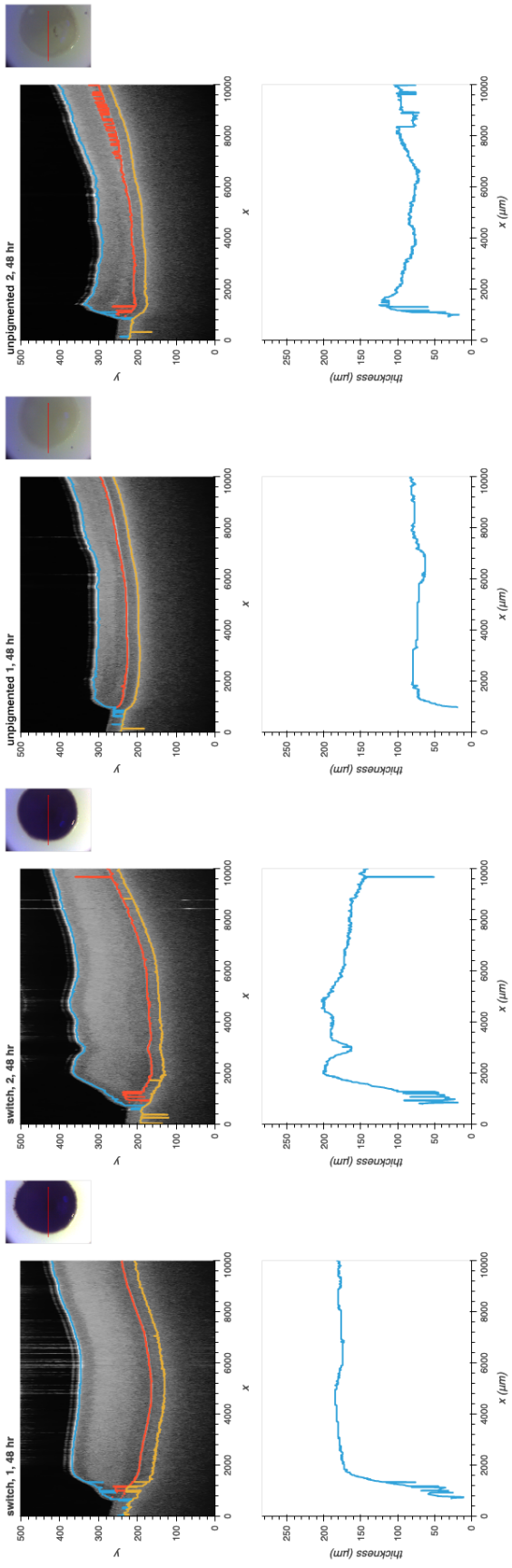

Figure 4.10: Representative OCT images at 48 h for patches of *E. coli* containing either the temperature switch construct or a control construct encoding heat-inducible GFP, grown at 32°C with illumination. Each OCT image is shown with its measured thickness (with Hampel filtering) across the entire field of view. Insets: white light images from the built-in camera of the OCT, showing the imaging path.

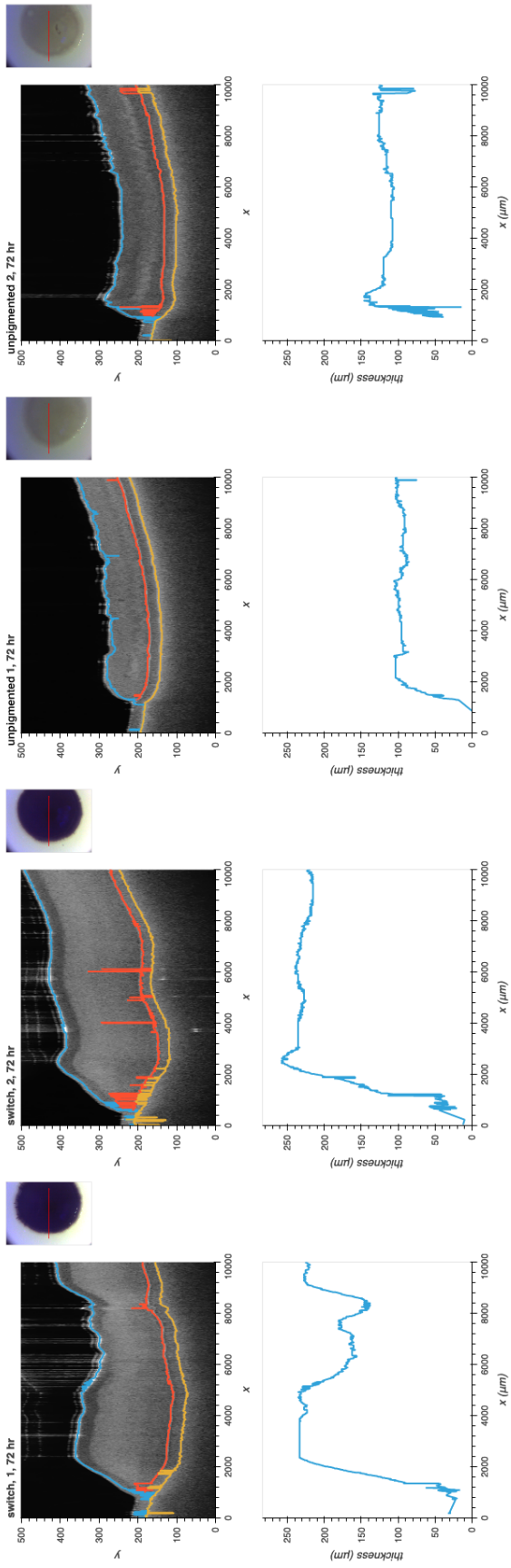

Figure 4.11: Representative OCT images at 72 h for patches of *E. coli* containing either the temperature switch construct or a control construct encoding heat-inducible GFP, grown at 32°C with illumination. Each OCT image is shown with its measured thickness (with Hampel filtering) across the entire field of view. Insets: white light images from the built-in camera of the OCT, showing the imaging path.

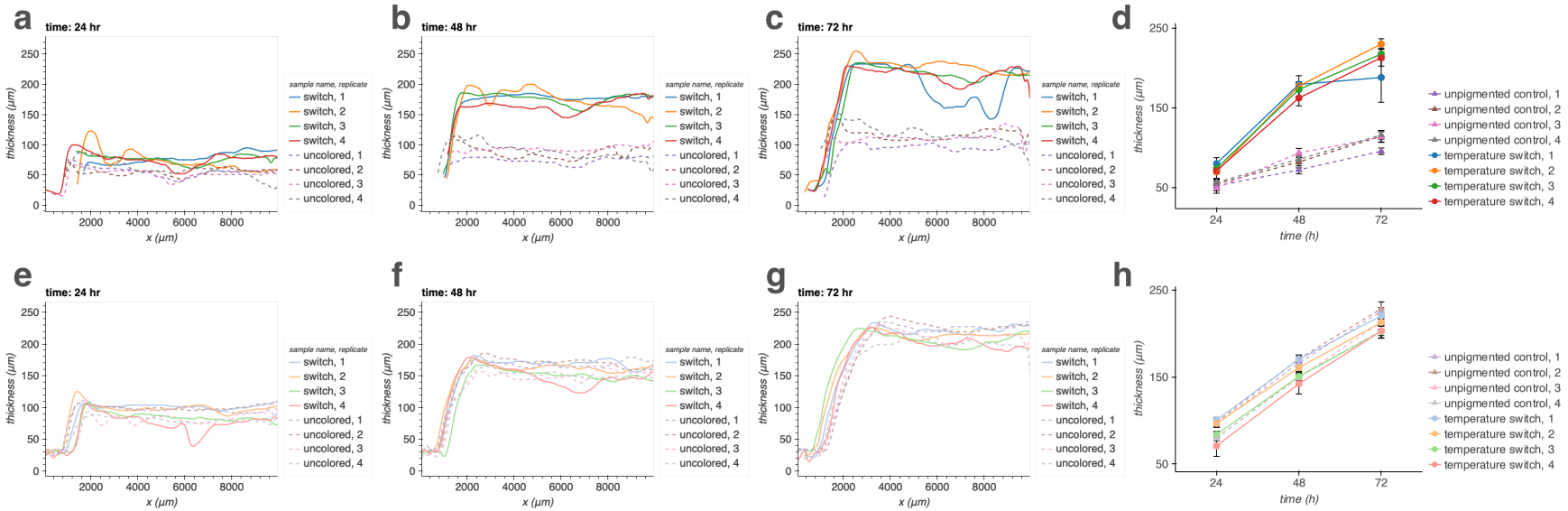

Figure 4.12: Thickness measurements of patches of *E. coli* for each replicate. (a-c) Thicknesses (with Gaussian filtering) measured across full OCT cross-section for each patch of *E. coli* containing either the temperature switch construct or a control construct encoding heat-inducible GFP, grown at 32°C with illumination. (d) Mean thickness and standard deviation between x = 3.5 mm and x = 9.0 mm (avoiding the edges of the patch) of each patch grown at 32°C with illumination. (e-g) Thicknesses across full OCT cross-section for each patch of *E. coli* grown at 32°C without illumination. (h) Mean thickness and standard deviation between x = 3.5 mm and x = 9.0 mm (avoiding the edges of the patch) of each patch grown at 32°C without illumination

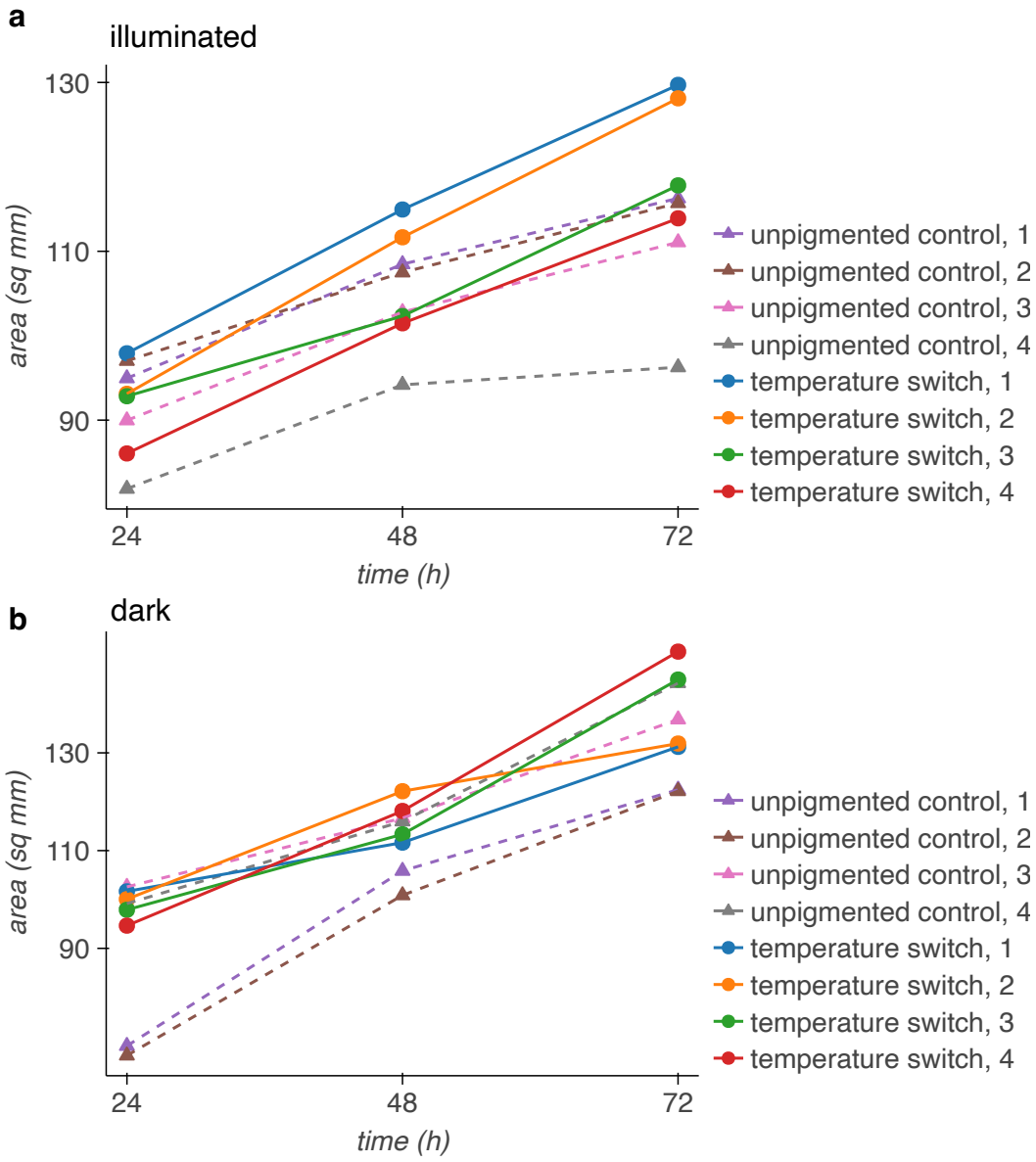

Figure 4.13: Area of patches of *E. coli* containing either the temperature switch construct or a control construct encoding heat-inducible GFP, grown at 32°C with (a) or without (b) illumination over time.

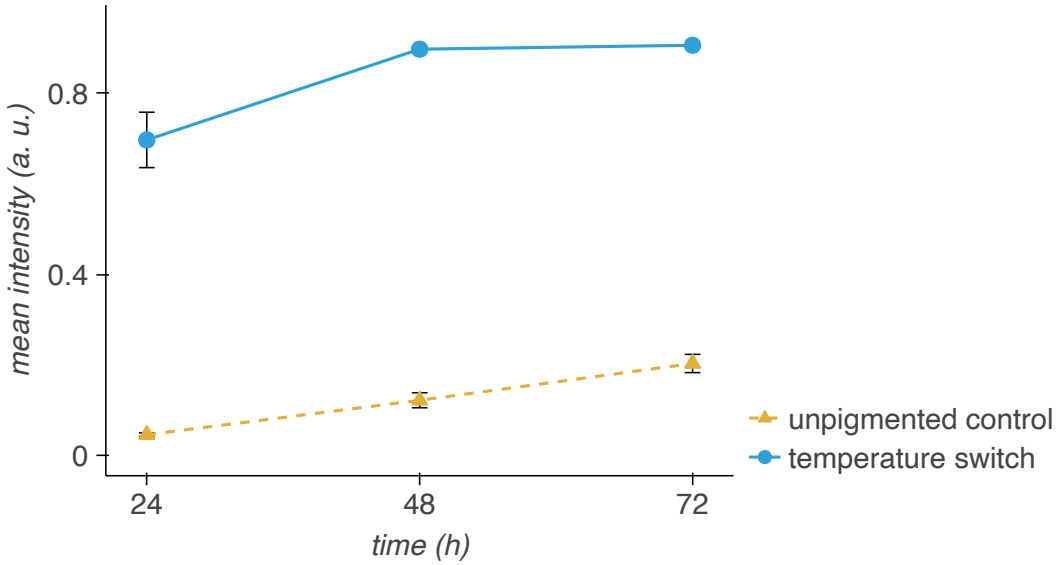

Figure 4.14: Mean pixel intensity of patches of *E. coli* containing either the temperature switch construct or a control construct encoding heat-inducible GFP, grown at 32°C with illumination, over time. Image was normalized so that the polycarbonate membranes have a mean intensity of 0 and opaque black plastic has a mean intensity of 1.

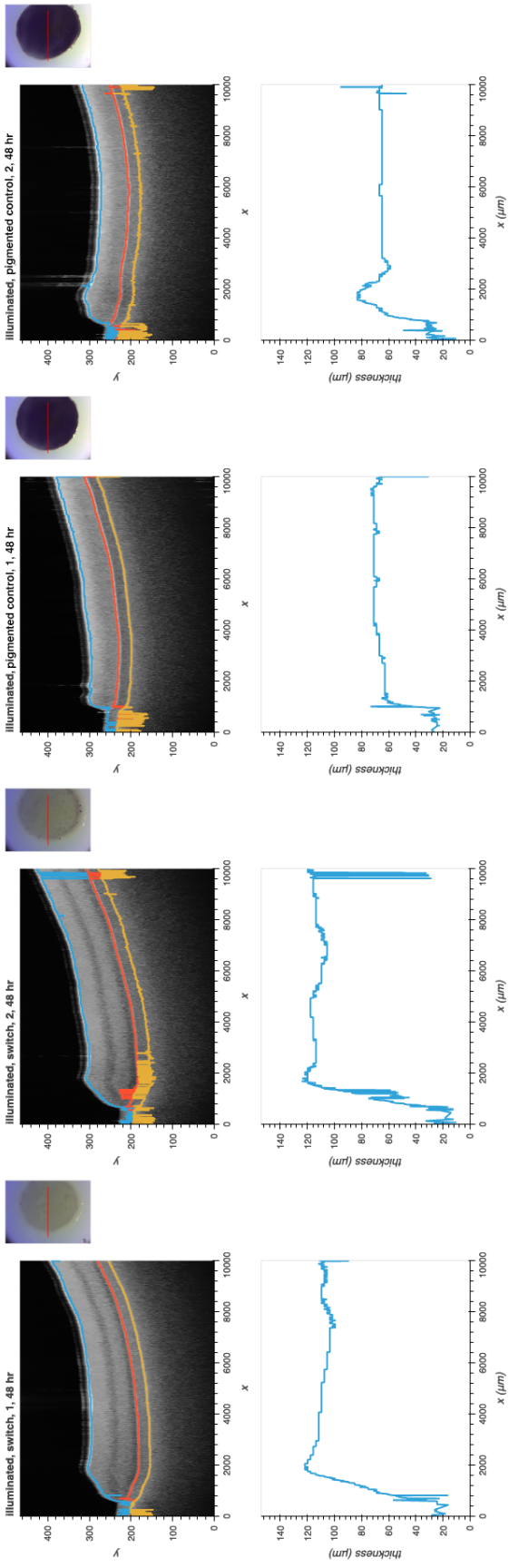

Figure 4.15: Representative OCT images at 48 h for patches of *E. coli* containing either the temperature switch construct or a control construct encoding IPTG-inducible LacZα, grown at 42°C with illumination. Each OCT image is shown with its measured thickness (with Hampel filtering) across the entire field of view. Insets: white light images from the built-in camera of the OCT, showing the imaging path.

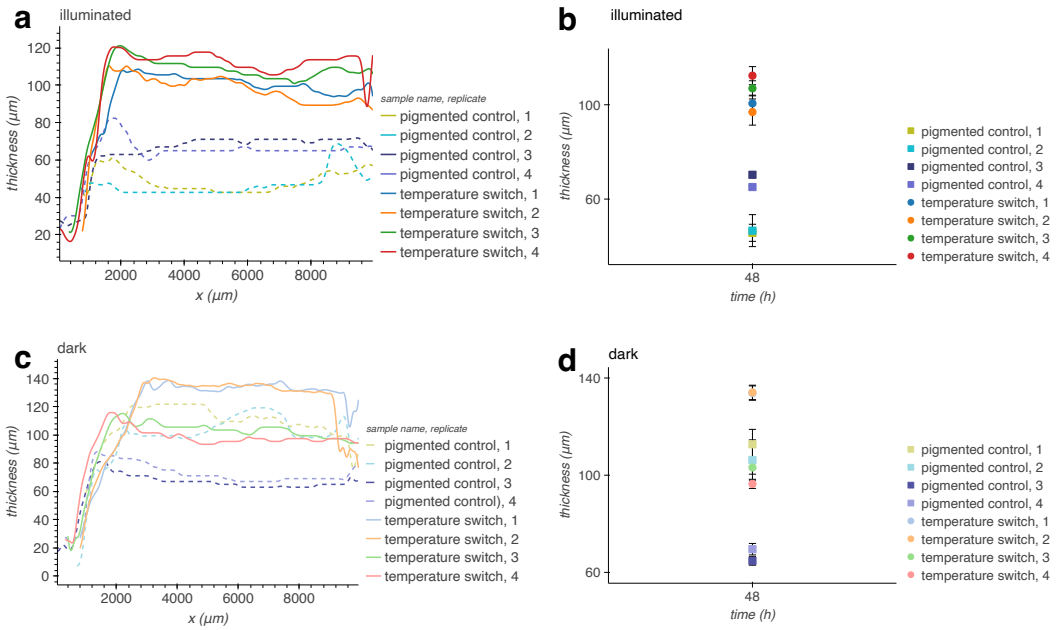

Figure 4.16: Thicknesses (with Gaussian filtering) measured across full OCT cross-section for each patch of *E. coli* containing either the temperature switch construct or a control construct encoding IPTG-inducible LacZα, grown at 42°C with (a) or without (c) illumination for 48 h. (b, d) Mean thickness and standard deviation between x = 3.5 mm and x = 9.0 mm (avoiding the edges of the patch) of each patch, grown with (b) or without (d) illumination over time.

Modeling temperature at the surface of living materials

This section is based in part on guest lecture materials prepared for and presented in Caltech ChE103a (Heat Transfer) in Fall 2021 and Fall 2022.

Here, we explore modeling the temperature at the surface of living materials exposed to sunlight using the heat equation (Equation 4.1).

$$\rho \hat{C}_p \left(\frac{\partial T}{\partial t} + v_r \frac{\partial T}{\partial r} + v_\theta \frac{\partial T}{\partial \theta} + v_z \frac{\partial T}{\partial z}\right) = -\left[\frac{1}{r}\frac{\partial}{\partial r}(r q_r) + \frac{1}{r}\frac{\partial q_\theta}{\partial \theta} + \frac{\partial q_z}{\partial z}\right] + \mathcal{S} \tag{4.1}$$

Components of heat transfer in our system include solar flux into the system, resulting radiative exchange with the surroundings, conduction through our sample through the media system, convection at the surface of the sample, and heat lost to evaporation at the surface of the sample (Figure 4.17).

We assume that our living materials samples and media system are approximately cylindrical; hence, the use of cylindrical coordinates. In this system, we assume that the ELM sample and media system have the thermal properties of water:

$$\begin{cases} k = 0.6 \frac{\mathrm{W}}{\mathrm{mK}} \\ \hat{C}_p = 4.186 \frac{\mathrm{J}}{\mathrm{g\,K}} \\ \rho = 10^6 \frac{\mathrm{g}}{\mathrm{m}^3} \end{cases} \tag{4.2}$$

We assume we are holding the bottom of the media system at a constant temperature, equal to the temperature of the surroundings. The boundary condition at the top of

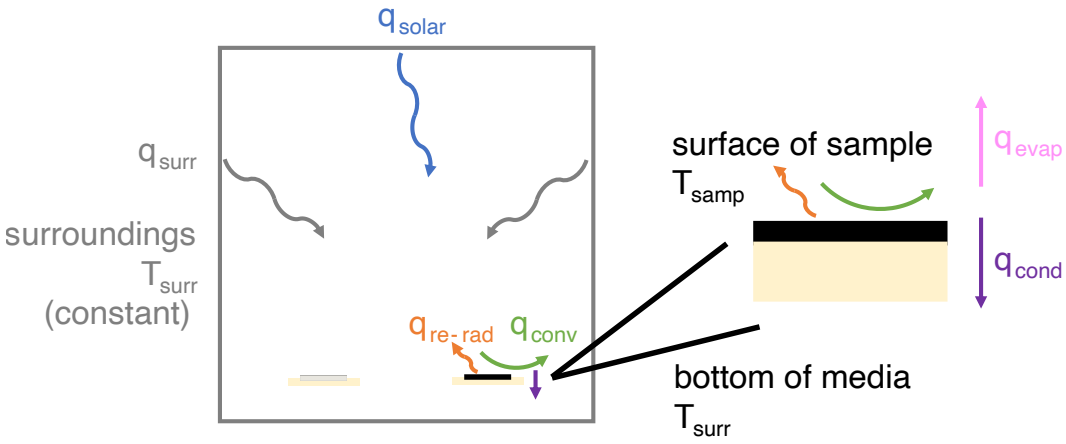

Figure 4.17: Schematic of components of heat transfer for samples exposed to solar illumination.

the sample is a constant radiative flux of 1000 $\frac{\mathrm{W}}{\mathrm{m}^2}$, equivalent to sunlight at midday. The sample has visible light absorptivity $\varepsilon_{\mathrm{vis}}$ and IR light absorptivity $\varepsilon_{\mathrm{IR}}$. Here, $\varepsilon_{\mathrm{vis}}$ depends on pigment production. We assume natural air convection at the surface of the sample.

Should we expect 2D conduction?

To assess whether we should expect 2D conduction, we first write the heat flux density in terms of temperature gradient using Fourier's law (Equation 4.3):

$$\mathbf{q} = -k\nabla T \tag{4.3}$$

$$\begin{cases} q_r = -k\frac{\partial T}{\partial r} \\ q_\theta = -k\frac{1}{r}\frac{\partial T}{\partial \theta} \\ q_z = -k\frac{\partial T}{\partial z}. \end{cases} \tag{4.4}$$

We substitute into the heat equation:

$$\rho\hat{C_p}\frac{\partial T}{\partial t} = \frac{k}{r}\frac{\partial}{\partial r}(r\frac{\partial T}{\partial r}) + k\frac{\partial^2 T}{\partial z^2}. \tag{4.5}$$

Next, we nondimensionalize:

$$\begin{cases} \bar{T} = \frac{T}{\Delta T} \\ \bar{t} = \frac{t}{\tau} \\ \bar{r} = \frac{r}{R} \\ \bar{z} = \frac{z}{L} \end{cases} \tag{4.6}$$

$$\frac{\partial \bar{T}}{\partial \tau} = \frac{\alpha\tau}{R^2}\frac{1}{\bar{r}}(\frac{\partial}{\partial \bar{r}}(\bar{r}\frac{\partial \bar{T}}{\partial \bar{r}})) + \frac{\alpha\tau}{L^2}\frac{\partial^2 \bar{T}}{\partial \bar{z}^2}, \tag{4.7}$$

where $\alpha = \frac{k}{\rho\hat{C_p}}$ is the thermal diffusivity.

The nondimensional number for comparing conduction in z versus r is:

$$\frac{\text{conduction transport rate in } r}{\text{conduction transport rate in } z} = \frac{L^2}{R^2}. \tag{4.8}$$

For patches of bacteria (Figure 4.5a), the radius of the sample is $R \approx 0.5$ cm and the height of the sample and media system is $L \approx 1.5$ cm.

Thus, $\frac{L^2}{R^2} \approx 9$. This is greater than 1, so we may observe temperature gradients in r.

Can we assume a steady state?

For the purposes of this analysis, we neglect conduction in r, because $\frac{L^2}{R^2}$ is relatively close to 1. In addition, we neglect convection and source, and by symmetry, there is no conduction in θ. We are left with the heat equation in 1 dimension:

$$\rho \hat{C_p} \frac{\partial T}{\partial t} = -\frac{\partial q}{\partial z}. \tag{4.9}$$

Using Fourier's law again, we rewrite in terms of T and nondimensionalize:

$$\rho \hat{C_p} \frac{\partial T}{\partial t} = k \frac{\partial^2 T}{\partial z^2} \tag{4.10}$$

$$\frac{\partial \bar{T}}{\partial \bar{t}} = \frac{\alpha \tau}{L^2} \frac{\partial^2 \bar{T}}{\partial \bar{z}^2}. \tag{4.11}$$

Now, we can consider the Fourier number:

$$\text{Fo} = \frac{\text{conduction transport rate in } z}{\text{thermal storage rate}} = \frac{\alpha \tau}{L^2}. \tag{4.12}$$

Once again using the thermal properties of water and $L \approx 1.5$ cm, Fo = 0.02 $\text{s}^{-1}\tau$, where τ is the timescale to reach steady state.

If the rate of heat conduction is comparable to the rate of heat storage, Fo $\approx 1 \implies$ $\tau \approx 2 \times 10^3$s, or 30 minutes. So, on the timescale of growing a living material, days, we can assume steady state.

Finite element analysis of living material temperature

We used COMSOL Multiphysics software to perform finite element analysis of living material temperature at steady state. We implemented a 2D axisymmetric geometry consisting of a sample with R = 5 mm, Z = 0.1 mm centered on a substrate with R = 36.5 mm, Z = 16 mm. All components have the thermal properties of water. The sample's visible light absorptivity depends on its expression of pigment. The

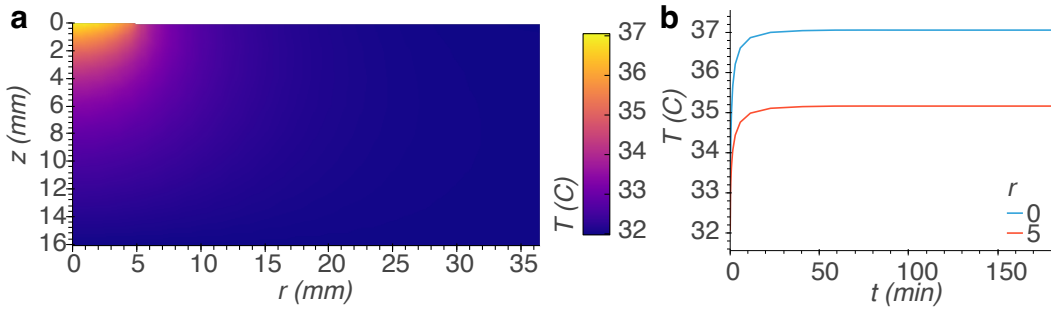

Figure 4.18: Steady state temperature for a sample with $\varepsilon_{\text{vis}} = 0.9$ located in surrounding at 32°C. (a) Temperature map in $\hat{r}$ and $\hat{z}$ of the sample and substrate. The sample is located on top of and centered with the substrate. (b) Temperature over time at the center of the sample ($r = 0$ mm) and edge of the sample ($r = 5$ mm).

substrate has $\varepsilon_{\text{vis}} = 0.1$, or low visible light absorptivity. The sample and substrate have an initial temperature equivalent to the surroundings. Boundary conditions include radiative exchange with the surroundings, constant temperature equivalent to the surroundings at the sides and bottom of the substrate, natural convection with heat transfer coefficient $h = 10$ at the surface of the sample and substrate, constant heat flux into the sample and substrate surface of 1000 $\frac{\text{W}}{\text{m}^2}$ from sunlight, and constant heat flux out of the sample and substrate surface due to evaporation. Empirically, about 25 mL of water evaporates in 24 h from a system with this geometry sitting in a Petri dish with diameter 90 mm, equivalent to 102.8 $\frac{\text{W}}{\text{m}^2}$.

Using this model, for a sample with $\varepsilon_{\text{vis}} = 0.9$, or high visible light absorptivity, located in surroundings at 32°C, we predict that the center of the sample will reach 37°C at steady state, with a 2°C decrease along r to the edge of the sample (Figure 4.18).

We can extend our analysis to a range of temperatures of the surroundings and visible light absorptivities of the sample (Figure 4.19). Our model suggests that with these conditions and with pigment kinetics on the scale of reaching steady state temperature, we should turn on pigment production starting when the temperature drops to 37°C or below. Then, pigment will be formed until the correct visible light absorptivity is achieved to warm to 37°C at the center of the sample. Due to the small area of the samples, up to a few degrees is lost in $\hat{r}$.

While we engineered a genetic circuit to change visible light absorptivity with temperature, radiation is only one component of heat transfer in this system. Our model predicts that by changing the conductivity through adding a layer of insulation

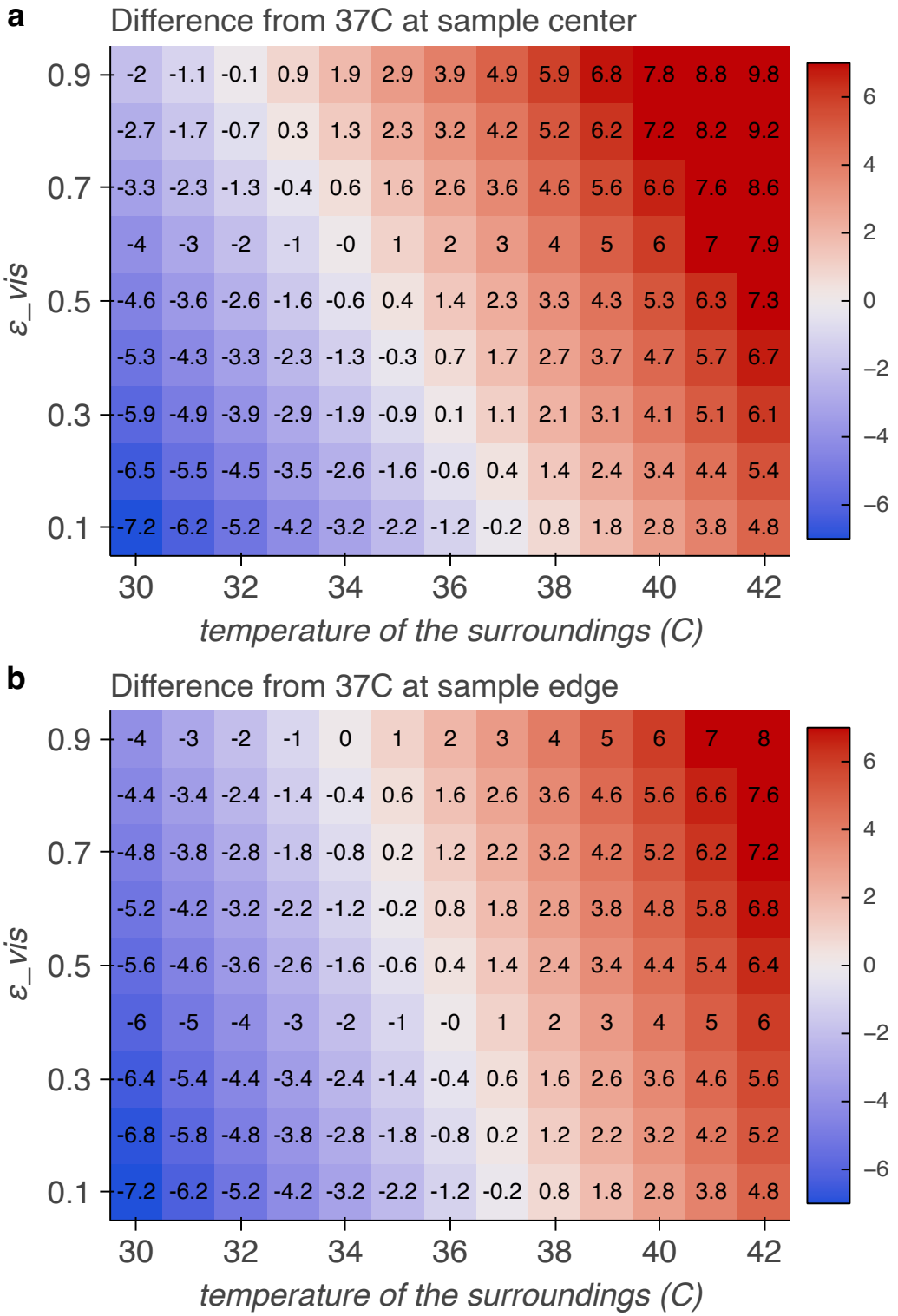

Figure 4.19: Difference from 37°C at center of sample (a) and edge of sample (b) with varying visible light absorptivity and temperature of the surroundings for patches of bacteria growing on liquid medium.

below the substrate, we can extend the lower temperature limit in which our circuit is protective (Figure 4.20).

Now, we implemented a 2D axisymmetric geometry consisting of a sample with R = 15 mm, Z = 0.1 mm centered on a substrate with R = 50 mm, Z = 2.5 mm, which is in turn centered on insulation with R = 150 mm, Z = 25 mm. The sample and substrate have the thermal properties of water, while the insulation has the thermal properties of polyurethane foam. The sample's visible light absorptivity depends on its expression of pigment. The substrate and insulation have $\varepsilon_{\text{vis}} = 0.1$, or low visible light absorptivity. The sample and substrate have an initial temperature equivalent to the surroundings. Boundary conditions include radiative exchange with the surroundings, constant temperature equivalent to the surroundings at the sides and bottom of the substrate, natural convection with heat transfer coefficient $h = 10$ at the surface of the sample and substrate, and constant heat flux into the sample and substrate surface of 1000 $\frac{\text{W}}{\text{m}^2}$ from sunlight.

In this scenario, if the sample turns on pigment production below 30°C, the center of the sample is able to warm to above 37°C in surroundings as low as 4°C!

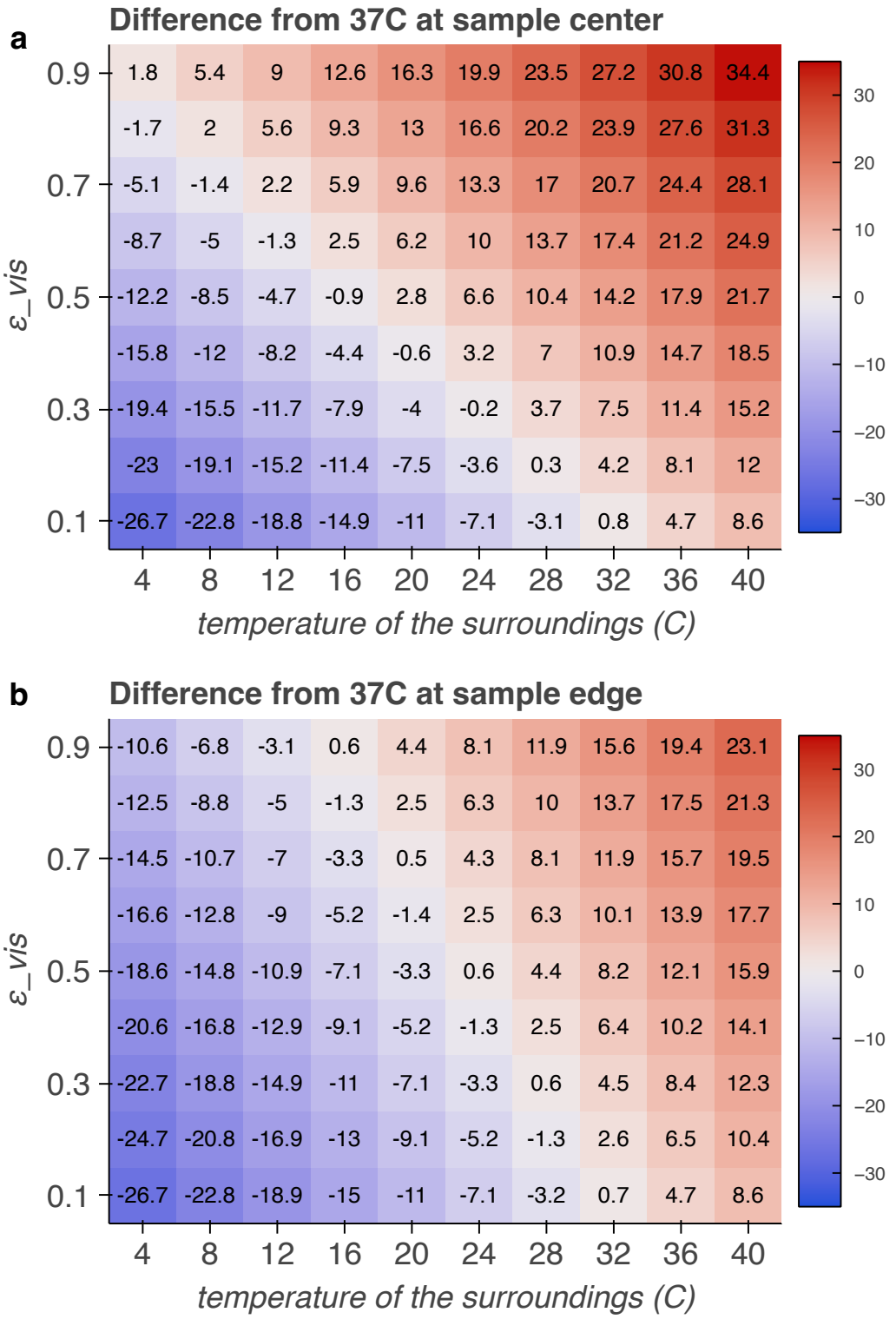

Figure 4.20: Difference from 37°C at center of sample (a) and edge of sample (b) with varying visible light absorptivity and temperature of the surroundings for patches of bacteria growing on liquid medium with insulation underlay.

Investigations into location of pigment formation by *E. coli*

On a macroscopic scale, whether the pigment produced by *E. coli* in an engineered living material localizes within the cells themselves, extracellularly, or both, does not affect the absorption of sunlight at the surface, as long as the pigment is in high enough concentration within the living material. However, where the pigment is produced and where it is transported could affect future strategies to actively degrade pigment to to accelerate the transition from dark to translucent in response to a change in environment from low to high temperature.

The 3,4-cyclohexenoesculetin pigment used in our study is structurally similar to esculetin, which soluble in water at less than 1 mg/mL [30]. The cyclohexene group further decreases the hydrophilicity of the compound. When patches of *E. coli* containing our switch construct are grown at 30°C on melamine foam saturated with pigment-induction media for 24 hours, they become opaque with pigment (Figure 4.21). Transferring the patches to agar shows that the pigment diffuses minimally into the melamine foam substrate.

On the other hand, when a patch of *E. coli* containing our switch construct is grown at 30°C on polyurethane foam saturated with pigment-induction media for 24 hours, nearly all the pigment that it produces diffuses into the polyurethane foam; the patch of *E. coli* appears completely transparent over the majority of the area, with very little pigment coloring the edge. (Figure 4.22). This demonstrates that the pigment is not intracellular. The polyurethane foam (normally used as a sponge for application of cosmetics) swells when it absorbs aqueous solutions, including the bacterial growth

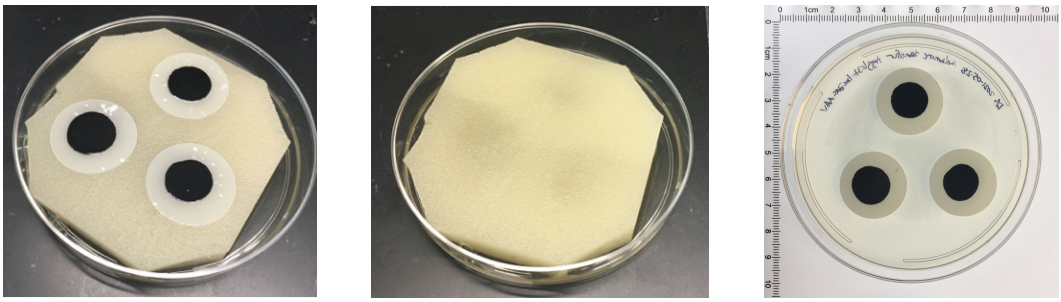

patches of bacteria containing switch circuit
24 h growth on melamine foam, 30°C

melamine foam after removing
patches of bacteria

patches of bacteria
after transferring to LB agar

Figure 4.21: Patches of *E. coli* containing our temperature switch construct become opaque due to the pigment they produce after 24 hours of growth at 30°C on melamine foam saturated with pigment-induction media. Left: patches of *E. coli* as grown on melamine foam substrate. Center: melamine foam after removing patches of *E. coli*. Right: patches of *E. coli* after transferring to LB agar plate.

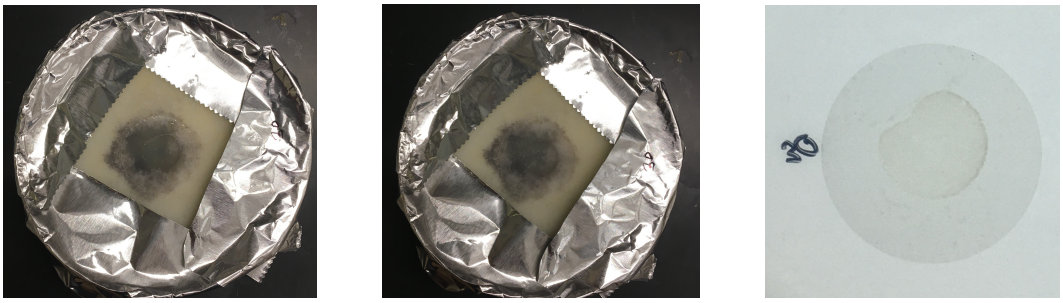

Figure 4.22: A patch of *E. coli* containing our temperature switch construct develops pigment after 24 hours of growth at 30°C on polyurethane foam saturated with pigment-induction media; however, the pigment localizes in the foam substrate, outside of the cells. Left: a patch of *E. coli* as grown on polyurethane foam substrate. Center: polyurethane foam after removing the patch of *E. coli*. Right: the patch of *E. coli* after transferring to LB agar plate.

media. However, the media beads on the surface of the foam when it is initially added to the foam, indicating that the material contains hydrophobic moieties. We hypothesize that the attraction of the 3,4-cyclohexenoesculetin pigment to the surface of the foam increases the rate of diffusion away from the cells.

The conversion of 3,4-cyclohexenoesculetin β-D-galactopyranoside (S-gal) to pigment (Figure 4.2) occurs in two steps. First, S-gal is cleaved to 3,4-cyclohexenoesculetin by β-galactosidase. Then, the 3,4-cyclohexenoesculetin coordinates with ferric iron to form the black pigment. To determine where each step takes place, we cultured *E. coli* DH10B containing a preliminary version of temperature switch construct, a control construct encoding IPTG-inducible LacZ (LacZ overexpression, pigmented control), or a control construct encoding a non-fluorescent mutant of mWasabi under the control of TlpA (no LacZ, unpigmented control) in LB medium with 100 μg/mL ampicillin or LB medium with 300 μg/mL S-gal and 100 μg/mL ampicillin for 23 hours at 30°C, 250 rpm. We passed the saturated cultures through a 0.22 μm filter to remove the cells. Then, to the filtered media from the samples cultured without S-gal, we added S-gal to 300 μg/mL and ferric ammonium citrate to 500 μg/mL; to the filtered media from the samples cultured with S-gal, we added ferric ammonium citrate to 500 μg/mL. After mixing by vortexing, we imaged the media at 3 minutes, 5 minutes, and 45 minutes (Figure 4.23). In addition, we measured the UV-visible light spectrum (Figure 4.24). The preliminary version of the temperature switch construct lacks the ssRA degradation tag on *lacZ*α; the rest of the construct is identical to the temperature switch construct used elsewhere in this chapter.

In the case of growing *E. coli* containing the temperature switch construct without S-gal or ferric ammonium citrate, no pigment developed by 45 minutes after the addition of S-gal and ferric ammonium citrate to the filtered media, as determined by visual comparison with the non-pigmented control and by visible light spectroscopy. However, in the case of growing *E. coli* containing the temperature switch contruct with S-gal but without ferric ammonium citrate, pigment developed by 3 minutes after the addition of ferric ammonium citrate to the filtered media. This implies that the conversion of S-gal to 3,4-cyclohexenoesculetin occurs inside the cell, and the 3,4-cyclohexenoesculetin diffuses or is transported outside of the cell, where it forms the pigment complex with ferric iron.

In the case of growing *E. coli* containing the LacZ overexpression pigmented control construct without S-gal or ferric ammonium citrate, the addition of S-gal and ferric ammonium citrate to the filtered media resulted in the development of pigment by 3 minutes, with an increase in the amount of pigment over time. In the case of growing *E. coli* containing the LacZ overexpression contruct with S-gal but without ferric ammonium citrate, a much large amount of pigment develops by 3 minutes. This implies that S-gal is both converted to 3,4-cyclohexenoesculetin outside the cell and forms the pigment complex with ferric iron outside the cell; however, the conversion of S-gal is slow. The overexpression of LacZ is burdensome to *E. coli*, so we hypothesize that β-galactosidase could be present in the filtered media due to cell lysis after 23 hours in culture. Further experimentation is needed to confirm how β-galactosidase is present extracellularly in this case, and whether β-galactosidase is present extracellularly in the model flat ELM.

Taken, these experiments suggest that the 3,4-cyclohexenoesculetin pigment is located outside the cell. In the model flat ELM grown on media-saturated melamine foam, the pigment diffuses slowly into the media, so the bacterial patch accumulates pigment to opacity. While the pigment being located extracellularly raises the possibility that it could be physically washed out of the living material, it could complicate future engineering of enzymatic degradation of pigment: the pigment-degradation enzyme would need to be exported from the cell into the surrounding media.

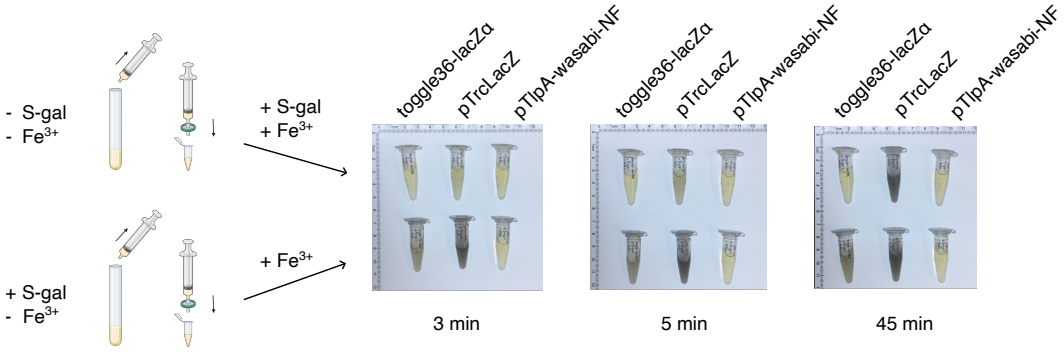

Figure 4.23: Formation of pigment in filtered media after overnight growth of *E. coli*.

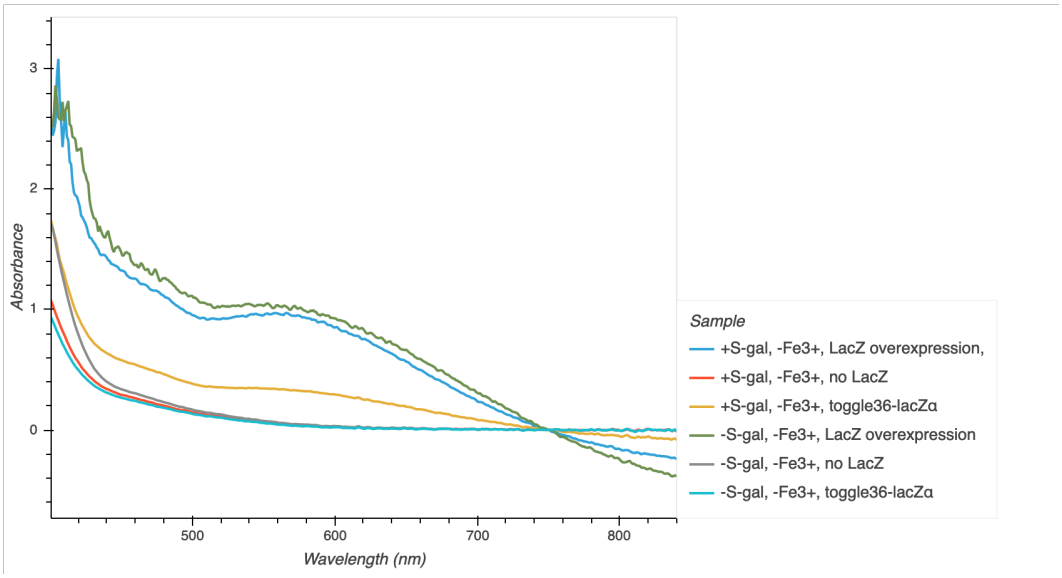

Figure 4.24: Visible light spectrum of pigment in filtered media after overnight growth of *E. coli*.

Details of design and construction of illuminated incubator with *in situ* temperature monitoring

To grow our model flat ELM with illumination, simulating sunlight conditions, we constructed an illuminated growth chamber with sensors for monitoring the temperature of the samples as well as the temperature inside and outside of the sample enclosure.

Solar illumination at the surface of the Earth reaches 1000 $\frac{W}{m^2}$ when the sun is directly overhead. We used a 100 W white light LED grid (Mifxion via Amazon) as a cost-effective simulant of sunlight. While the output appears white to the human eye, the provided spectrum report indicates a strong blue peak. At a distance of 120 mm from the light source, the light flux averages 120000 lx, slightly higher than direct sunlight.

We considered various materials for the sample chamber, including a 9 qt cooler and cardboard, before deciding to use an aluminum enclosure. After preliminary experiments, we discovered that the 100 W LED light gets hot enough to cause the cooler, made of insulating material, to exceed 60°C within 30 min. While the cardboard, which is much thinner and less insulating, reached a more reasonable steady state temperature of approximately 40-45°C (which we further lowered below 37°C by adding fans to the LED light) it was not a feasible material to use with bacterial samples because of the risk of contamination. Aluminum, which can be decontaminated using isopropyl alcohol, is thin and thermally conductive. The enclosure we used is able to reach a steady state temperature of 32°C with illumination from the LED without electronic heating or cooling when the outside of the chamber is exposed to a room temperature of 18°C.

We used 3D-printed polylactic acid (PLA) supports attached to threaded rods to suspend the LED at an appropriate height above aluminum enclosure (Figure 4.25a,b) At a room temperature of 18°C, we could grow samples at 32°C inside the chamber. At higher room temperatures, we used alternative supports which could hold computer fans, blowing along the length of the LED light housing, to reduce the heat radiating from the LED into the chamber.

The lid of sample chamber consists of a 1/8" layer of glass to filter IR and a 1.5 mm layer of clear acrylic to filter UV, while allowing visible light illumination of the samples. A 3D-printed PLA collar holds the glass and acrylic in place, and we applied weatherproofing foam to the inside of the collar to provide a tight fit between the lid and the box. This is crucial to ensure high humidity inside the enclosure;

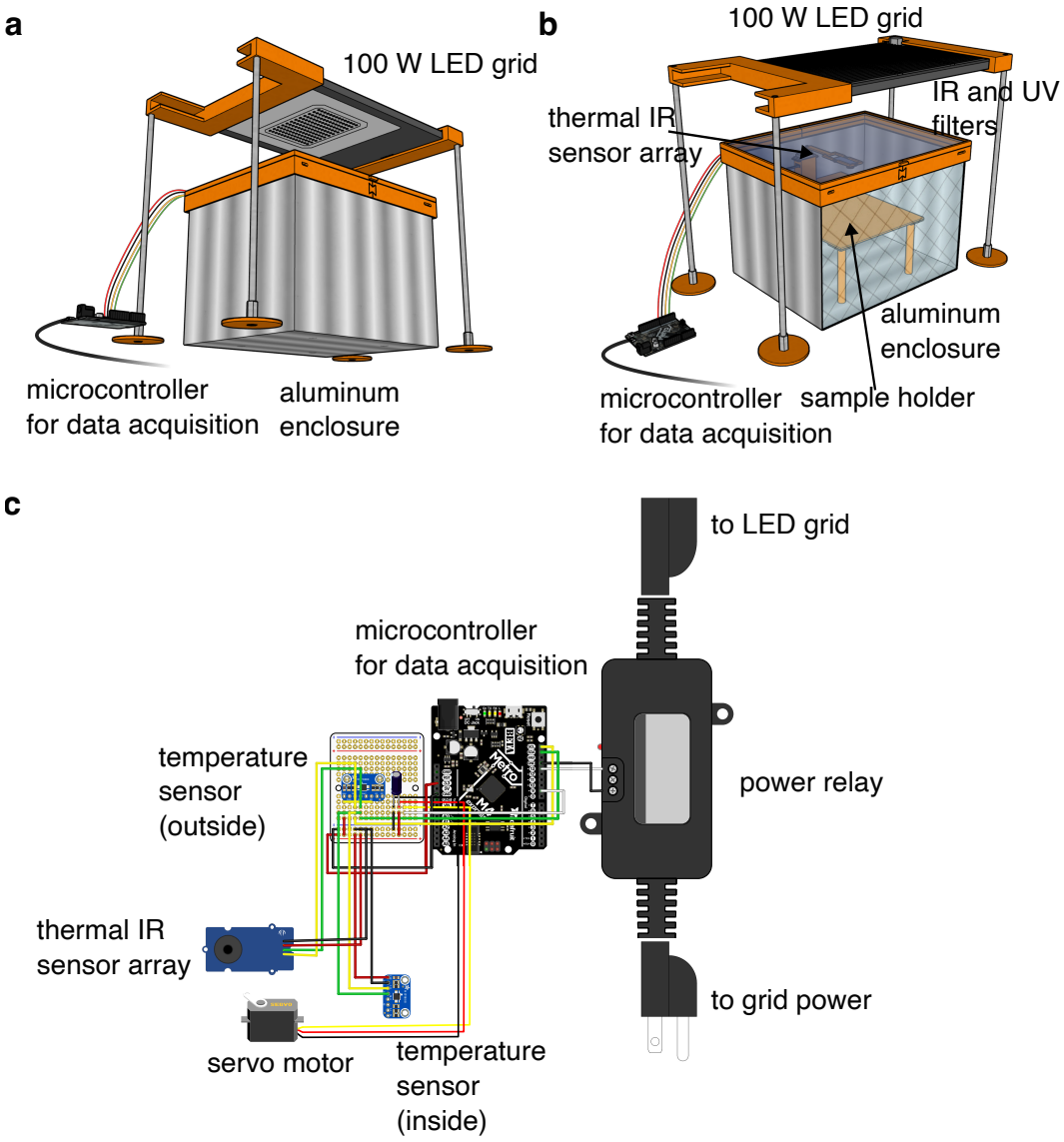

Figure 4.25: Hardware of illuminated growth chamber (a, b) Schematic of illuminated growth chamber, with views showing the LED grid (a) and the lid and interior of the chamber (b; repeated from Figure 4.5b). (c) Schematic of microcontroller and components for measuring temperature and controlling illumination source. In the final design, the servo motor is powered externally and the microcontroller is the Adafruit Feather M4 Express.

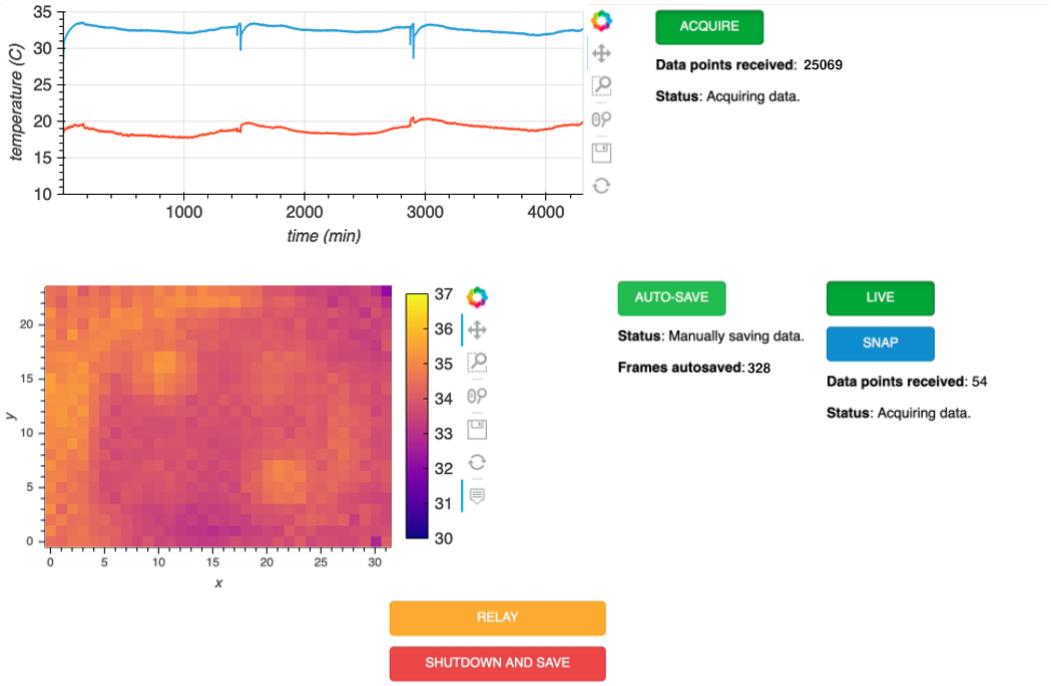

Figure 4.26: Graphical user interface of software, written using the Bokeh Python package, of illuminated growth chamber (representative graphs added).

otherwise, the rate of evaporation of water from the sample and media is so high that the samples cannot grow. To increase the humidity inside the chamber, we placed pieces of common cellulose kitchen sponge in two 100×10 mm petri dishes on the floor of the chamber and saturated them with water. The sponge pieces draw water to sample height and allow it to evaporate into the air there.

To increase the temperature inside the sample chamber to 42°C, we added a layer of 1/2" melamine foam insulation, held in place with a 1/8" cardboard backing and a layer of aluminum foil (which also reflects heat back into the chamber). We avoided implementing electronic temperature control for simplicity; in addition, an electric heater and/or cooler could cause inhomogeneous temperature within the chamber and require a fan, which would increase evaporation fron the sample and media.

For 32° experiments, we used a 3D-printed PLA platform to hold the samples at an appropriate distance from the light source. However, for 42° experiments, the PLA absorbed light and warmed above its glass transition temperature and deformed; we substituted with an acrylic platform.

We wanted to monitor the temperature inside the chamber, the temperature outside the chamber, and the temperature of the samples. We used an Arduino-compatible

microcontroller to control sensors and acquire data. We used MCP9808 high accuracy temperature sensors (Adafruit) for the interior and exterior of the chamber. We attached a 40x10mm 5V fan (Noctua NF-A4x10) to the sensor inside the chamber to remove heat due to the sensor itself absorbing light. To noninvasively monitor the temperature of up to four samples, we chose to use a MLX90640 32 x 24 thermal IR array with $110^\circ \times 70^\circ$ field of view (Adafruit or Grove). We attached this lightweight sensor to a servo motor using 3D-printed PLA fittings so that it could swing over the samples to acquire data, then swing away to avoid casting a shadow. While this sensor is affordable and the small form factor facilitates motorization, the low spatial resolution means that we cannot precisely measure the temperature of the samples. However, we can clearly visualize samples that heat above the background. The PLA fittings were wrapped in aluminum foil and reinforced with wooden craft sticks to avoid deforming from heating due to light absorption.

By necessity, one temperature sensor, the servo motor, the thermal IR array, and their wires are exposed to the humidity inside the sample chamber. For 32° experiments, no condensation occurred on the electronics. However, for 42° experiments, water did condense on the splice points of wires for the thermal IR array, which caused short-circuiting and prevented data acquisition. We carefully rearranged the wires so that the splice points could sit outside the sample chamber.

We connected all sensors, the servo motor, and a power relay to an Arduino-compatible 3V microcontroller (Figure 4.25c). The power relay allows the microcontroller to interface with the LED light source, which runs on 120V grid power. The thermal IR array requires at least 20KB RAM. We initially chose the Adafruit Metro M4 Express (3382) with presoldered headers for prototyping, then switched to the Adafruit Feather M4 Express and soldered wires directly to its printed circuit board for stability. Both of these microcontrollers have an Arm Cortex-M4 processor with 512KB of flash and 192KB of RAM, and are compatible with the Arduino IDE.

To interface with the microcontroller, we wrote a custom application using the Bokeh package in Python (Figure 4.26). We included buttons to toggle automatic acquisition of ambient exterior and interior temperature at 5 s intervals, with data saved at 30 min intervals; to toggle automatic acquisition of thermal IR images at 10 min intervals; to acquire and view a live thermal IR image; to save the last acquired thermal IR image; to toggle the light source using the power relay; and to shutdown the application and perform a final save. We reset the microcontroller and started the

software application at the beginning of each experiment. By using remote desktop software, experiments could be monitored remotely.

This combination of hardware and software enabled the experiments described in Figures 4.6 and 4.7. The apparatus could be improved for future experiments by adding finer temperature control using electronics, and a different enclosure geometry with an opening on a side would allow for placing and adjusting samples without disturbing the lid, on which water can condense during high temperature experiments. In addition, we could implement a peristaltic pump system for adding either water to the humidifying sponges or media directly to the sample system. The pump could either run autonomously, or be connected to the microcontroller. Finally, for ease of use, the software could be rewritten to allow for user input of the data acquisition and saving intervals, and to provide error messages to the user in the interface (currently, error messages output to the Terminal).

This work would not have been possible without Justin Bois and materials from the Introduction to Programming in the Biological Sciences Bootcamp (2020 and 2021 editions). Thank you also to Red Lhota for initial conversations about building this apparatus.

References

(1) Nguyen, P. Q.; Courchesne, N.-M. D.; Duraj-Thatte, A.; Praveschotinunt, P.; Joshi, N. S. *Advanced Materials* **2018**, *30*, 1704847.

(2) Gilbert, C.; Ellis, T. *ACS Synthetic Biology* **2019**, *8*, 1–15.

(3) Liu, S.; Xu *Frontiers in Sensors* **2020**, *1*, DOI: 10.3389/fsens.2020.586300.

(4) Rivera-Tarazona, L. K.; Shukla, T.; Singh, K. A.; Gaharwar, A. K.; Campbell, Z. T.; Ware, T. H. *Advanced Functional Materials* **2022**, *32*, 2106843.

(5) Heveran, C. M.; Williams, S. L.; Qiu, J.; Artier, J.; Hubler, M. H.; Cook, S. M.; Cameron, J. C.; Srubar, W. V. *Matter* **2020**, *2*, 481–494.

(6) Huang, J. et al. *Nature Chemical Biology* **2019**, *15*, Number: 1 Publisher: Nature Publishing Group, 34–41.

(7) González, L. M.; Mukhitov, N.; Voigt, C. A. *Nature Chemical Biology* **2020**, *16*, Number: 2 Publisher: Nature Publishing Group, 126–133.

(8) Heyde, K. C.; Scott, F. Y.; Paek, S.-H.; Zhang, R.; Ruder, W. C. *JoVE (Journal of Visualized Experiments)* **2017**, e55300.

(9) Duraj-Thatte, A. M.; Courchesne, N.-M. D.; Praveschotinunt, P.; Rutledge, J.; Lee, Y.; Karp, J. M.; Joshi, N. S. *Advanced Materials* **2019**, *31*, _eprint: https://onlinelibrary.wiley.com/doi/pdf/10.1002/adma.201901826, 1901826.

(10) Guo, S. et al. *ACS Synthetic Biology* **2020**, *9*, Publisher: American Chemical Society, 475–485.

(11) Blount, Z. D. *eLife*, *4*, e05826.

(12) Winfield, M. D.; Groisman, E. A. *Applied and Environmental Microbiology* **2003**, *69*, Publisher: American Society for Microbiology, 3687–3694.

(13) Van Elsas, J. D.; Semenov, A. V.; Costa, R.; Trevors, J. T. *The ISME Journal* **2011**, *5*, Number: 2 Publisher: Nature Publishing Group, 173–183.

(14) Shaw, M. K.; Marr, A. G.; Ingraham, J. L. *Journal of Bacteriology* **1971**, *105*, 683–684.

(15) Broeze, R. J.; Solomon, C. J.; Pope, D. H. *Journal of Bacteriology* **1978**, *134*, 861–874.

(16) Rudolph, B.; Gebendorfer, K. M.; Buchner, J.; Winter, J. *The Journal of Biological Chemistry* **2010**, *285*, 19029–19034.

(17) Voigt, C. A., *Synthetic Biology: Methods for part/device characterization and chassis engineering*, Google-Books-ID: i_B4LwPVmL4C; Academic Press: 2011; 734 pp.

(18) Piraner, D. I.; Abedi, M. H.; Moser, B. A.; Lee-Gosselin, A.; Shapiro, M. G. *Nature Chemical Biology* **2017**, *13*, 75–80.

(19) Levskaya, A.; Chevalier, A. A.; Tabor, J. J.; Simpson, Z. B.; Lavery, L. A.; Levy, M.; Davidson, E. A.; Scouras, A.; Ellington, A. D.; Marcotte, E. M.; Voigt, C. A. *Nature* **2005**, *438*, Number: 7067 Publisher: Nature Publishing Group, 441–442.

(20) Anderson, J. C.; Voigt, C. A.; Arkin, A. P. *Molecular Systems Biology* **2007**, *3*, Publisher: John Wiley & Sons, Ltd, 133.

(21) Krikštaponis, A.; Meškys, R. *Molecules : A Journal of Synthetic Chemistry and Natural Product Chemistry* **2018**, *23*, 2613.

(22) Walsby, A. E. *Microbiological Reviews* **1994**, *58*, 94–144.

(23) Bourdeau, R. W.; Lee-Gosselin, A.; Lakshmanan, A.; Farhadi, A.; Kumar, S. R.; Nety, S. P.; Shapiro, M. G. *Nature* **2018**, *553*, Number: 7686 Publisher: Nature Publishing Group, 86–90.

(24) Ai, H.-w.; Olenych, S. G.; Wong, P.; Davidson, M. W.; Campbell, R. E. *BMC Biology* **2008**, *6*, 13.

(25) Part:BBa_I11012, Registry of Standard Biological Parts `http://parts.igem.org/Part:BBa_I11012`.

(26) Part:BBa_B1002, Registry of Standard Biological Parts `http://parts.igem.org/Part:BBa_B1002` (accessed 11/29/2022).

(27) Levin-Karp, A.; Barenholz, U.; Bareia, T.; Dayagi, M.; Zelcbuch, L.; Antonovsky, N.; Noor, E.; Milo, R. *ACS Synthetic Biology* **2013**, *2*, Publisher: American Chemical Society, 327–336.

(28) Der, B. S.; Glassey, E.; Bartley, B. A.; Enghuus, C.; Goodman, D. B.; Gordon, D. B.; Voigt, C. A.; Gorochowski, T. E. *ACS Synthetic Biology* **2017**, *6*, Publisher: American Chemical Society, 1115–1119.

(29) Schneider, C. A.; Rasband, W. S.; Eliceiri, K. W. *Nature Methods* **2012**, *9*, Number: 7 Publisher: Nature Publishing Group, 671–675.

(30) Esculetin SDS No. S4711 [Online]; Selleck Chemicals, `https://www.selleckchem.com/msds/MSDS_S4711.pdf`.

Chapter 5

CONCLUSIONS AND FUTURE DIRECTIONS

This thesis describes new tools for thermal control of *E. coli*, building on previous work in the use of TcI and TlpA mutants as hot-on bioswitches. Hot-on bioswitches are promising for *in vivo* medical applications, as they can serve as sensors of fever, or clinicians can send a noninvasive heat signal deep into tissue using focused ultrasound. Now, by engineering cold-on bioswitches, we can expand the application space for temperature sensing, including the design of therapeutic cells that die when leaving the warm interior of the body; the coupling of gene induction to the lowering of the temperature of cell culture to promote protein stability and reduce the formation of inclusion bodies; and, as discussed in this thesis, the activation of cold-protective measures when the ambient temperature drops, such as for living materials.

In Chapter 2, we presented direct low temperature gene induction by TcI mutants, using their ability, inherited from wildtype λ repressor, to act as transcriptional activators. In addition, a single TcI mutant can be used as a state switch, controlling two genes with opposite thermal response profiles. In Chapter 3, we discussed inversion of heat-inactivated transcriptional repression using a temperature-insensitive repressor, an orthogonal protease, or both in combination. In Chapter 4, we used our most promising multi-component circuit architecture to develop a genetically-encoded mechanism to turn on production of a light-absorptive pigment below 36°C, enabling *E. coli* in a model ELM to warm with illumination and improve in growth rate. This represents the first use of temperature sensing and self-regulation for ELMs.

5.1 Pushing the lower limit of temperature sensing

The genetic circuits presented here are useful for relatively small excursions below the ideal physiological temperature of 37°C. To sense lower temperature thresholds, the transcription factors used in this work require further tuning. While TcI has been further mutated to function as a temperature-sensitive repressor with a threshold as low as 32°C (unpublished). Further evolution yielded a mutant with a threshold of 30°C, with leaky expression below the threshold that could be mitigated by the addition of a degradation tag. However, this mutant was not able to activate

gene expression at any temperature between 25°C and 42°C. This may be due to its mutations in the N-terminal domain, which contains the interface with RNA polymerase that mediates transcriptional activation. Thus, 30°C may be near the lowest threshold achievable for TcI mutants — any further mutation may result in such unstable binding to the DNA operator sites that no repression with sharp switching can occur. Although our lowest-switching mutant can still repress, it has lost its ability to stabilize the interaction between RNA polymerase and the P_{RM} promoter. To ascertain whether the lowest temperature threshold for activation has been reached, directed evolution experiments could be performed with the activation construct instead of the repression construct.

Our pigment temperature switch construct, based on inversion of TlpA36 using CI repressor, increased the growth of patches of *E. coli* growing at 32°C with illumination compared with an unpigmented control. Finite element analysis suggests that the addition of insulation to the system could allow pigmentation to protect *E. coli* growing in an environment as cold as 4°C with illumination. However, in this case, full production of pigmentation at 16°C or above would be detrimental, and in fact, pigment production should cease as soon as the surroundings fall below about 30°C. To achieve this, TlpA36 could be used as the parent for directed evolution. In addition, it may be beneficial to screen the mutant library in the inverted construct.

5.2 Further development of the pigment temperature switch for protection of *E. coli*-based ELMs from nonoptimal environmental temperatures

With our current construct, pigment accumulates in our *E. coli* with brief exposure to low temperature. We could avoid production of pigment at night by incorporating light sensing proteins, for example based on flavin-binding light oxygen and voltage (LOV) domains or phytochromes [1]. Using an AND gate [2], we could engineer a circuit to turn on pigment production only with low temperature and light, so that in environments where the daytime temperature exceeds 37°C, low nighttime temperatures do not cause pigment to develop, which would cause overheating the next day. Future experiments could also include the development of an enzyme cassette for biodegradation of our pigment. 3,4-cyclohexenoesculetin is chemically related to esculetin and other naturally-occuring coumarin derivatives, which are degraded by soil bacteria [3].

In addition to preventing unnecessary pigment production and degrading pigment when it is no longer needed, we could develop a mechanism for *E. coli*-based ELMs

to scatter light at high temperature. For example, gas vesicles, which are hollow gas-filled protein nanostructures derived from *Anabaena flos-aquae*, Halobacterium NRC-1 or *Serratia marcescens* [4–6], could be expressed above 37°C, increasing protection from heat.

Finally, our pigment is based on a synthetic small molecule; the precursor must be added to the media of the ELM. Future work could entail the development of alternative enzymatically-produced pigments. For example, our β-galactosidase / S-gal system is highly analogous to the β-glucosidase / esculin system for differentiation of Enterococcus and Enterobacteriaceae [7]. β-glucosidase hydrolyzes esculin to yield esculetin, which complexes with ferric iron to form a black pigment. The cyclohexene group in S-gal reduces the diffusivity of the resulting pigment in aqueous conditions compared with esculetin. Esculin occurs naturally in some plants. Alternatively, *E. coli* can produce eumelanin, a black-brown pigment, from tyrosine using a tyrosinase mutant derived from *Rhizobium etli*, a root nodule bacterium [8]. Interestingly, Lagunas-Muñoz *et al.* report that melanin production is optimal at 30°C, which could be useful for the ELM application. In our preliminary experiments, eumelanin was readily formed by BL21 *E. coli* in liquid culture with shaking, but less readily in colonies; however, parameters such as the tyrosine concentration and pH could be tuned for eumelamin production at low temperature in patches of *E. coli*.

References

(1) Choi, J.; Ahn, J.; Bae, J.; Koh, M. *Molecules* **2022**, *27*, Number: 20 Publisher: Multidisciplinary Digital Publishing Institute, 6798.

(2) Anderson, J. C.; Voigt, C. A.; Arkin, A. P. *Molecular Systems Biology* **2007**, *3*, Publisher: John Wiley & Sons, Ltd, 133.

(3) Krikštaponis, A.; Meškys, R. *Molecules : A Journal of Synthetic Chemistry and Natural Product Chemistry* **2018**, *23*, 2613.

(4) Shapiro, M. G.; Goodwill, P. W.; Neogy, A.; Yin, M.; Foster, F. S.; Schaffer, D. V.; Conolly, S. M. *Nature Nanotechnology* **2014**, *9*, Number: 4 Publisher: Nature Publishing Group, 311–316.

(5) Bourdeau, R. W.; Lee-Gosselin, A.; Lakshmanan, A.; Farhadi, A.; Kumar, S. R.; Nety, S. P.; Shapiro, M. G. *Nature* **2018**, *553*, Number: 7686 Publisher: Nature Publishing Group, 86–90.

(6) Hurt, R. C.; Buss, M. T.; Duan, M.; Wong, K.; You, M. Y.; Sawyer, D. P.; Swift, M. B.; Dutka, P.; Barturen-Larrea, P.; Mittelstein, D. R.; Jin, Z.; Abedi, M. H.; Farhadi, A.; Deshpande, R.; Shapiro, M. G. Genomically mined acoustic reporter genes enable real-time in vivo monitoring of tumors and tumor-homing probiotics, Pages: 2021.04.26.441537 Section: New Results, 2022.

(7) Lindell, S. S.; Quinn, P. *Journal of Clinical Microbiology* **1975**, *1*, 440–443.

(8) Lagunas-Muñoz, V.; Cabrera-Valladares, N.; Bolívar, F.; Gosset, G.; Martínez, A. *Journal of Applied Microbiology* **2006**, *101*, 1002–1008.